MECHANICS OF PEELING: COHESIVE ZONE LAW AND STABILITY

Thesis by

Christopher Kovalchick

In partial Fulfillment of the Requirements

for the Degree of

Doctor of Philosophy

California Institute of Technology

Pasadena, California

2011

(Defended May 9, 2011)

To Nanny, who has and always will be with me every step of the way.

Acknowledgements

I have been very fortunate during my time at Caltech to be surrounded by some absolutely incredible and inspiring people. I would like to first and foremost thank my advisor, Prof. G. Ravichandran. I could not have asked for a better mentor and advisor than Ravi, who has always believed in me while challenging me to be the best I can be each and every day. I am grateful for his tutelage and guidance through the past few years.

I would like to thank the members of my thesis committee: Prof. Kaushik Bhattacharya, Prof. Wolfgang Knauss, and Prof. Chiara Daraio for offering their guidance, mentorship, and support throughout my graduate study. I am also grateful for collaborations with the truly brilliant minds I have worked with in various areas of my thesis research, including Prof. Alain Molinari from the Universite de Metz and Dr. Shuman Xia here at Caltech.

I would like to thank my colleagues of the Experimental Mechanics Lab past and present, whom I have enjoyed getting to know, work with, and interact with on a regular basis over the years: Christian Franck, Winston Jackon, Sharlotte Kramer, Benny Poon, Ling Zheng, Mike Silva, Justin Brown, Jacob Notbohm, Victoria Stolyar, Kristen John, Laurence Bodelot, Maen Alkhader and Addis Kidane.

I would also like to thank the members of the solid mechanics community at Caltech, particularly the Bhattacharya group, Harsha Bhat, and Mike Mello. Mike has taught me not only about experimental mechanics and methods, but about every facet of life in

general. I will miss our daily conversations and the joy we always shared in each others' scientific discoveries.

I would like to thank my family, particularly my mother and father, who from 3000 miles away have inspired me to never settle for anything less than my best. My mother's fight with Multiple Sclerosis has been and will continue to be a daily inspiration for me. Keep fighting.

To my fiancée, Emily, who has waited in the great Northwest patiently for this day for the last 18 months. I look forward to the next chapter in our lives together.

To John Meier and Pablo Abad-Manterola, the best two friends I could have ever asked for. John, I thank you for not telling me I was ridiculous when signing up for the Rose Bowl Half-Marathon in 2007. It has changed my life.

A special thanks to Prof. John Dabiri, who has and will continue to be a lifelong friend and mentor, both in the classroom and on the golf course.

I would also like to thank the many friends who I have been able to meet and spend great times with both at Caltech and outside, including Andrew Tchieu, Jeffrey Hanna, Philipp Boettcher, Nicholaus Parziale, Yousi Ma, Jesse Arian, Lenny Lucas, David Pekarek, and Tony Roy.

Abstract

The measurement of interface mechanical properties between an adhesive layer and a substrate is significant for optimization of a high-quality interface. A common method for measuring these properties is the peel test. While there are many interesting applications of peel in such areas as cell and gecko adhesion, the focus here is to obtain a better understanding of the fundamental mechanics underlying the problem.

The mechanics of the peel test is examined through experiments, finite element simulations, and theoretical analysis with the aim of developing governing relations to describe the role of fracture in the peel test for elastic adhesive tapes. An inverse formulation is developed to extract a cohesive zone law from a set of experimental peel tests using a theoretical framework based upon non-linear beam theory. Through extracting a cohesive zone law, the adhesion energy during a peel test is determined along with the force distribution in the process zone. This local method of determining the adhesion energy is compared to a global method used by Rivlin in the context of finite deformations, showing good agreement.

The effect of rate dependence in the peel test is also examined experimentally, with the results used to derive a rate-dependent power law for the adhesion energy in a peel test as a function of the peel rate. The effects of varying different geometrical parameters during the peel test and how they affect the force distribution and adhesion energy are also presented. Finally, a study of the stability in the peel test, including the role of compliance through several newly developed force-controlled experimental configurations is discussed. The stiffness of the system is varied by altering the

magnitude and direction of the applied load during a test. This change in stiffness can be tuned to trigger or delay the onset of instability. Theoretical stability criteria are also presented to to develop insights into the role of parameters investigated experimentally.

Table of Contents

List of Figures

List of Tables

Chapter 1

Introduction

The applications of peeling and its role in adhesion are widespread in both engineering and biology. A specific problem that has captivated a diverse group of scientists, particularly mechanicians, in the area of peeling and adhesion for the last decade is the enhancement of the adhesive properties of materials through studying analogous behavior in nature. More specifically, investigations focused on naturally-occurring reversible adhesion in biological systems can be applied to the development of engineered reversible adhesive systems, which have a wide range of engineering applications including biomedical devices [1], microelectronic storage and packaging [2], and surgical robotics [3]. At the core of this problem are the mechanics, both on the micro- and macroscale, of how a natural reversible adhesion process works.

The reversible adhesion problem can be broken down into two parts: 1) enhancing adhesion, and 2) decohesion, or releasing adhesion. Traditional adhesives used in every-day settings such as tapes and glue are categorized as pressure-sensitive adhesives (PSAs). While these materials can stick to most surfaces with the application of simple contact and slight pressure, detachment of these adhesives usually prevents significant reattachment due to contamination. Thus, while one can attempt to enhance the strength

of these adhesives, releasing this adhesion in order to complete the reversible process is currently very difficult [4].

The best way to examine the entire process of reversible adhesion is to study examples in nature. One of the most investigated examples is the mechanics and locomotion of the gecko. The gecko is often referred to as “nature’s supreme climber” due to its ability to scale vertical and inverted surfaces [5]. This is possible through the structural hierarchy of the gecko’s foot, which acts as a reversible dry adhesive. The smallest two levels of this structure are the micron-sized setae and the sub-micron-sized spatulae. Experimental studies on the setae of a gecko’s foot show that when a single seta is properly oriented and dragged, it can generate 200 μN in shear force (parallel to the adhered surface) and 40 μN in normal force (perpendicular to the adhered surface). The resulting net forces are more than three orders of magnitude greater than required to support a gecko’s body weight. While the gecko is a strong climber, it is also able to detach its foot from a surface in as little as 15 ms [6]. Thus, the question arises of how the setae on a gecko’s foot are strong enough to support so much force, while simultaneously allowing the gecko to move so rapidly. The answer to this is attributed to the macroscopic peeling process by which the gecko removes its foot. By efficiently peeling its foot from the surface through a critical angle of about 30°, the foot easily detaches, leaving behind no residue. In this peeling process, the question arises of the stability of the gecko’s foot. This stability may be influenced by the stored energy in the muscles of the foot, particularly in the process of how the gecko releases the stored energy to optimize its efficiency.

The gecko adhesion process is ideal as a basis for modeling synthetic adhesive materials because of the implications of the structural hierarchy of the gecko's foot. Recent research suggests that a structural hierarchy is the key principle behind robust adhesion [7]. In an adhesion process, this hierarchy is a combination across multiple length scales. As a new level of hierarchy is added, the adhesion energy is exponentially enhanced. In the case of the gecko, adhesion is based upon the hierarchical structure of the setae and spatulae on the foot that become smaller at the contact regions with the surface. With the introduction of this theory, we can see that it is neither the macroscale nor the microscale individually that govern the adhesion process, but rather a combination across length scales [8].

When dealing with a multiscale problem such as reversible adhesion, it is important to understand the behavior across all length scales. This is where the use of mechanics, both micromechanics and mechanics on a continuum scale, plays an important role. The application of micromechanics is useful for studying the adhesion between the smallest fibers of an adhesive and the surface to which they are attached. These forces are very small when measured individually. However, considering the collection of fibers as a continuum on the macroscale, the global adhesion force is several orders of magnitude larger.

1.2 Early Background of the Mechanics of Peeling

The measurement of interface mechanical properties between an adhesive layer and a substrate is significant for optimization of a high-quality interface [9]. A common method

for measuring these properties is the peel test, a technique that can be traced back to the results of investigations on the surface energy that exists between two elastic solids in contact [10]. However, the way in which these interfacial properties are investigated and measured has evolved over the past half-century. In the 1950's and 60's, two primary drivers in the study of interfacial adhesives were the tire and rubber industry. Gent pioneered numerous studies, both simple and complex, in the peeling of an adhesive polymer from a surface at a fixed angle, either perpendicular to or parallel to the surface [11]. Kaelble produced a series of papers in the early 1960's, which were among the first to draw the parallel that the peel problem could be viewed in the spirit of fracture mechanics [12, 13, 14], focused specifically on the mechanics of peeling and adhesion and the role of microfracture mechanisms in the process. Further studies at the forefront include the adhesion tests of Liechti and Knauss [15], the constitutive behavior of an adhesive polymer in a double cantilever beam configuration using optical interferometry [16], and the investigation of the local fibrillation zone that develops in an adhesive when peeled from a surface and the relation of a local stress distribution to this region [17]. Perhaps the most significant study is that of Rivlin in 1944, where a simple relation was derived in the context of finite deformations between the adhesion energy in the peeling process and the applied force at a fixed peel angle [18].

At the same time, the review of the study of peel cannot be considered complete without the work of three of the pioneers of the field of contact mechanics, Johnson, Kendall, and Roberts (JKR). Stemming from the Hertz contact problem and subsequent JKR contact adhesion model [19], Kendall investigated the peeling problem to develop simple analytical relations to describe the different phenomena that govern the peel test

and its significant utility in studying adhesion. Such studies include the determination of the shape of an elastic band upon being peeled from a surface [20], the development of interfacial dislocations in a peel test [21], and foremost the application of first principles in mechanics to describe the competing energies in the process [22].

The rate-dependence of the peel problem has also been investigated, particularly since the peeling of adhesives involves the behavior of soft materials, which display non-linear elastic and viscoelastic properties. An early study of Anderson (1974) extracted the adhesion energy during a mixed-mode fracture process from a peel test using a layer of solithane adhered to a PMMA substrate [23]. This material system combination was seen to be highly rate-dependent, which motivates the need for the study of rate-dependency in the peel test.

1.3 Current Work in Peeling – The Need for Experiments

Recent work in peeling is of interest in a variety of scientific areas. There are several applications of peeling in the field of biomechanics, particularly in the area of gecko adhesion, as previously discussed. In the microelectronics community, the focus of peeling has been on the delamination strength of thin films to silicon substrates [24]. Additionally, environmental conditions such as moisture and thermal gradients can degrade the strengths of devices due to strain mismatches between the film and the substrate. From an industrial standpoint, the peel test has been used primarily for comparative strength testing of materials for case-specific applications. These include quality control devices in which the ultimate peel strength of a material is a critical parameter [25].

While there are many interesting applications of peel in such areas as cell adhesion and motility [26, 27], biomaterial adhesion [28], as well as the development of mechanical and material laws for adhesion based upon systems like the gecko, the focus on the peel test is to obtain a better understanding of the fundamental mechanics underlying the problem. The proposition of this test as one based upon first principles and fracture mechanics has generated a renewed interest in the subject, particularly in developing theoretical models of the process [29, 30]. There is significant insight into the adhesion process that is obtained in modeling the peel test as a bimaterial interfacial fracture problem. Wei and Hutchinson have developed models describing the macroscopic work of fracture in the peel test that make beautiful correlations between the adhesion energy in a fracture problem and a peel test [31]. Thouless and Yang have conducted parametric analyses of the peel test to examine the incorporation of various phenomena such as shear forces and bending energies into analytical models [32]. Other recent models are aimed at incorporating additional parameters during the peeling process such as the dissipation of plastic energy [33], non-linear elastic effects [34], and the extensibility of the tape [35, 36].

While analytical models exist, there is a need for more rigorous experiments in the peel test to validate these models. Pesika et al. have conducted simple yet elegant peel tests that provide insight into developing a process-zone model that mimics the material properties of the gecko [37]. Wei and Zhao developed an experimental peel arrangement for testing the adhesion of ductile thin films to ceramic substrates [38]. In combination

with analytical models, experimental peel tests can yield very powerful insights into the role of adhesion energy during a peel test.

1.4 Global Energy Approach – Peel Mechanics

Consider the peeling of an elastic thin film from a rigid substrate, shown in Figure 1.1 [18]. Specified parameters are the film thickness, h, film width, b, peel force, P_f, the angle of peel between the film and the substrate, θ, the extension of the unadhered portion of the film, δ_e, the length of the peeled portion of film, c, the elastic modulus of the film, E, and the incremental length of the film to be peeled, Δc. For this problem, a linearly elastic, extensible adhesive film with constant width and thickness is assumed.

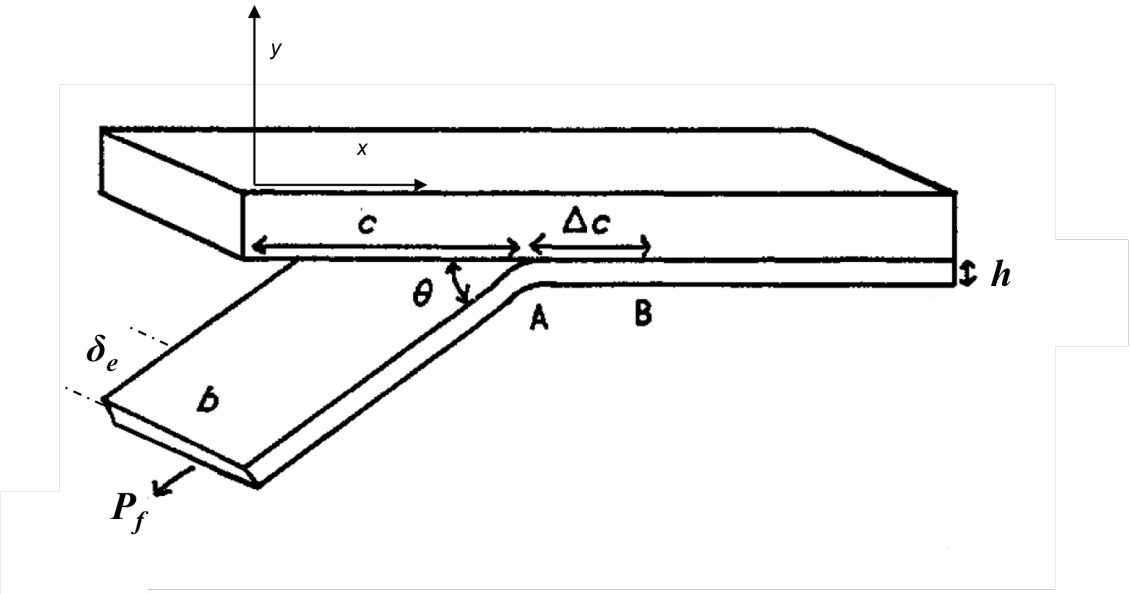

Figure 1.1: Schematic of the peel test for a linearly elastic, extensible adhesive tape (Kendall, 1975).

An energy balance of the process of peeling the film through the length Δc shows that the work done by the peel force is equal to the change of the stored internal energy of the system

$$\Delta W_P = \Delta U_E + \Delta U_S \tag{1.1}$$

where ΔW_P is the work due to peel, ΔU_E the change in the elastic energy stored in the film due to extension of the peeled portion c, and ΔU_S the change in the surface energy due to the creation of new crack surfaces.

The surface energy U_S is defined as the amount of energy required to peel the tape to a new location while at a constant peel angle θ. It is given by

$$U_S = -bG\Delta c \tag{1.2}$$

where G is the adhesion energy, defined as the energy required to fracture a unit area of interface. The peel test can be considered as a fracture mechanics problem with a bimaterial interface of an adhesive and its backing attached to a rigid substrate. In this case, G is analogous to the fracture energy, considering that the surface energy here is due to the creation of new surfaces during the peeling process.

To determine the elastic energy term U_E, consider the extension of the tape in the peeled region, given by

$$\delta_e = \frac{P_f \Delta c}{Ebh}. \tag{1.3}$$

Thus, the elastic energy is given by the area under the force-displacement curve, or

$$U_E = \frac{1}{2} P \delta_e = \frac{P_f^2 \Delta c}{2Ebh}. \tag{1.4}$$

Balancing the energy stored via elastic and surface energies is the work done due to peel. When the film is peeled from A to B (Fig. 1.1), the point of application of the peel force P_f will move a distance, $\Delta c + \delta - \Delta c \cos\theta$. Therefore, the work due to peel is given as

$$W_P = -P_f \Delta c \left(1 + \cos\theta + \frac{P_f}{Ebh}\right). \tag{1.5}$$

Substituting Eqs. 1.2, 1.4, and 1.5 into Eq. 1.1 and solving for the adhesion energy, G

$$G = \frac{P_f^2}{2Eb^2 h} + \frac{P_f}{b}(1 - \cos\theta). \tag{1.6}$$

If the film is assumed to be inextensible, the first term corresponding to elastic energy vanishes and the simplified expression, known as the Rivlin Equation, is

$$\frac{P_f}{b} = \frac{G}{1 - \cos\theta}. \tag{1.7}$$

This expression was originally developed independent from Kendall's method by Rivlin in the context of finite deformations [18]. The assumption made here is that the tape is inextensible. Note that the Kendall equation (Eq. 1.6) includes the elastic energy of the tape, whereas Rivlin did not consider this term. An inextensible tape is said to be infinitely stiff. In this case, the elastic modulus is very large and the first term in Eq. 1.6 vanishes. This can also be observed by comparing the quantity of stress P_f/bh to the

elastic modulus E. For an inextensible material, $E >> P_f/bh$. For soft materials, this may not be the case and the extensibility of the film must be considered. The elastic energy term also plays a significant role at small peel angles (close to 0°).

The beauty of the energy-balance approach taken by Rivlin and Kendall is in its simplicity. The adhesion energy of the peel test can be estimated with knowledge of the peel angle θ and the far-field peel force, P_f. However, the Rivlin model does not give any information about the forces and displacements near the crack tip. In terms of a fracture mechanics problem, the Rivlin model does not provide any information, such as forces and displacements, near the crack tip. In order to obtain such detail, another method of describing this local region during a peel test is needed. One possible method is to treat this local region as a cohesive zone, which is described in the next section. One of the aims of this thesis is to use a cohesive zone law to obtain information in this local process zone region. This relates to the idea of approaching the peeling problem from both a macro (global) scale by using the Rivlin model, while considering the micro (local) scale that is governed by the cohesive zone.

1.5 The Cohesive Zone Law

The concept of a cohesive zone law is useful to describe the behavior close to the crack tip in a fracture mechanics problem, particularly in eliminating the singularity that occurs directly at the crack tip. One of the first studies in this area is that of Dugdale and the strip yield model [39]. Although the Dudgale model was originally developed to study thin, metal sheets, it is utilized as a primary model for the study of ductile fracture

as it sheds light on the limitations of the small scale yielding approach to describing the local region around a crack tip.

The Dugdale model essentially determines a region of constant or finite stress ahead of the crack tip. In the process of determining this value of finite stress, the crack opening displacement is also determined. This model is prototypical of the concept of the cohesive zone law. Barenblatt [40] utilized concepts from both Prandtl [41] and Dugdale to model a cohesive zone as a region around the crack tip in which the stresses in the yield zone ahead of the crack are expressed as a function of the displacement across the yield zone. Consider the mode-I fracture problem shown in Figure 1.2, given in the x_1-x_2 plane [42].

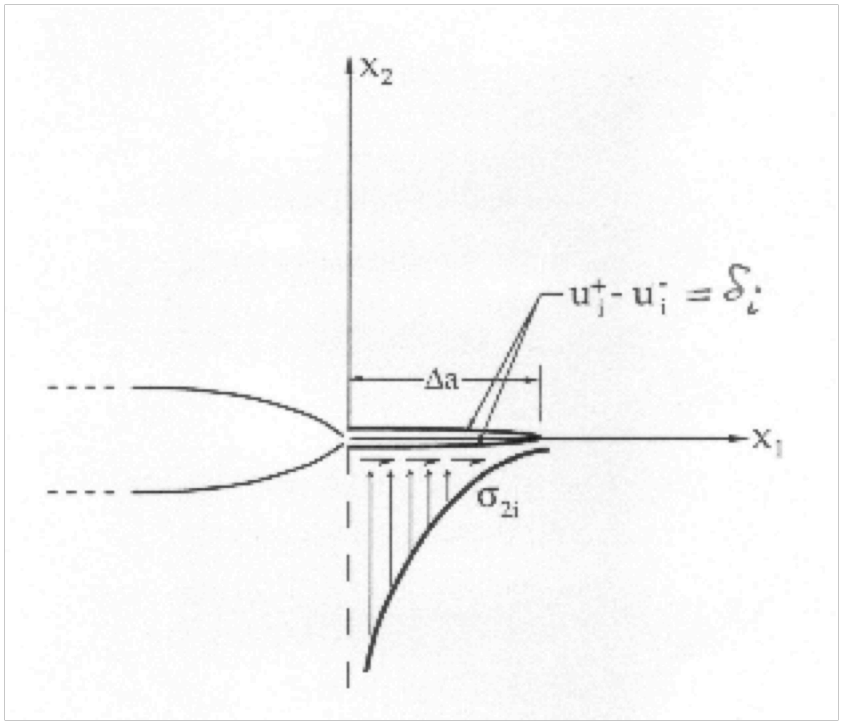

Figure 1.2: Cohesive zone in a fracture problem (from Hutchinson, 1979).

The crack, shown on the left of the diagram, precedes a region just beyond the crack tip shown with length Δa. This length Δa here defines the length of the cohesive zone. The cohesive zone height is defined by the crack tip opening displacement, δ_i which is a result of the displacement of the upper and lower crack surfaces, u_i^+ and u_i^-, respectively. The stress in this region is defined by σ_{2i}, which will be a function of the crack tip opening displacement, as can be seen in the figure. At the edge of the cohesive zone ($x_1 = \Delta a$), the cohesive stress σ_{2i} goes to 0.

The cohesive zone in a mode-I fracture problem can be defined in any number of ways in what is termed a cohesive zone law, or the material law that defines the stress in the cohesive zone as a function of the crack tip opening displacement, δ. The law is sometimes referred to as a traction-separation law. A set of studies by Ungsuwarungsri and Knauss derives a series of cohesive zone laws to describe the effects of non-linear cohesive forces on a crack tip [43, 44]. A schematic of a typical cohesive zone model is shown in Figure 1.3 [45].

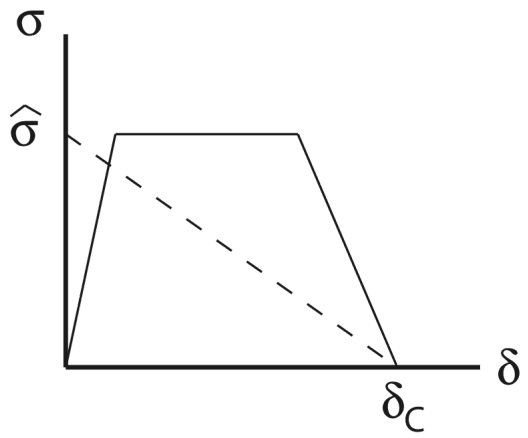

Figure 1.3: Schematic of a generic cohesive zone law (from Zehnder, 2008).

The two key parameters needed to define the cohesive zone law are the peak stress, $\hat{\sigma}$, and the critical crack tip opening displacement (CTOD), δ_c. The CTOD corresponds to the point ahead of the crack tip where the cohesive stress σ goes to 0, i.e., where $\delta = \delta_c$. Another interesting feature of the cohesive zone law is that the area under the cohesive zone curve in Figure 1.3 is equivalent to the fracture or adhesion energy of the process, *G,* or the energy required to separate the interface

$$G = \int_0^{\delta_c} \sigma(\delta) d\delta \tag{1.8}$$

where G is the fracture energy and $\sigma(\delta)$ is the functional form of the cohesive zone law. One of the most commonly used forms for the cohesive zone law is a power-law formulation written in terms of the stress in the x_2 direction

$$\sigma(x_2) = \sigma_0 \left(1 - \frac{x_2}{\delta}\right)^n \tag{1.9}$$

where σ_0 is the peak cohesive stress and n is the exponent of the power law. Figure 1.4 shows some typical sample cohesive zone laws of the form in Eq. 1.9, with n = 0, 1, and 2 corresponding to the different zone shapes from left to right, respectively.

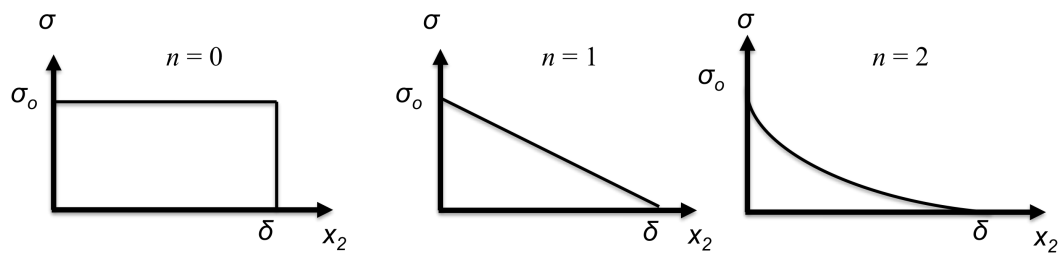

Figure 1.4: Sample cohesive zone laws used, of the form in Eq. 1.9.

The cohesive zone law is traditionally used in computational fracture mechanics as a phenomenological material law for describing the stress state around a crack tip. One of the primary questions is how exactly one defines the cohesive zone around the crack tip in a fracture problem, and how one determines the cohesive zone law for a given material system. The law is usually postulated based on some prior knowledge of the problem, and is iterated several times in to obtain agreement with known theoretical results and/or experimentally-observed behavior. To postulate the law, the user simply defines the key parameters, which form the shape of the law in Figure 1.4.

The cohesive zone is not limited to fracture problems of exclusively a single mode. The case of a mixed-mode fracture problem (i.e., mode-I and mode-II) can be modeled by accounting for the displacements that result in both the x_1 and the x_2 direction: the opening displacement δ_n, and the sliding displacement δ_t, respectively, as shown in the Figure 1.5.

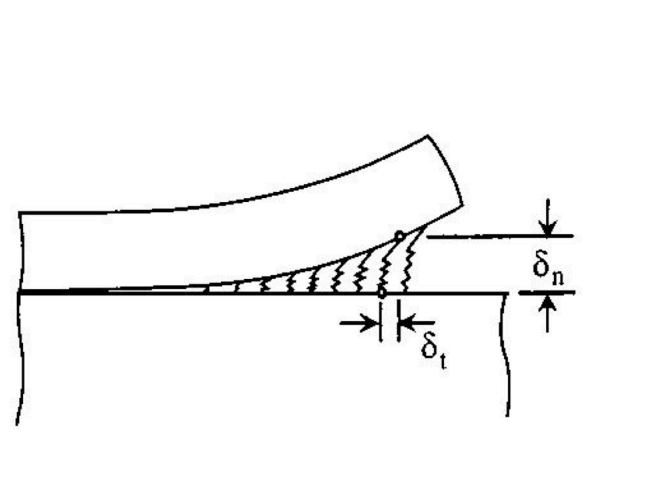

Figure 1.5: Opening displacement vs. sliding displacement in a mixed-mode fracture problem (from Hutchinson, 1992).

When a crack opens, the displacements that result can be separated into an opening displacement, δ_n and a sliding displacement, δ_t. The two displacement components are combined to express an overall displacement δ by

$$\delta = \sqrt{\delta_t^2 + \delta_n^2}. \tag{1.10}$$

In the context of finite element implementation, if limited or no knowledge is had of the magnitude of the opening and sliding displacements, a weighting factor β is introduced as shown in Eq. 1.11. This weighting factor can be tuned and simply represents a ratio that relates the two displacement components

$$\delta = \sqrt{\beta^2\delta_t^2 + \delta_n^2}. \tag{1.11}$$

In the case of a pure mode-I problem, as already discussed, $\beta = 0$. This parameter β is another term that can be implemented into a computational cohesive zone law. Hutchinson [42] and Hutchinson and Tvergaard [46] have done much work in developing applicable theory for a cohesive zone law for the mixed-mode case of a mode-I/mode-II fracture problem. In this case, the work per unit area needed to separate the interface is independent of the combination of crack face displacements leading to separation. The fracture energy is an extension of Eq. 1.8, where the effective displacement δ is used along with the opening and tangential stresses in both the x_1 and x_2 directions, respectively. The effective displacement and tractions are implemented using a non-dimensional crack separation measure

$$\lambda = \sqrt{\left(\frac{\delta_n}{\delta_n^c}\right)^2 + \left(\frac{\delta_t}{\delta_t^c}\right)^2} \tag{1.12}$$

and the fracture energy is

$$G = \delta_n^c \int_0^{\lambda} \sigma(\lambda') d\lambda'. \tag{1.13}$$

1.6 Objectives

This thesis examines the mechanics of the peel test through experiments, finite element simulations, and theoretical analysis with the aim of developing governing relations to describe the role of adhesion in the peel test for elastic adhesive tapes and in the fracture process in general. Chapter 2 discusses an experimental peel test configuration developed for the study and investigation of the peeling of elastic adhesive tapes. Displacement-controlled tests are conducted for a range of peel angles using Scotch MagicTape adhered to a rigid glass substrate, and the experimental results are compared to the governing relations of Rivlin and Kendall. By making the analogy that the fibrillation zone that develops in these tests is a cohesive zone in a fracture-based study, the opening displacements in the cohesive zone are measured experimentally via an imaging technique that is implemented and used during a peel test. The resulting information about the shape and size of the fibrillation zone is then utilized in Chapter 3 for conducting a finite element simulation. A series of simulations of the peel test are conducted, with the results compared to the experimental findings to determine the role of bending in the adhesive backing. Chapter 3 also presents a new theoretical framework in the context of finite deformation beam theory to extract a cohesive zone law from an

experimental peel test. Through extracting a cohesive zone law, the adhesion energy during a peel test is determined along with the force distribution in the process zone. This local method of determining the adhesion energy is compared to the global method used in the Rivlin model.

Chapter 4 investigates the rate-dependent effects of the peel test. Using the same experimental peel setup as in Chapter 2, tests are conducted for both Scotch Magic Tape and Scotch Packing Tape at different peel rates for a range of peel angles. The results are used to derive a rate-dependent power-law for the adhesion energy in a peel test as a function of the peel rate. The effects of varying different geometrical parameters during the peel test and how they affect the force distribution and adhesion energy are also discussed. Finally, a study of the stability including the role of compliance during a peel test using a newly developed force-controlled experimental configurations is discussed in Chapter 5. Experiments that monitor the tip position of an inextensible adhesive tape are conducted over time subject to a constant applied load at the tape extremity while the width of the tape is decreased as a function of the tape length. The stiffness of the system is varied by altering the magnitude and direction of the applied load during a test. This change in stiffness can be tuned in order to trigger or delay the onset of instability. Theoretical stability criteria are also presented for developing insights into the role of parameters investigated experimentally.

Chapter 2

Cohesive Zone Law Extraction: Experimental Methods

2.1 Introduction

The goal of this study is to treat the peel test described in Chapter 1 as a fracture mechanics problem and develop a cohesive zone law for a specific material system in a peeling configuration. An inverse formulation is used to extract a cohesive zone law from a series of experimental peel tests to describe the local stress behavior in the fibrillation zone that develops. This formulation will be described in the next two chapters, beginning with the current one, which details the experimental method and results used in this study. The development of a peel test configuration is described and validated with a series of experiments. By making the analogy that the fibrillation zone that develops in these tests is a cohesive zone in a fracture-based study, the displacement in the cohesive zone is measured experimentally via an imaging technique along with other relevant parameters to be described in this chapter.

2.2 Experimental Setup – Peel Test

For this study, an experimental configuration is developed for conducting a displacement-controlled peel test of an adhesive tape from a rigid substrate. Tests are conducted using Scotch Magic Tape (3M, Minneapolis, MN), a well-known adhesive system for comparison to known results in the literature for validation purposes. The

backing material of this tape is generally observed to be elastic, with the modulus obtained independently through a uniaxial tension test (the modulus measurement and method are described in detail in the next section). The width and the thickness of the tape backing are 19 mm and 50 μm, respectively.

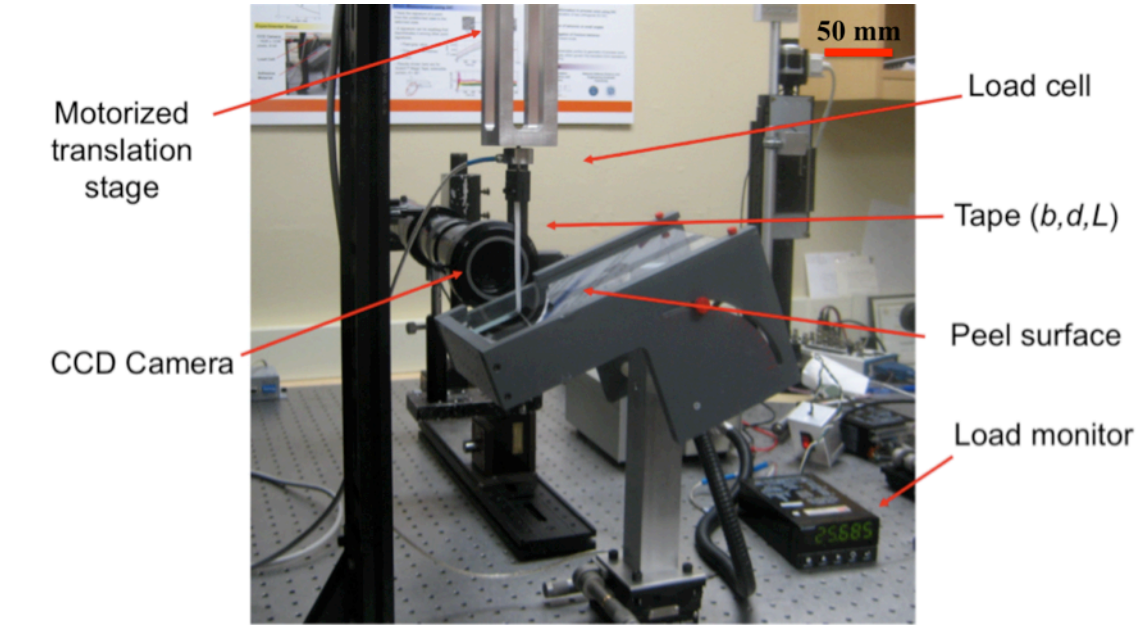

Figure 2.1: Experimental peeling configuration.

The experimental setup is shown in Figure 2.1. The peel base is constructed out of delrin, a commercial plastic, and mounted on an aluminum post. The base holds the glass substrate from which the tape is peeled, to be described later. The aluminum post is attached to 25-mm micrometer translation stages (Newport, Irvine, CA) to allow for precise alignment of the base. The base can be adjusted to obtain a range of angles from 0°-180° (0° to 90° in the configuration shown here; to obtain 90° to 180°, the base is turned around). The peel force P_f is measured at the end of the unadhered portion of the tape with a 500 g load cell (ALD-MINI-UTC-M, AL Design, Inc., Buffalo, NY). Since

the peel force increases significantly at lower angles, a 1.2 kg load cell from the same manufacturer is used for tests at 40° and lower, as for the widths of tape used in these experiments, the forces measured exceed the 500 g capacity load cell. The load is monitored in-situ with a digimeter (MD-40, Newport, Irvine, CA), configured to show the output force from the load cell in grams. The load cell is screwed into the end of an aluminum peel arm, which is attached to a motorized translation stage (M-410.CG, Physik Instrumente, Irvine, CA). The stage has a total travel range of 100 mm, a maximum velocity of 1 mm/s, and resolution of 100 nm. The stage is vertically mounted to an optical rail and used to apply a crosshead displacement (u), which peels the tape at a constant rate from a glass substrate. The glass substrate used is a generic piece of industrial grade lime glass cut to size with dimensions 203 x 127 x 3.175 mm (8” x 5” x 1/8”) for the length, width, and thickness, respectively. The glass substrate is held in a notched path on the inside perimeter of the peel base. On the top right hand side of the stage, two red screws are used as stops to keep the glass from moving during a test. Data is acquired for specific sampling rates and test times from the load cell through a virtual instrument created in Labview (DAQM02, National Instruments, Austin, TX).

Prior to testing, the glass surface is cleaned with acetone, followed by wiping with isopropanol, and left to dry. The adhesive tape is applied to the glass surface with a roller. Ideally, it appears that the longer the adhesive is left on the surface once attached before testing, the more steady a peel force can be obtained, along with more consistent results. To mitigate this phenomenon, all tests are conducted after the adhesive is left to rest for 20 minutes prior to testing. Due to the stochastic nature of this process, great care is taken in being consistent in the process of applying the adhesive to the surface.

The process zone in a peel test is defined as the region from the last detached fibril to the critical point where the fibrillation starts, which is the contact point between the adhesive tape and the glass substrate. A schematic of the process zone is shown in Figure 2.2.

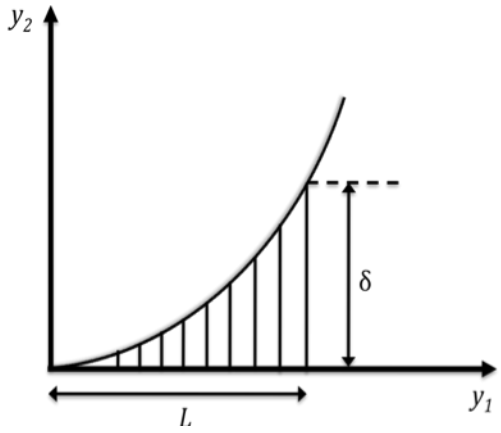

Figure 2.2: Schematic of the process zone in the peel test.

To investigate the fibrillation of the adhesive in the process zone, the geometry of the process zone is measured by acquiring in-situ images of the fibrils in the deformed configuration $(y_1 - y_2)$ using a 2-megapixel monochromatic digital CCD camera (UP-2000CL B/W, Uniqvision, Santa Clara, CA) attached to a long- distance video lens (K2/S Infinity, Boulder, CO). A sequence of images is acquired every 0.5 s for the duration of a peel test (typically 10 minutes) at a constant angle. Separate tests are conducted for peel angles ranging from 30° to 90°. The height and length of the zone are measured for each image using a simple post-processing scheme implemented in Matlab (MathWorks, Natick, MA).

2.3 Elastic Modulus Measurement

To consider any possible effects of the extensibility of the tape in the unadhered portion of the tape, the elastic modulus E must be determined. An specifically designed axial tensile tester is used to measure this value for the Scotch Magic Tape. The setup, shown in Figure 2.3, was designed for the testing of mechanical properties of soft materials such as hydrogels, rubbers, and other polymers. Shown in the figure is a hydration tank that is not used in the present measurements. It is used with the tensile tests for other studies involving the testing of materials in hydration, such as hydrogels.

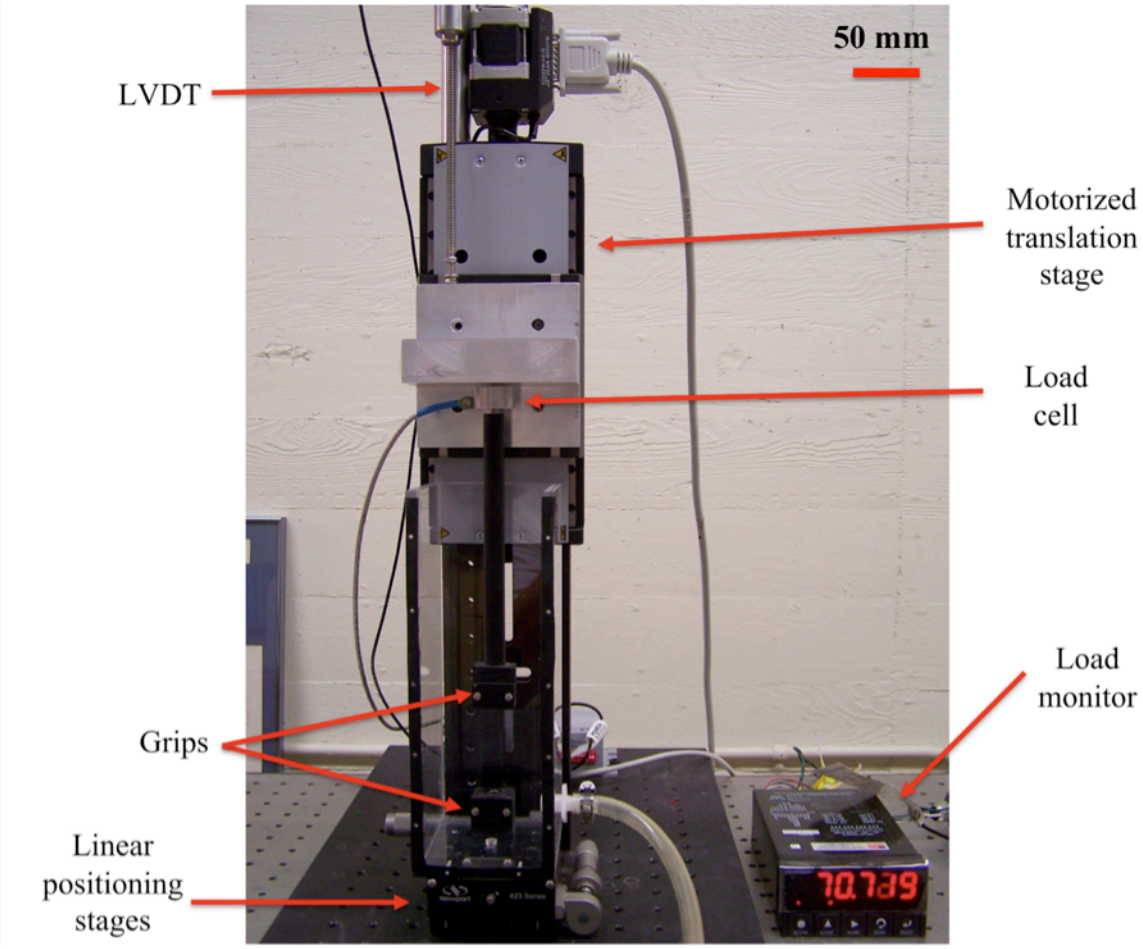

Figure 2.3: Tensile setup used for determining elastic modulus.

The tape is clamped between two grips manufactured out of delrin. The top grip is attached to a delrin rod, in-turn screwed on to the end of a 500 g load cell (ALD-MINI-UTC-M, AL Design, Inc., Buffalo, NY). The bottom grip is fixed upon two linear translation stages (Newport, Irvine, CA) for fine adjustment and alignment prior to testing. The load cell is attached to an aluminum T bracket, which is mounted to a motorized translation stage (M-410.2S, Physik Instrumente, Irvine, CA). The stage, a different model than that used with the peel test, has a maximum load capacity of 50 N, maximum stage velocity of 6 mm/s, and a resolution of 100 nm. The stage is mounted to a vertical optical rail and attached to an optical table.

The load is monitored in-situ with a digimeter (MD-40, Newport, Irvine, CA), configured to show the output force from the load cell in grams. The load cell output values are acquired with a virtual instrument created in Labview (DAQ-M02, National Instruments, Austin, TX). In order to measure the displacement, a linear variable differential transformer (Omega, Stamford, CT) is mounted on top of the translation stage, with its tip resting on the T bracket attached to the motor stage. The LVDT has a stroke length of ± 1.5mm and a resolution of 2.5 μm. While it may be sufficient to use the travel distance of the motor for the displacement in a given test, using the LVDT to directly measure the displacement is a more accurate method. In the case of extensible tapes such as the ones tested here, non-uniform deformations are not expected and thus this global method of measuring displacements and calculating strain should be sufficient.

Tests are conducted using samples of Scotch Magic Tape of dimensions length, width, and thickness of 117 mm, 19 mm and 50 μm, respectively. A plot of the nominal stress vs. strain in a tensile test is shown in Figure 2.4. The tests are conducted at a crosshead displacement rate of v = 10 μm/s, which is the same rate as the peel tests central to this study and described in the next section.

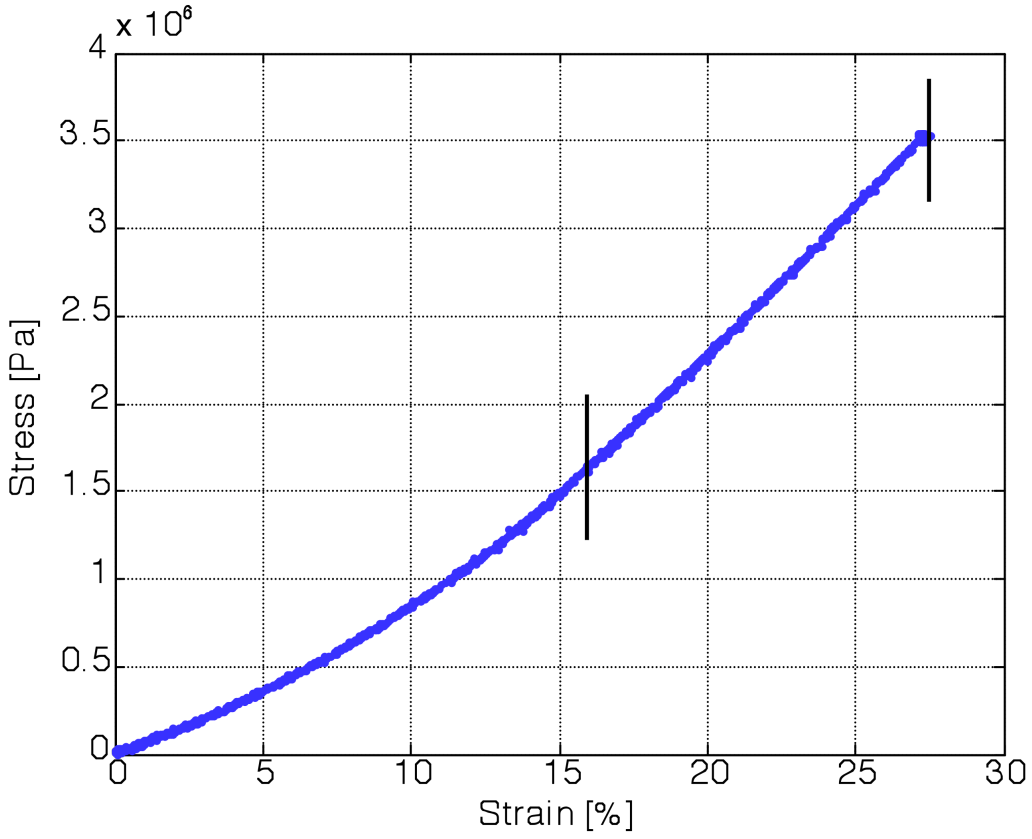

Figure 2.4: Stress vs. strain for Scotch Magic Tape obtained in a uniaxial test.

The elastic modulus is measured from the slope of the linear portion of the curve above, indicated by the two vertical black lines. For this set of 15 tests, the modulus is E = 1.65 ± 0.15 GPa, which agrees with values in the literature [34]. The non-linear portion of the curve, from the start of the test until about 17% strain, can be attributed to seating and slipping in the grips. To reduce slipping in the grips, sandpaper is adhered to both

sides of the grips in order to sandwich the tape between two pieces. However, since the LVDT is measuring displacement of the motor and not the actual displacement of the adhesive tape, the above result is useful only for obtaining a value of the elastic modulus, E. To investigate further stress-strain behavior such as failure stress, yield stress, and very large deformations, a more accurate displacement measurement method would have to be used. Since the focus of this study is not on exploring the mechanical behavior of adhesive tape in tension, the above result is sufficient for this investigation.

2.4 Steady-State Peel Force

Using the peel configuration described in Section 2.2, peel tests are conducted for Scotch Magic Tape through a range of angles with the objective of determining the steady-state peel force P_f. Figure 2.5 shows a typical plot of the peel force vs. time for a 90° peel test at a rate of v = 10 μm/s.

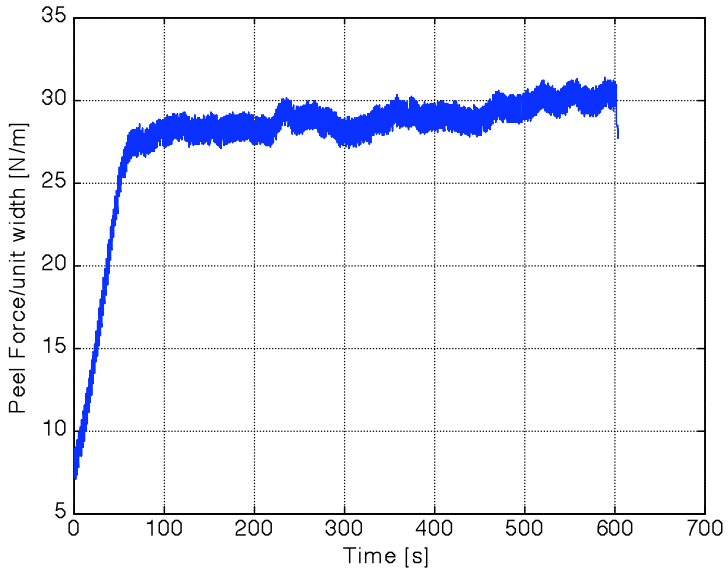

Figure 2.5: Peel force (P_f) vs. time (t) for a 90° peel test at a rate of v = 10 μm/s.

A pre-load is applied to ensure that the sample is taut prior to commencing peeling. As the adhesive is peeled, the force increases until it levels off at a roughly steady-state value. This is the steady-state region, where the focus of this study is directed. The peel force P_f used for each test is taken as an average of its values in the steady-state region. The peel base does not move horizontally as the sample is peeled. Thus, towards the end of the test, the load increases slightly due to a small decrease in peel angle θ. This change has been observed to be ~1°, and is consistent with slight increase in steady-state peel force in Figure 2.5

Peel tests are conducted for angles of 30° to 90° at 10° increments. A total crosshead displacement of 6 mm is imposed at a rate of 0.01 mm/s, and the peel force (P_f) is measured over a time period of 10 minutes. The tape used in the investigation has width, b =19 mm (3/4") and thickness, h = 50 μm. The measured steady-state peel forces are plotted as a function of the peel angle in Figure 2.6 and compared to those predicted by the Kendall and Rivlin models. Recall from Chapter 1 these relations given for a linearly elastic extensible (Kendall) and inextensible (Rivlin) tape

$$G = \frac{F^2}{2Eb^2h} + \frac{F}{b}(1-\cos\theta) \tag{1.6}$$

$$\frac{P_f}{b} = \frac{G}{1-\cos\theta}. \tag{1.7}$$

In the Kendall model (Eq. 1.6), the elastic modulus of the tape backing material is E = 1.65 GPa, obtained independently through a uni-axial tensile test described in Section 2.3. The values of adhesion energy used in both models are determined from the

experimentally measured 90° peel force, which in this case is G = 34.5 N/m. This value is employed for calculating the theoretical peel forces at the lower angles. Figure 2.6 shows that the peel forces correlated by the two models begin to exhibit a difference at small peel angles, due to the important role of the elastic energy term associated with stretching. However, for the range of peel angles (30°-90°) investigated in this study, the difference is negligible, which validates the inextensibility assumption for the present work. Compared to both model evaluations, the measured peel forces show good agreement within experimental scatter.

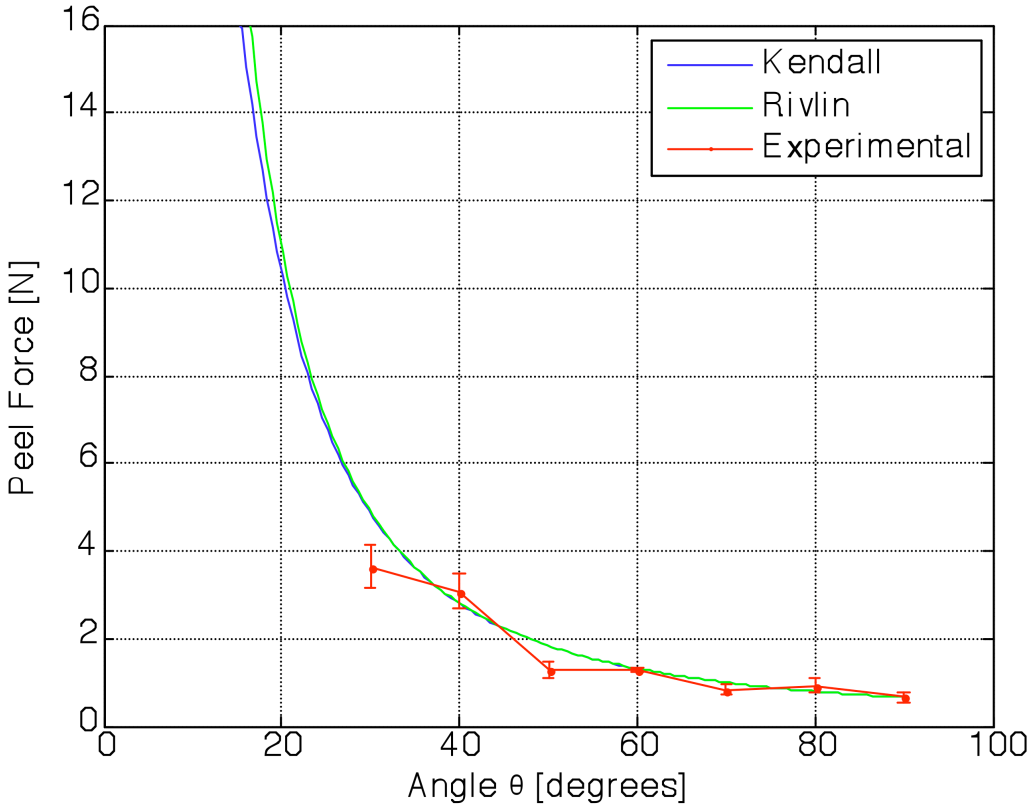

Figure 2.6: Measured steady-state peel force (P_f) vs. peel angle (θ).

One aspect that is of interest is whether or not the adhesion energy G is a function of the peel angle. This will be investigated in detail in Chapter 4.

2.5 Process Zone Characterization

The process zone analysis is aimed at examining two phenomena: the steady-state behavior of the process zone geometry, and the dependence of the geometry on the peel angle. The process zone image in a representative test is shown in Figure 2.7. The image here is acquired for a peel angle of $\theta = 90°$ after the steady-state peel force has been achieved.

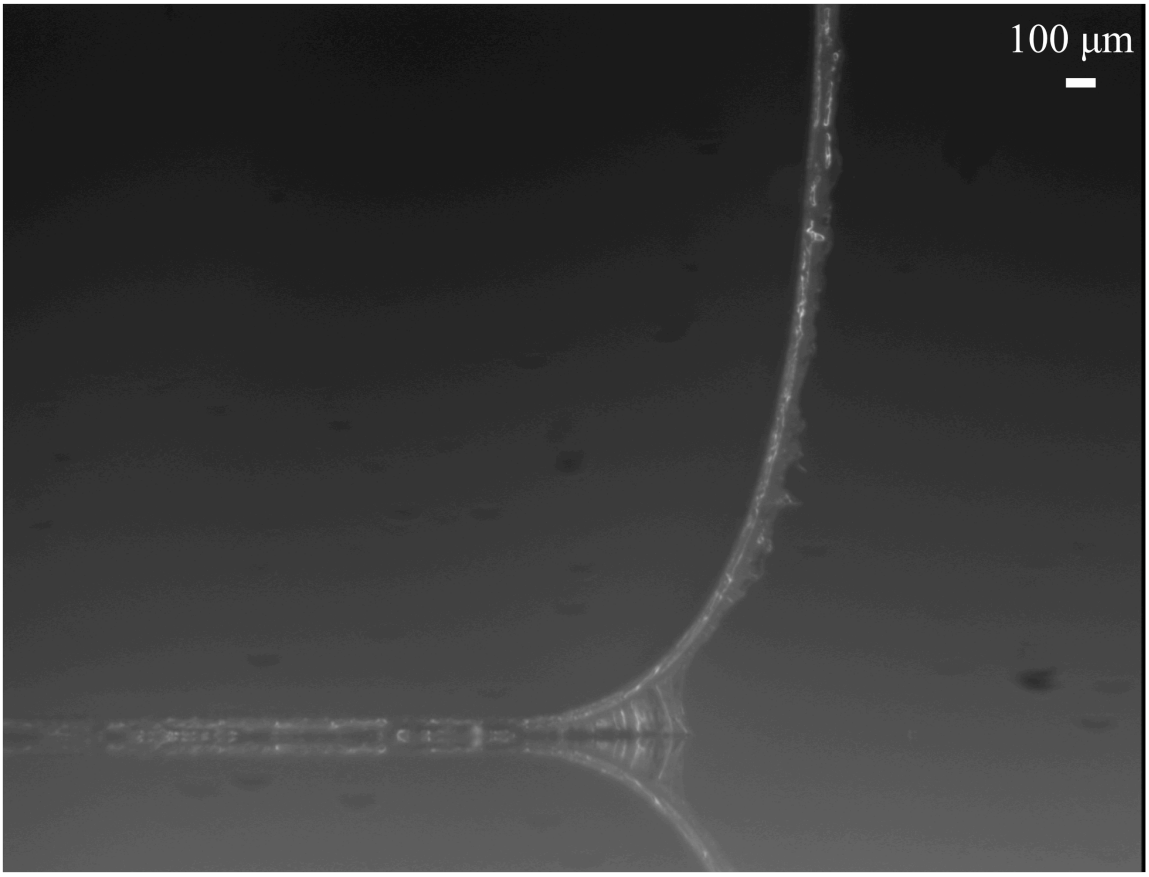

Figure 2.7: Image of the process zone for a 90° peel test.

From this image, the fibrillation zone can be quantified clearly. The last attached fibril can be identified, which defines the end of the cohesive zone. While the origin of the zone is more difficult to locate accurately at this resolution, it is identifiable enough at a given angle to see a trend in the zone size as a function of angle. This will be seen in more detail in subsequent sections. To determine the length scale from the image, an image of sets of line pairs from a 1951 USAF target grid is acquired prior to testing. This image allows for determination of the scaling factor in units of mm/pixel.

The parameters of interest from these tests are the length and height of the process zone L and δ, respectively, as well as the shape of the backing material in the process

zone. The radius of curvature of the backing can be described analytically with a mathematical function, which will be explored in detail in the next chapter. Figures 2.8 and 2.9 show images of the process zone for tests at lower peel angles of 70° and 30°.

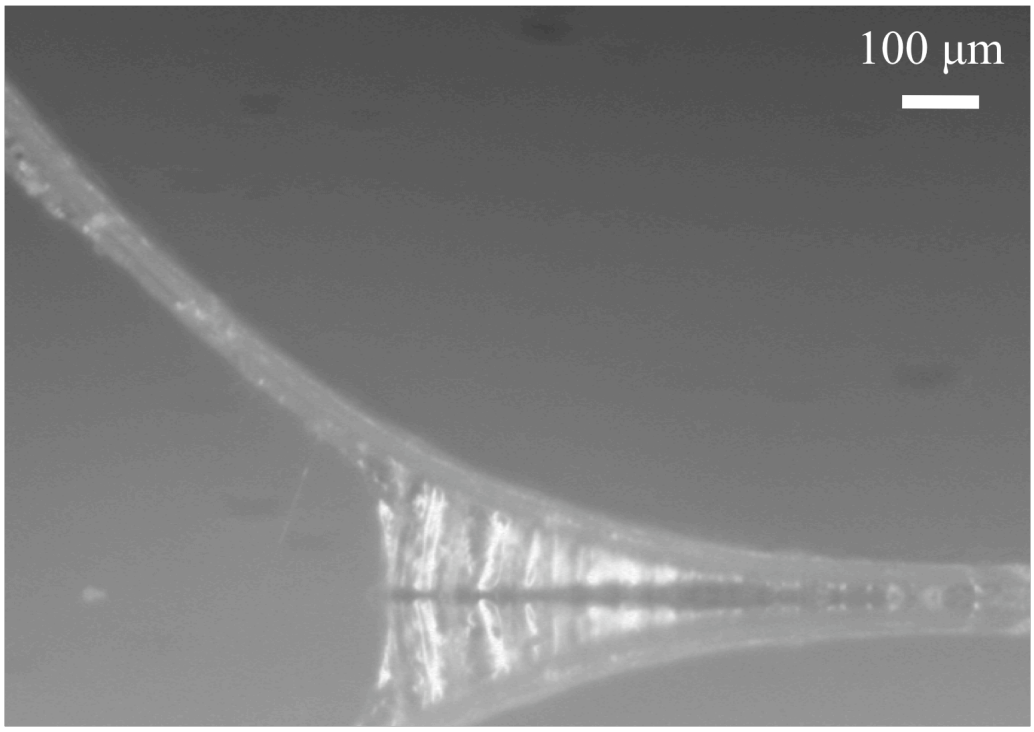

Figure 2.8: Image of the process zone for a 70° peel test.

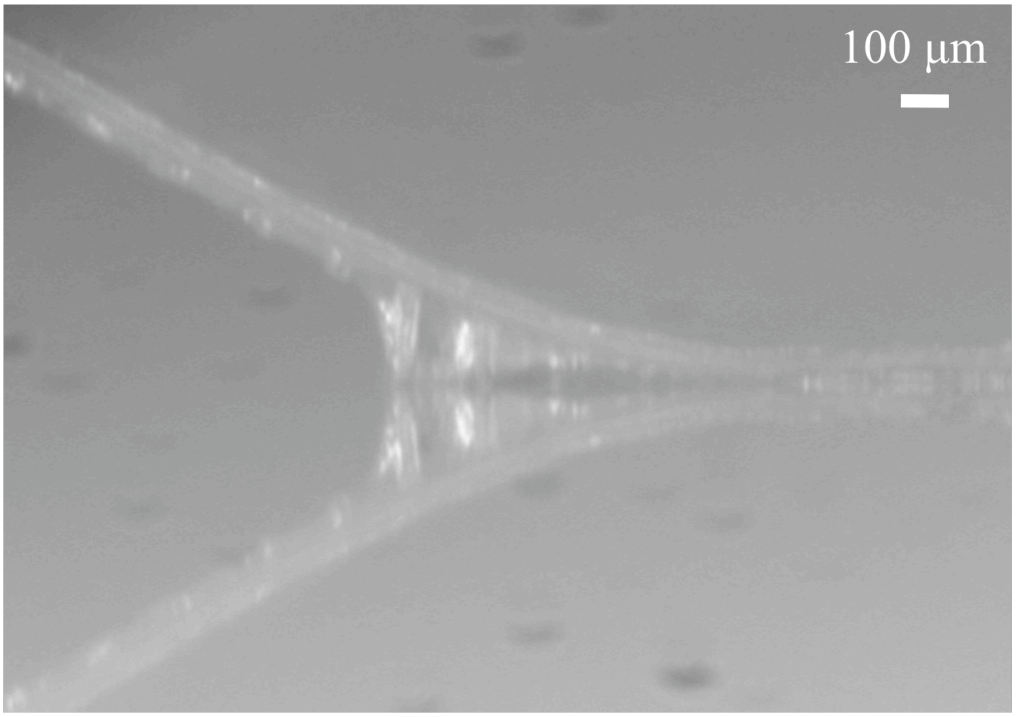

Figure 2.9: Image of the process zone for a 30° peel test.

Prior to quantitative analysis of the fibrillation, there are some qualitative results that can be seen by comparing the images of the process zones at the three different peel angles shown here (Figs. 2.7-2.9). The size of the process zone appears to change as the peel angle changes. Specifically, the length of the zone (L) appears to increase with increasing peel angle. Another interesting observation is that to a good approximation, the fibrils appear to remain perpendicular to the glass substrate throughout the process zone. If the schematic in Figure 1.5, comparing a sliding versus an opening displacement, is considered, the opening displacement appears to dominate any sliding displacements that are present. This will be investigated in detail in Chapter 3. To examine how the shape of this process zone potentially changes during the steady-state, five separate images at equal time increments (100 s) through the steady-state phase are quantified. Figure 2.10 shows the shape of the process zone for these five individual time steps in a

90° peel test. The time increments are color-coordinated, as shown in the legend of Figure 2.10.

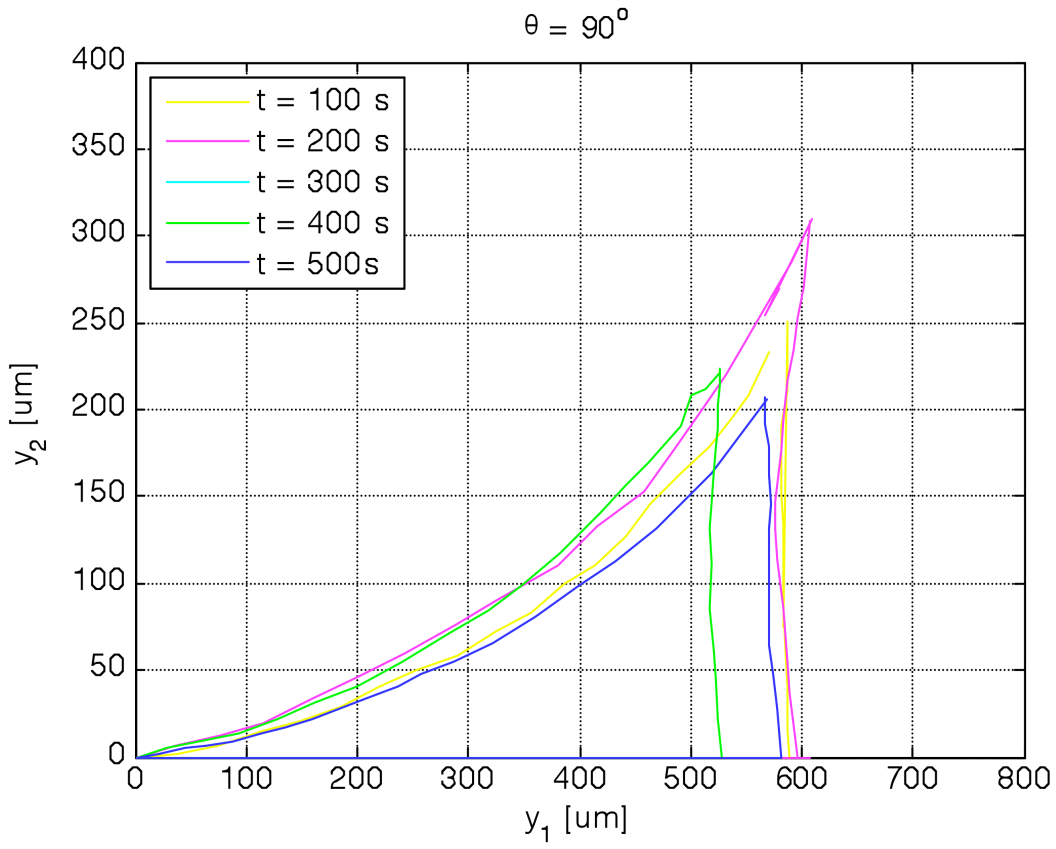

Figure 2.10: Process zone shape at five separate time increments in the steady-state regime throughout a 90° peel test.

As is seen here, the shape of the zone remains fairly constant during the steady-state period for a single peel test at $\theta = 90°$. Examining the steady-state process in the same manner for peel angles down to 30°, Figures 2.11 to 2.16 show the similar behavior for similar time increments. The colors for the shapes in each plot represent the same time increments as in Figure 2.10.

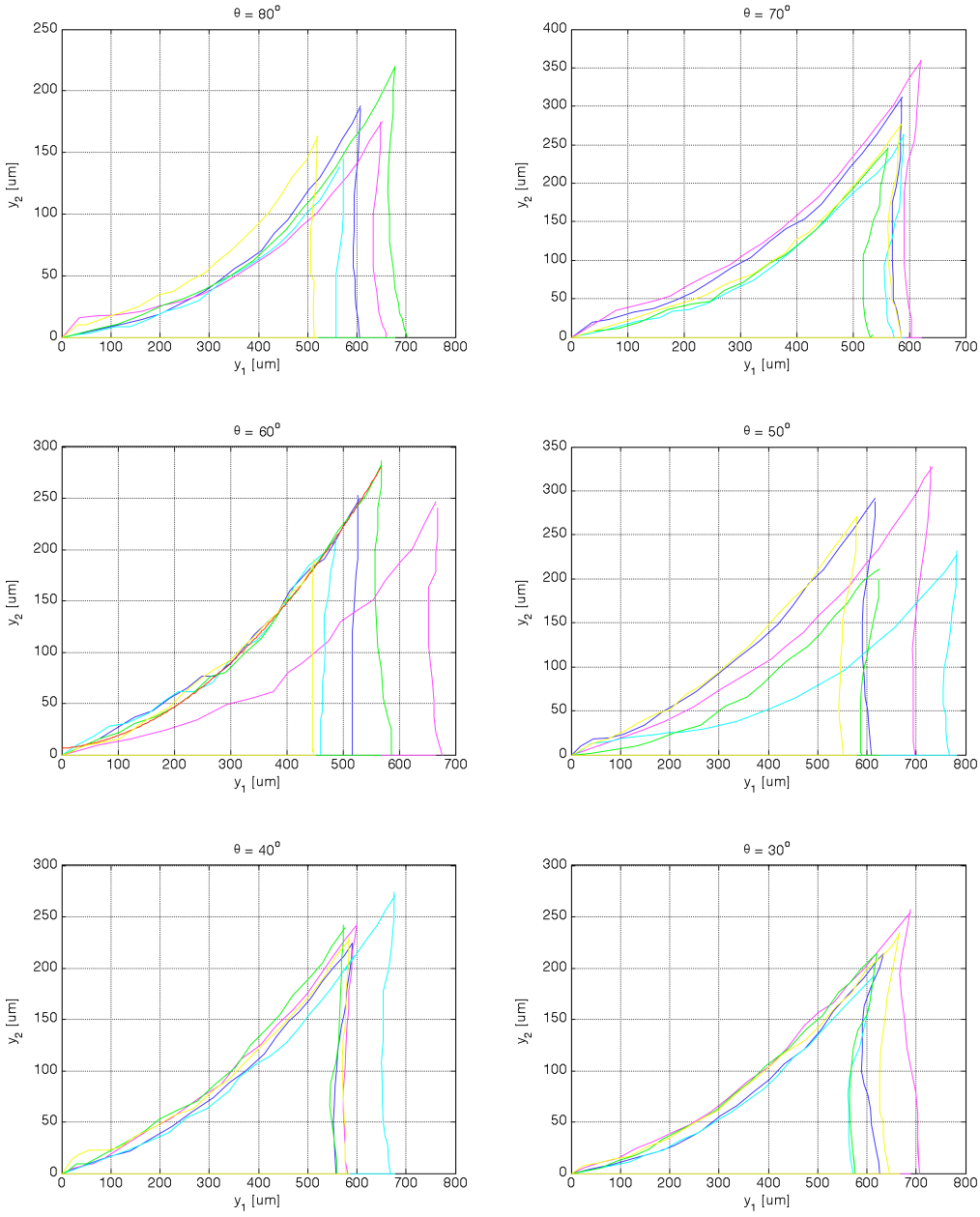

Figures 2.11 to 2.16: Process zone shape at five separate time increments in the steady-state regime for peel angles θ = 80°, 70°, 60°, 50°, 40°, 30°.

There is some variation in the shape of the process zone for all angles, but for the most part it can be concluded that the geometry of the process zone remains constant for the steady-state process within a 10-15% experimental scatter. Table 2.1 shows the

average size of the process zone for a single test for each angle at the varying time increments.

θ	L [μm]	δ [μm]
90	574 ± 27	242 ± 39
80	602 ± 69	177 ± 29
70	576 ± 27	291 ± 45
60	538 ± 95	234 ± 40
50	643 ± 87	267 ± 47
40	589 ± 46	242 ± 19
30	626 ± 55	221 ± 25

Table 2.1: Average process zone size for five separate time increments for a single peel test at a given peel angle.

Since the shape of the zone will be treated as constant irrespective of time during the steady-state process based on the aforementioned results, the shape is taken to be the average of the five randomly-selected instances in time during a single test. However, the reproducibility between tests for a given angle must be examined as well. Examining the case of $\theta = 90°$, Figure 2.17 compares the shapes of the process zone for five separate peel tests conducted at this angle.

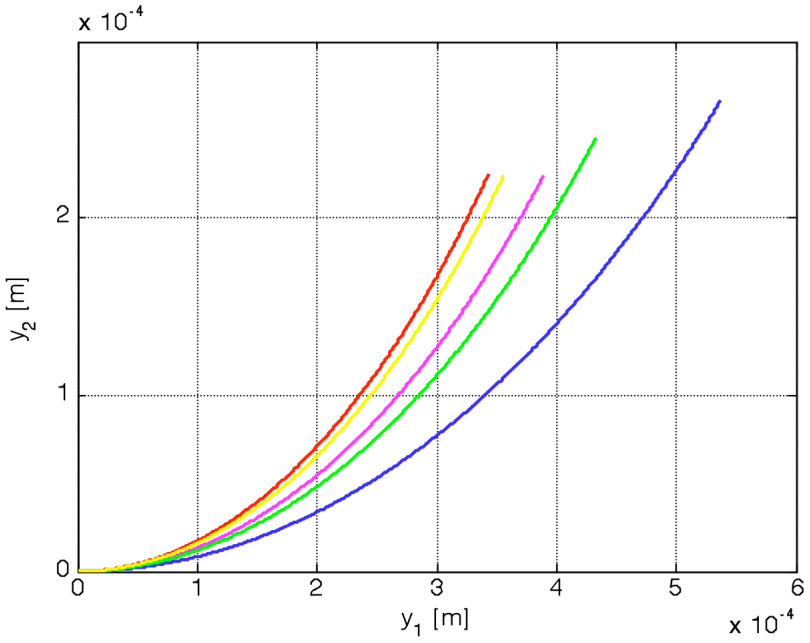

Figure 2.17: Process zone shape for five separate 90° peel tests.

For five separate tests, there is good consistency for all but one test (the blue curve), which itself is not far from the other four shapes. The average values for the entire range of peel angles (30° to 90°) are given in Table 2.2 using data from the five separate peel tests at each angle. Note the difference between the values in Tables 2.1 and 2.2. Recall that the values of L and δ in Table 2.1 are the averages of the process zone for a single test at each angle for five separate time increments.

Peel Angle θ	L [μm]	δ [μm]
90	412 ± 78	226 ± 21
80	505 ± 11	212 ± 51
70	523 ± 22	223 ± 39
60	634 ± 0.7	259 ± 23
50	600 ± 85	207 ± 30
40	621 ± 78	222 ± 21
30	617 ± 32	181 ± 22

Table 2.2: Process zone sizes for varying peel angles.

As is seen for all of the angles in Table 2.2, the error for the process zone size is roughly 20% at a given angle. Having established that the process zone can be quantified within a given test and from multiple tests, it is important to examine the dependence of the geometrical parameters on the peeling angle e.g. $L(\theta)$, $\delta(\theta)$. The plots below in Figures 2.18 and 2.19 show the relationship between the length and height of the process zone for peel angles from 30° to 90°.

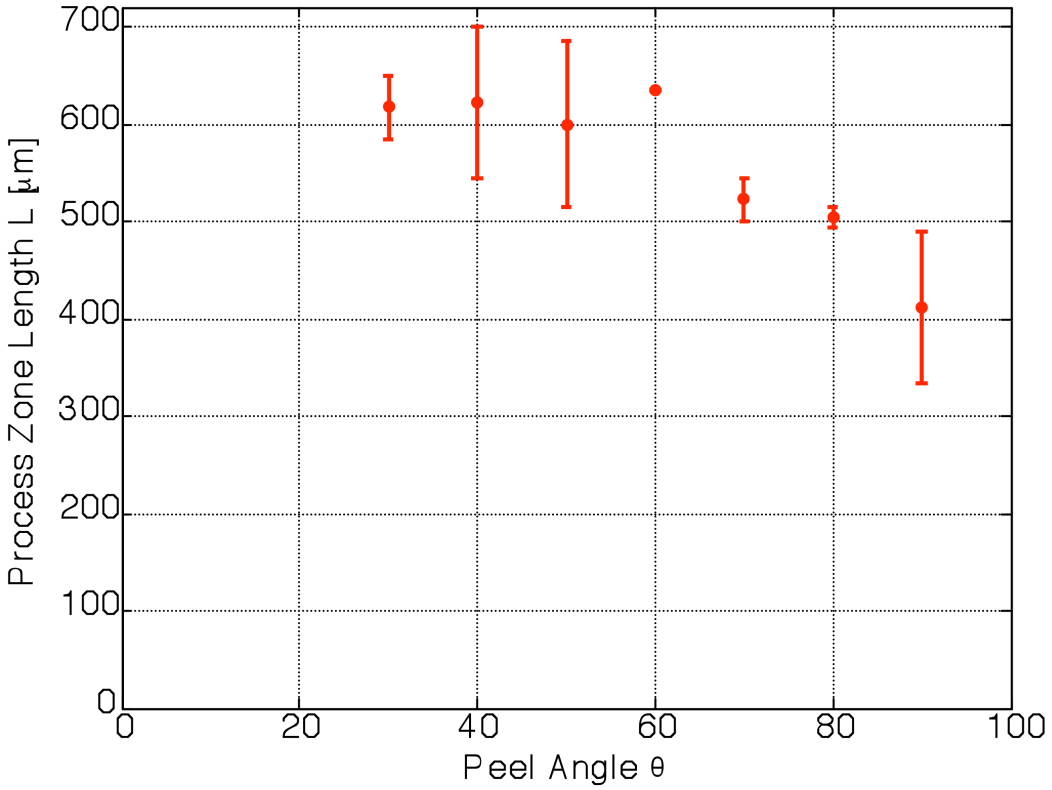

Figure 2.18: Process zone length (L) vs. peel angle (θ).

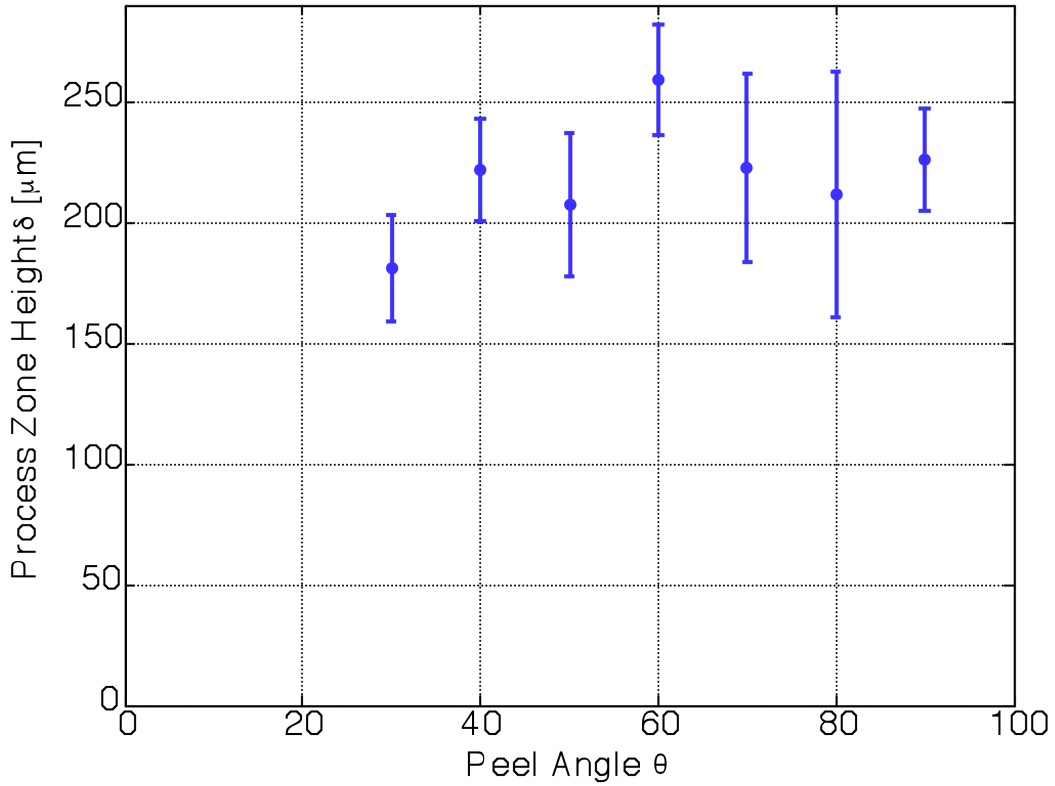

Figure 2.19: Process zone height (δ) vs. peel angle (θ).

Figure 2.18 shows a definite increase in the length of the process zone L as the peel angle θ decreases. As for the height of the process zone δ, it seems to remain relatively constant independent of the peel angle.

2.6 Conclusions

This chapter described the experimental methods developed and implemented as the basis for extracting a cohesive zone law from a series of experimental peel tests for linearly elastic adhesive tapes. The elastic modulus of the candidate material, Scotch Magic Tape, is determined using a separate tensile test arrangement. An original experimental peel test is developed and the steady state peel force is compared to the

well-established Rivlin and Kendall models available in the literature. Using a simple imaging technique, the process zone during a peel test is quantified for a range of peel angles by examining the fibrillation that occurs during debonding. The shape of this process zone remains constant throughout the steady-state process for a given angle. For a range of peel angles 30˚ to 90˚, the length of the process zone increases as the peel angle decreases and the height of the process zone appears to remain constant for the same range of peel angles.

Chapter 3

Cohesive Zone Law Extraction: Finite Element Simulation and Non-Linear Beam Theory

3.1 Introduction

To extract a cohesive zone law from the experimental peel tests described in the Chapter 2, a theoretical framework is developed to model the peeling configuration appropriately. To determine the proper framework, a finite element simulation is developed to examine the mechanical behavior of the tape backing in the process zone. This finite element simulation motivates the treatment of the tape as a non-linear beam adhered to rigid substrate, with a cohesive zone equivalent to the fibrillation zone observed in experiments. Upon fitting the shape of the experimental profile of the process zone with an analytical function, this fit is implemented into the theoretical framework described here. A full-field force distribution in the process zone is obtained for a range of peel angles from 30˚ to 90˚, and the cohesive zone laws at each of these angles is extracted. From the cohesive zone curves, the adhesion energy can be determined with this local process zone method and compared to the global method of determining the adhesion energy proposed by Rivlin [18].

3.2 Finite Element Formulation

Prior to developing a relevant theoretical framework for modeling this problem and extracting a cohesive zone law, a finite element simulation is conducted to investigate the

behavior of the peeling configuration. The goal of this analysis is to investigate the possible effects of bending as the tape is peeled from the rigid glass substrate, specifically with regard to the effects of the bending stiffness in the adhesive backing. Based upon inspection, the axial force in the tape backing is proportional to Eh, where E is the elastic modulus and h the thickness of the tape backing. The bending moment in the backing is proportional to Eh^3. Thus, by altering the modulus and thickness of the backing, the axial force is kept the same while effectively changing the bending stiffness. This relation is explored in detail in the context of the finite element simulation presented here.

The geometry of the peeling configuration as modeled in the simulation is shown below in Figure 3.1.

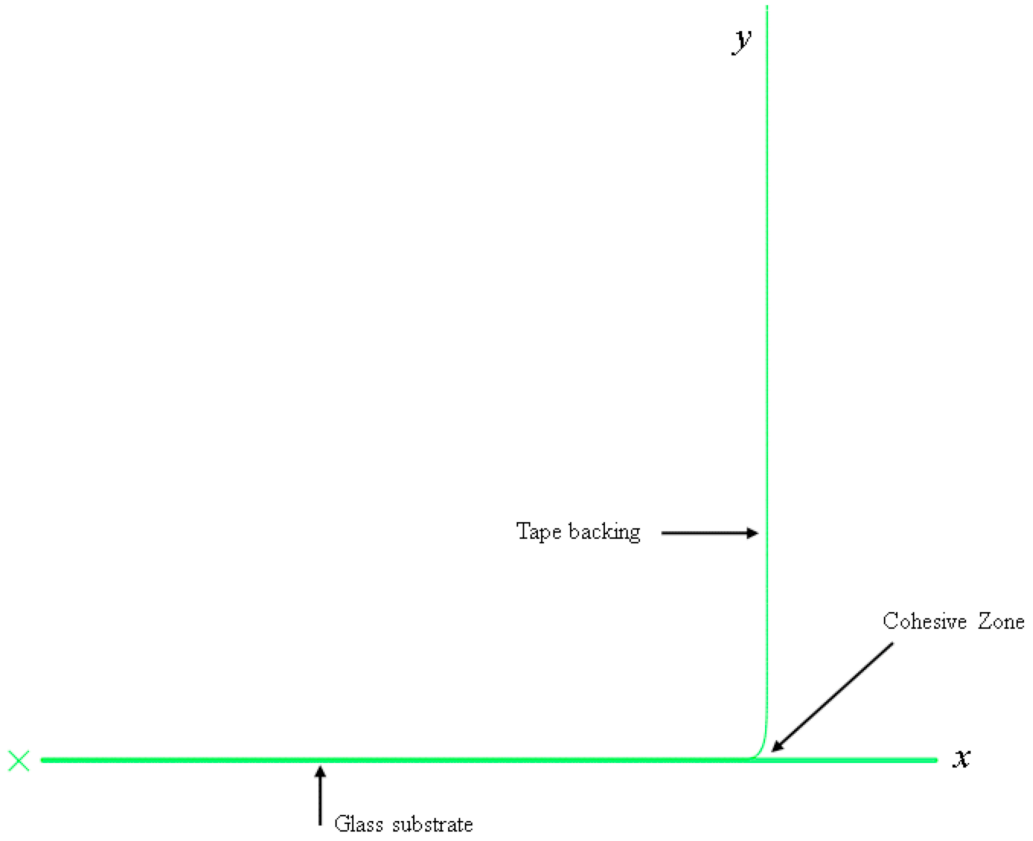

Figure 3.1: Schematic of the finite element formulation of the tape peeling process.

The problem is formed as a 2D plane (*x*-*y*) problem using Abaqus Standard [47] assuming unit width in the *z* direction. The glass substrate is treated as a rigid solid, such that all deformation is confined to the adhesive and the cohesive zone between the adhesive and the substrate. The adhesive backing is modeled as a Bernoulli-Euler beam. 2D linear beam elements are used to mesh the adhesive, with thickness, h = 50 μm and width, b = 1 mm.

While the overall goal of this study is to derive a cohesive zone law for the process zone from an experimental peel test, a separate user-defined cohesive zone law is implemented into the finite element simulation solely to investigate the global mechanical behavior of the adhesive. This is implemented by considering the adhesion energy, G from the global energy balance described in Chapter 1. The estimation provides valuable insight into applicable theory for extracting a more precise cohesive zone law from the experimental data acquired in Chapter 2 during a peel test.

Using a coordinate frame y_1-y_2 in the deformed configuration, a power-law cohesive zone law of the following form,

$$\sigma(y_2) = \sigma_0\left(1 - \frac{y_2}{\delta}\right)^n \tag{3.1}$$

is used, where σ_0 is the stress in the cohesive zone at y_2 = 0. Initially, the simulations were performed for n = 0 (e.g., constant cohesive zone stress). The stress in the cohesive zone can be estimated by considering the Rivlin equation (Eq. 1.7). Recall that

$$G = \frac{P_f}{b}(1-\cos\theta). \tag{1.7}$$

Since the adhesion energy, G is the area under the cohesive zone law curve $\sigma(y_2)$, one can determine σ_0 from

$$\sigma_0 = \frac{P_f}{b\delta}(1-\cos\theta) \tag{3.2}$$

where δ is the height of the process zone, measured experimentally. The hypothesis here is that a global energy balance of the entire system can also be used to describe the energy locally in the process zone as originally proposed by Rivlin.

To input the cohesive zone law into Abaqus Standard, a user-defined script is implemented using Fortran following the method of Camacho and Ortiz [48]. For purposes of comparison in this investigation, a constant cohesive zone law is used, as is seen for a constant peel angle and tape width from Eq. 3.2. A schematic of this law is shown in Figure 3.2. The goal here is to implement the same cohesive zone law while varying the elastic modulus and thickness to investigate the effects of bending, independent of what the specific cohesive zone law may be. As previously mentioned, the specific cohesive zone law, which is the goal of this study, will be derived later in this chapter.

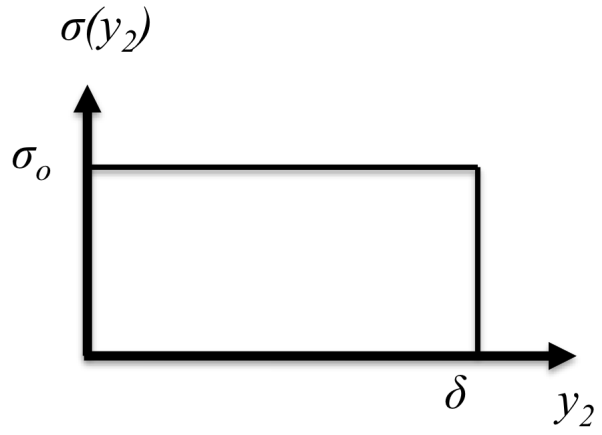

Figure 3.2: Schematic of the constant cohesive zone law $\sigma(y_2)$ used in the finite element simulation.

The finite element simulation is conducted by imposing a displacement at the end of the tape backing. The output from the simulation gives the force along the tape backing as a function of position for the entire length of the tape. The length of the process zone L will also be obtained from the simulation and compared to the experimentally measured length L from the experimental results. The peel arm here is set to be the same length as in the experimental tests described in Chapter 2.

3.3 Finite Element Results – Experimental Case

A simulation is performed as formulated in the previous section for a peel angle of θ = 90˚. The total computation time is approximately ten minutes on an Intel Core™2 Duo 2.4 GHz processor. To investigate the experimental version specifically, an initial test is conducted using parameters from the measurements in Chapter 2. The input parameters include the material properties of the tape (E = 1.65 GPa (Young's modulus), ν = 0.2 (Poisson's ratio)), the initial peel arm length (L = 75 mm), and the displacement to be applied at the end of the tape (u = 120 mm). The cohesive zone law is input using the

experimental opening displacement (the height of the process zone), δ = 222 µm, the experimentally-measured peel force P_f = 34.5 N/m, and the value of σ_0 calculated from Eq. 3.2 for this case, $\sigma(y_2)$ = 0.27 MPa.

A plot of the axial force along the curve following the shape of the tape backing, denoted *S11* in the plot, is shown in Figure 3.3 for a region local to the process zone. The direction of *S11* is in a coordinate system where a curve *s* is defined to follow the backing of the tape. This choice of coordinates is described in detail in a subsequent section. The cohesive zone is also shown in the plot.

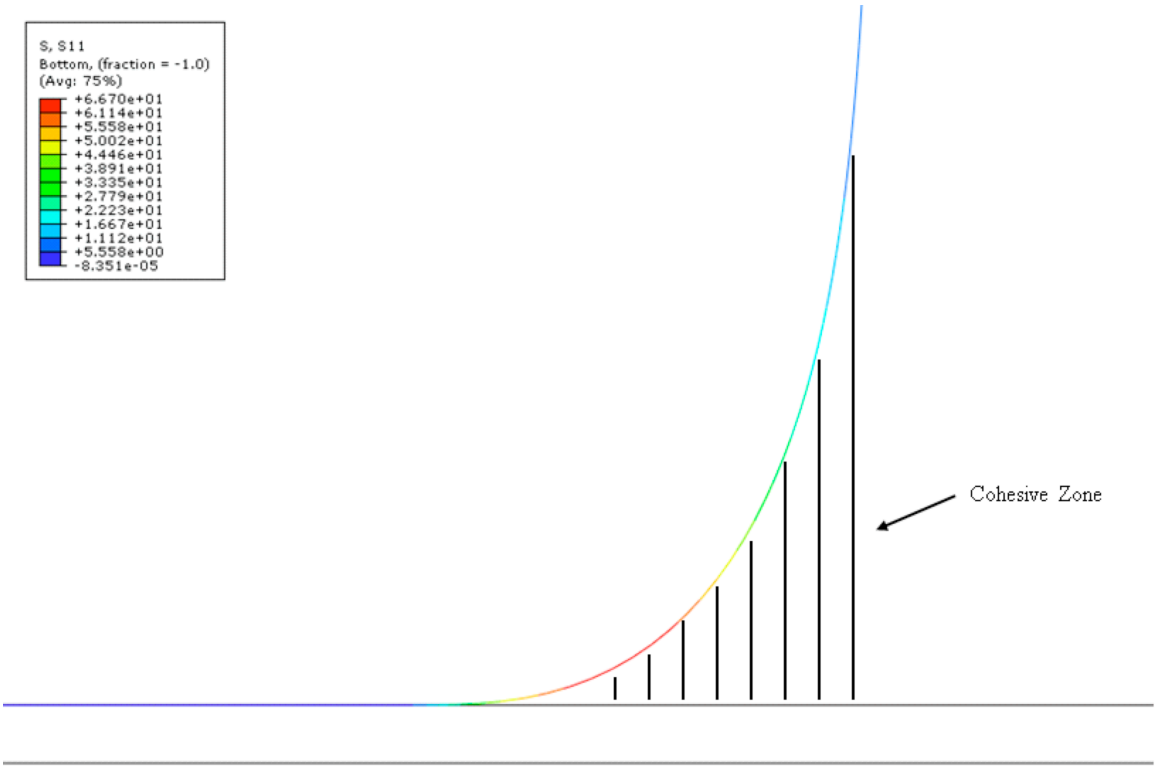

Figure 3.3: Axial force, denoted *S11*, along the tape backing in a simulation for θ = 90°.

The plot in Figure 3.3 provides insight into several interesting features. From a qualitative view of the contour plot, the axial force in the process zone is not constant.

Experimentally, recall that the peel force is measured at a point far away from the process zone. Based upon the result in Figure 3.3, it can be concluded that the far-field steady-state peel force itself is not equivalent to the forces in the process zone.

Another observation that can be made is that at the end of the process zone, the peel angle θ is not 90°, which is the far-field peel angle employed in the simulation. The backing therefore has some curvature at this point, which reflects the presence of bending stiffness. Consider if the backing of the tape is modeled with no bending stiffness. In this case, the curvature that exists in the backing is induced by the cohesive zone force, σ_0. Outside of the process zone, where the cohesive zone force is equal to 0, there are no forces acting on the backing and therefore no curvature should be present.

In order to verify the cohesive zone law that is input for this instance, the cohesive zone force is plotted in Figure 3.4 as a function of the position x in the deformed configuration.

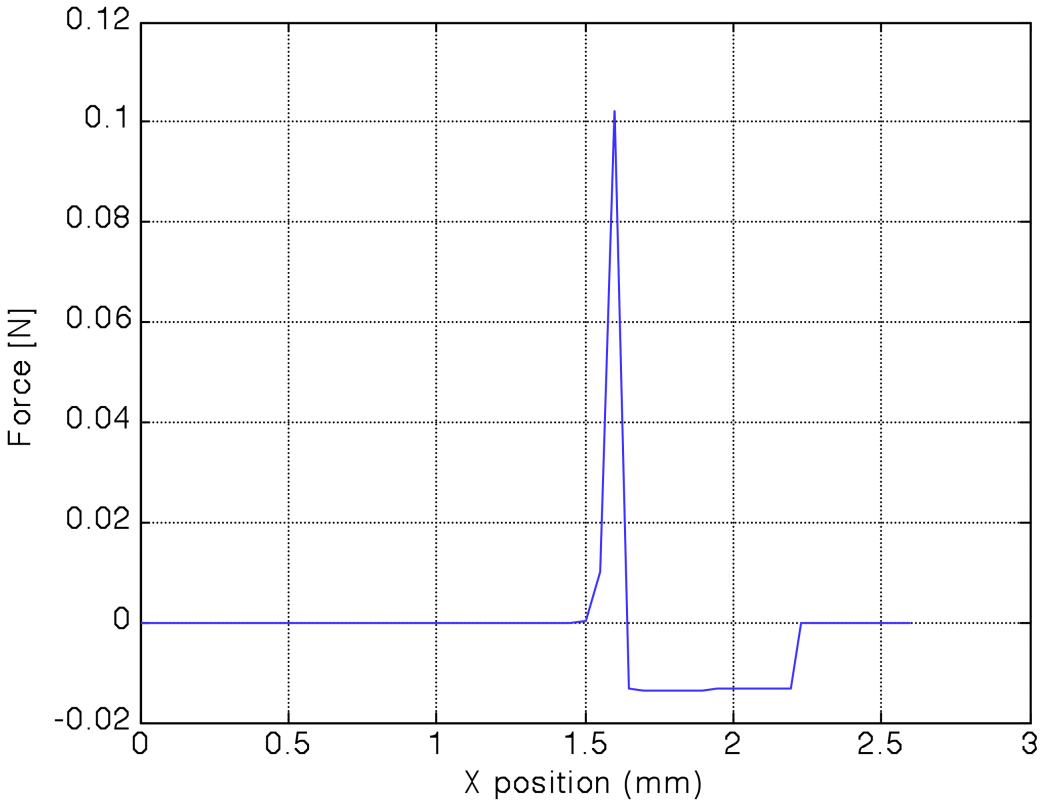

Figure 3.4: Contact cohesive force as a function of horizontal position, x in the deformed configuration.

The element size in this simulation is 50 μm. The origin of the process zone is at the position x = 1.5 mm, while the end of the end of the process zone is at x = 2.2 mm. The explanation for the spike at the origin of the process zone can be explained by the singularity that develops at the crack tip [42]. From x = 1.7 mm to 2.2 mm, there is a drop in the contact force of 0.0135 N, which corresponds to the cohesive zone force of the same value in the opposite direction being applied. This contact force is monitored along the substrate, hence explaining why the force is negative in Figure 3.4. The length, L of the process zone here is 730 μm, which is larger than the length in the experimental results.

From the contour plot of *S11*, the axial force along the adhesive backing can be quantitatively determined. This force, denoted *P(s)*, is plotted as a function of the horizontal position, *x*, along the tape backing in Figure 3.5.

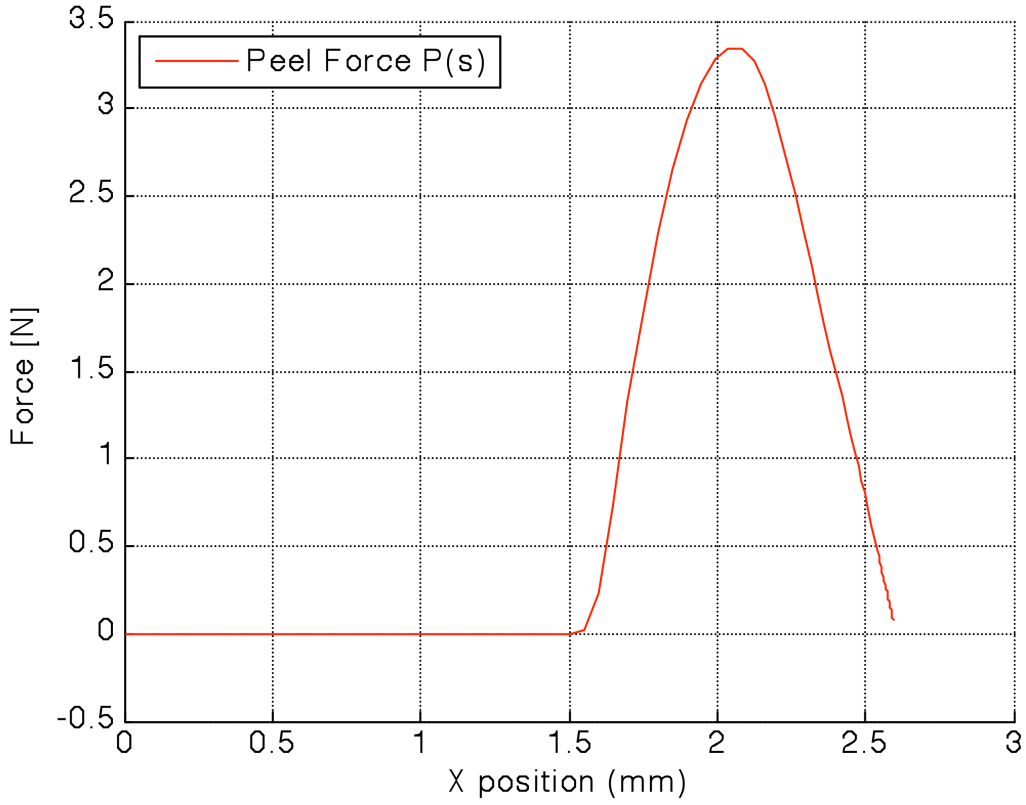

Figure 3.5: Axial force, *P(s)*, vs. position, *x* in the deformed configuration.

As suggested by the contour plot in Figure 3.3, the axial force does not remain constant in the process zone. The peak axial force occurs at $x = 2$ mm, which does not correspond with the edge of the process zone. At the end of the process zone, the axial force is 2.7 N, which is not equivalent to the far-field peel force P_f. Compared to the contact cohesive force, the axial force dominates the force distribution.

3.4 Finite Element Simulation - Parametric Study

Now that the experimental results have been simulated, the input parameters for the elastic modulus E and the tape thickness h are altered to simulate a beam with different bending stiffness. These simulations were performed to gain insight into the role of bending stiffness on the process zone geometry. Two cases are considered here: the first, where the modulus E and the thickness h are increased and decreased by a factor of 10, respectively, and then the second case by a factor of 100. This will effectively decrease the bending stiffness of the beam, as well as keep the axial force $P(s)$ the same for all cases while altering the bending stiffness of the beam.

To achieve convergence for these simulations, it is also necessary to change the constant cohesive zone force, σ_0 and the opening displacement, δ. To keep the energy G the same as in the simulation, the two parameters are similarly increased and decreased by the same factors of 10 and 100 as with the modulus, E and opening displacement, δ. A summary of the parameters used for these simulations is given in Table 3.1.

Simulation #	E	h	δ	σ_0
1 (Experimental)	1.65 GPa	50 μm	0.222 mm	0.27 MPa
2	16.5 GPa	5 μm	2.22 mm	0.027 MPa
3	165 GPa	0.5 μm	22.22 mm	0.0027 MPa

Table 3.1: Summary of input parameters used in the finite element simulations for different bending stiffnesses.

Simulations are conducted for cases 2 and 3 in Table 3.1, and the process zone is quantified. Figure 3.6 shows the shapes of the process zone for each of the two cases

described in this section, along with the profile from the experimental simulation (blue), denoted in a y_1-y_2 coordinate frame. The curves shown represent the shape of the tape backing. The profiles are normalized by the respective opening height, δ.

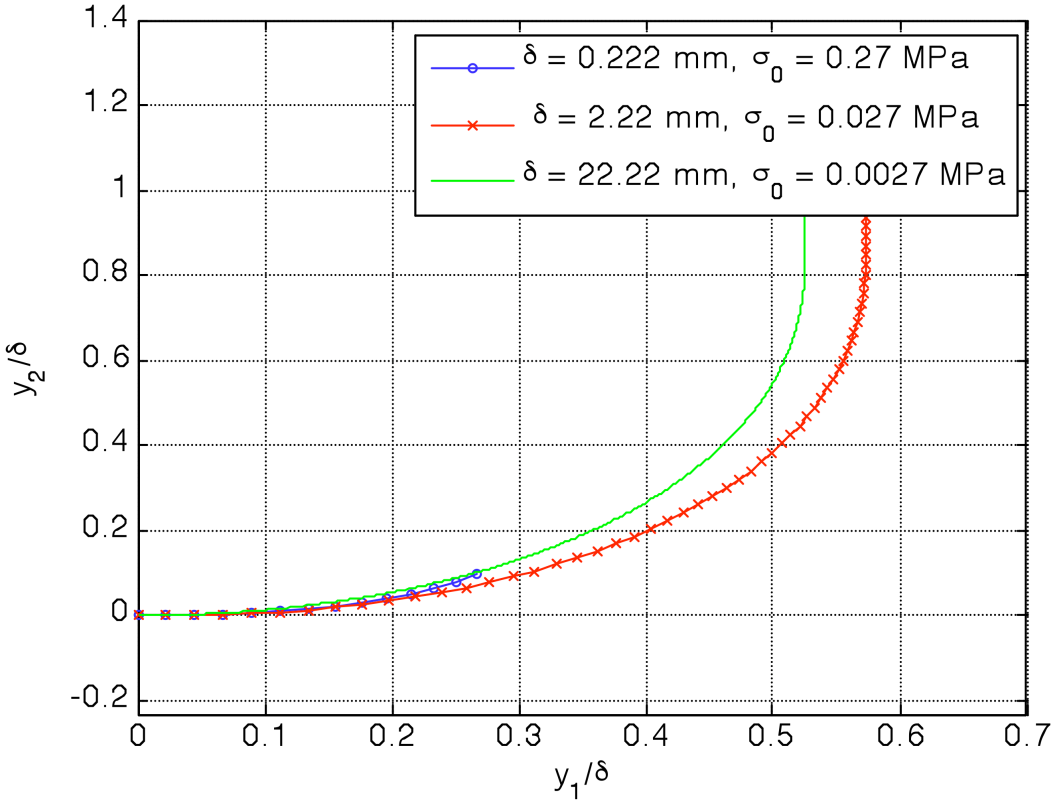

Figure 3.6: Process zone shape $y_2(y_1)$ for three different bending stiffnesses. The experimental profile is shown in blue.

In both cases where the bending stiffness has been decreased, the angle of the backing at the edge of the process zone is 90°. Thus, in these two cases, there is minimal to no bending present as evidenced by the fact that the local angle at the edge of the process zone is equal to the far-field peel angle. However, this is not the case for the experimental curve shown in blue in Figure 3.6. At the edge of the process zone, as mentioned previously, the local angle is not the same as the far-field peel angle. This suggests the

presence of bending in the tape backing, which must be accounted for in developing the theoretical framework for modeling this peeling configuration.

3.5 Local Process Zone Model

The results from the finite element simulations in the previous section are now used to motivate a closed-form theoretical framework for analyzing the peeling configuration. This analysis is used to determine the full-field force distribution in the process zone as well as a cohesive zone law to describe the process zone. Consider the peeling of an elastic adhesive film from a rigid substrate, as shown in Figure 3.7. The film has an elastic modulus E with a cross-sectional area of width b and thickness h. The adhesive backing is treated as a 2D planar beam, while the deforming adhesive in the process zone itself is considered as a cohesive zone (the cohesive zone description will be given in the next section). As the adhesive backing is peeled from the surface at a fixed angle, θ_0, it is similar to a bimaterial interfacial fracture problem. As the crack propagates, a process zone length, L, and height, δ, are defined.

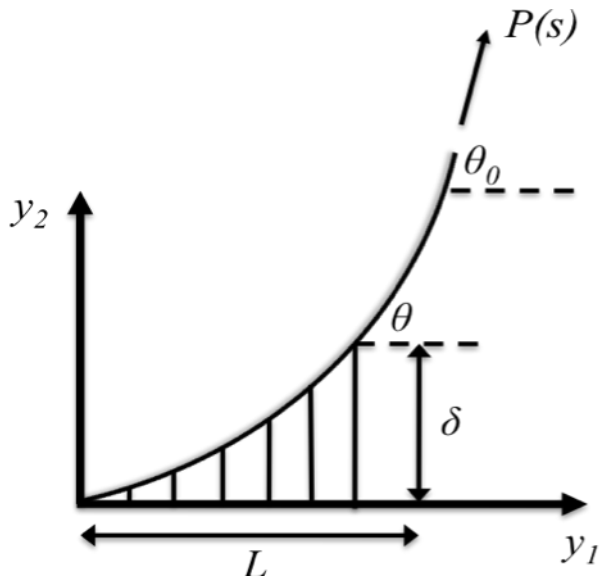

Figure 3.7: Schematic of a peeling configuration for an elastic adhesive film from a rigid substrate.

A base curve *s* is defined along the backing of the adhesive, with y_1 and y_2 being the coordinate frame in the deformed configuration. *P(s)* is the axial force in the beam. Far from the process zone, the axial force *P(s)* is the measured peel force P_f. Force equilibrium between two points, s_1 and s_2, along *s* requires

$$\vec{F}(s_2) - \vec{F}(s_1) + \int_{s_1}^{s_2} f(s)ds = 0 \tag{3.3}$$

or

$$\frac{d\vec{F}}{ds} + \vec{f} = 0 \tag{3.4}$$

where $\vec{F}$ is the internal force in the beam and $\vec{f}$ is the applied external force [49]. In component form, we can write Eq. 3.4 in terms of forces and moments

$$\frac{dN(s)}{ds} + kT(s) + \vec{f} \cdot \vec{n} = 0 \tag{3.5}$$

$$\frac{dT(s)}{ds} - kN(s) + \vec{f} \cdot \vec{t} = 0 \tag{3.6}$$

$$\frac{dM(s)}{ds} + \lambda N(s) + \vec{m} = 0 \tag{3.7}$$

where *T(s)* and *N(s)* are the internal axial and transverse forces along *s*, respectively, $\vec{t}$ and $\vec{n}$ unit vectors in the tangential and transverse directions, respectively, and λ a material constant related to the extensibility of the beam. A schematic of these forces is shown below in Figure 3.8, where the parameter σ is the cohesive zone force.

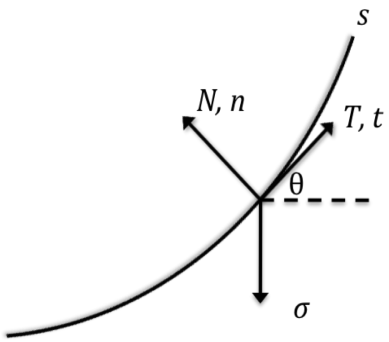

Figure 3.8: Force distribution at a point along the adhesive backing.

The parameter *k* is related to the curvature of the beam by

$$k = \frac{d\theta}{ds} \tag{3.8}$$

where θ is the local angle at a given position along s. The local angle θ is related to the slope curve s at any point by

$$\tan\theta = \frac{dy_2}{dy_1}. \tag{3.9}$$

The quantity dy_2/dy_1 can be determined by fitting a function to the shape of the tape backing from the experimental results in Chapter 2. To fit the experimental profile shown in Figure 2.7, an elliptical function is used. The general equation of an ellipse is given by

$$\frac{(y_1 - y_{10})^2}{A^2} + \frac{(y_2 - y_{20})^2}{B^2} = 1 \tag{3.10}$$

for an ellipse centered at (y_{10}, y_{20}). The constants A and B are fit empirically. Rewriting Eq. 3.10 in terms of y_2 results in

$$y_2 = B\sqrt{1 - \frac{(y_1 - y_{10})^2}{A^2}} + y_{20}. \tag{3.11}$$

Using this form, the profile of the tape backing is fit as a quarter of a full ellipse. To center this ellipse, one can see that the origin of process zone lies along the fourth quadrant of the ellipse. For a process zone of length, L and height, δ in the deformed configuration, the elliptical fit is centered at $(y_{10}, y_{20}) = (0, \delta)$. Thus, the form of the ellipse used analytically to fit the experimental profile is

$$y_2(y_1) = \frac{B}{A}\sqrt{A^2 - y_1^2} + \delta \tag{3.12}$$

where the constants A and B are determined experimentally. An image of the process zone for a 90° peel test from Figure 2.7 is shown in Figure 3.9 with the elliptical profile fit imposed.

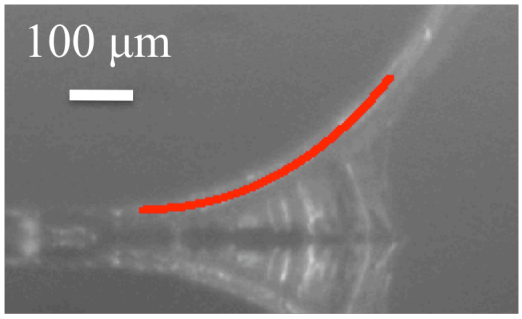

Figure 3.9: Image of the process zone for a 90° peel test with the elliptical profile (Eq. 3.12) fit to the tape backing, shown in red.

There are several functional forms for fitting the experimental profile that may yield similar results to the ones shown in this chapter (for example, a second-order polynomial fit $y_2(y_1) = Ay_1^2 + By_1$ also fits the experimental profile reasonably well). To ultimately determine the best function, the choice of curve fit should be motivated by some physical argument rather than arbitrarily fitting the best curve to the profile. As will be seen in the remainder of this section, the profile shape function will be differentiated four times for input into this theoretical framework. While the function itself seems like an accurate fit, a higher-order derivative may not necessarily be accurate.

The derivative of Eq. 3.12 can be related to the local angle θ at any point along the curve, s, by

$$\frac{dy_2}{dy_1} = \tan\theta = -\frac{By_1}{A}\left(A^2 - y_1^2\right)^{1/2}. \tag{3.13}$$

Expressing the local angle θ as a function of the beam shape, one has

$$\theta = \tan^{-1}\left(-\frac{By_1}{A}\left(A^2 - y_1^2\right)^{1/2}\right). \tag{3.14}$$

For an inextensible beam, the parameter $\lambda = 1$ and for an increment ds along the base curve,

$$dy_1^2 + dy_2^2 = ds^2. \tag{3.15}$$

Dividing this expression by dy_1^2, we can utilize the experimental fit to obtain a relation for the change in y_1 with respect to the base curve s,

$$\left(\frac{ds}{dy_1}\right)^2 = 1 + \left(\frac{dy_2}{dy_1}\right)^2 \tag{3.16}$$

$$\frac{dy_1}{ds} = \left(1 + \frac{B^2 y_1^2}{A^2\left(A^2 - y_1^2\right)}\right)^{-1/2}. \tag{3.17}$$

From this expression, k can be determined as a function of y_1, which will be a useful relation when solving the equilibrium relations Eqs. 3.5-3.7,

$$\frac{d\theta}{ds} = \frac{d\theta}{dy_1}\frac{dy_1}{ds} \tag{3.18}$$

where

$$\frac{d\theta}{dy_1} = \frac{-\dfrac{By_1^2}{A\left(A^2 - y_1^2\right)^{3/2}} + \dfrac{B}{A\left(A^2 - y_1^2\right)^{1/2}}}{1 + \dfrac{B^2 y_1^2}{A^2\left(A^2 - y_1^2\right)}} \tag{3.19}$$

and thus

$$\frac{d\theta}{ds} = \frac{-\dfrac{By_1^2}{A\left(A^2 - y_1^2\right)^{3/2}} + \dfrac{B}{A\left(A^2 - y_1^2\right)^{1/2}}}{\left(1 + \dfrac{B^2 y_1^2}{A^2\left(A^2 - y_1^2\right)}\right)^{3/2}}. \tag{3.20}$$

As there are no external moments applied, $\vec{m} = 0$ and Eq. 3.7 becomes

$$\frac{dM}{ds} + N = 0. \tag{3.21}$$

The internal moment can be related to the curvature by

$$M = EIk = EI\frac{d\theta}{ds} \tag{3.22}$$

and Eq. 3.21 can be written in terms of N as

$$N = -\frac{d}{ds}\left(EI\frac{d\theta}{ds}\right). \tag{3.23}$$

Solving for N as a function of y_1 yields

$$N = -EI\frac{(C_1 + C_2)}{C_3} \tag{3.24}$$

where

$$C_1 = \frac{-\dfrac{3By_1^3}{A\left(A^2 - y_1^2\right)^{5/2}} + \dfrac{3By_1}{A\left(A^2 - y_1^2\right)^{3/2}}}{\left(1 + \dfrac{B^2 y_1^2}{A^2\left(A^2 - y_1^2\right)}\right)^{3/2}}, \tag{3.25}$$

$$C_2 = \frac{\dfrac{3}{2}\left(\dfrac{By_1^2}{A\left(A^2 - y_1^2\right)^{3/2}} + \dfrac{B}{A\left(A^2 - y_1^2\right)^{1/2}}\right)\left(\dfrac{2B^2 y_1^3}{A^2\left(A^2 - y_1^2\right)^2} + \dfrac{2B^2 y_1}{A^2\left(A^2 - y_1^2\right)}\right)}{\left(1 + \dfrac{B^2 y_1^2}{A^2\left(A^2 - y_1^2\right)^{5/2}}\right)}, \tag{3.26}$$

and

$$C_3 = \left(1 + \frac{B^2 y_1^2}{A^2\left(A^2 - y_1^2\right)}\right)^{1/2}. \tag{3.27}$$

3.6 Cohesive Zone Definition

Consider the force distribution as shown in the previous section in Figure 3.8. A distributed cohesive zone force σ_0 is defined acting vertically downward with respect to the deformed configuration. This requires making the assumption that the deformation of the fibrils in the process zone is normal to the substrate, with no sliding displacement. Therefore, the cohesive force, σ_0 can be written as

$$\vec{f} = \sigma_0 \begin{bmatrix} 0 \\ -1 \end{bmatrix}. \tag{3.28}$$

The tangent and normal unit vectors ***t*** and ***n*** can be expressed as a function of the angle, θ by

$$\vec{t} = \begin{bmatrix} \cos\theta \\ \sin\theta \end{bmatrix} \tag{3.29}$$

$$\vec{n} = \begin{bmatrix} -\sin\theta \\ \cos\theta \end{bmatrix} \tag{3.30}$$

and thus the external force $\vec{f}$ is resolved in the tangential and normal directions as

$$\vec{f} \cdot \vec{n} = -\sigma_0 \cos\theta \tag{3.31}$$

$$\vec{f} \cdot \vec{t} = -\sigma_0 \sin\theta. \tag{3.32}$$

Returning to the equilibrium equation in component form, using Eqs. 3.5 and 3.6 to insert the cohesive zone law behavior, having solved for the transverse force N in the previous section,

$$\frac{dN}{ds} + \frac{d\theta}{ds} T - \sigma_0 \cos\theta = 0 \tag{3.33}$$

$$\frac{dT}{ds} - \frac{d\theta}{ds} N - \sigma_0 \sin\theta = 0 \tag{3.34}$$

This yields two equations with two unknowns, T and σ_0. Both expressions are solved for σ_0 and set equal to eliminate a variable

$$\frac{1}{\cos\theta}\frac{dN}{ds}+\frac{T}{\cos\theta}\frac{d\theta}{ds}=\frac{1}{\sin\theta}\frac{dT}{ds}-\frac{N}{\sin\theta}\frac{d\theta}{ds}. \tag{3.35}$$

This expression is a first-order, non-linear ordinary differential equation in s. To solve for T, the dT/ds term is cleared, resulting in

$$\frac{dT}{ds}-N\frac{d\theta}{ds}=\tan\theta\frac{dN}{ds}+T\tan\theta\frac{d\theta}{ds}. \tag{3.36}$$

It is more useful to express T as a function of y_1 in the deformed configuration, rather than s in the undeformed configuration. Thus, Eq. 3.33 is rewritten as

$$\frac{dT}{dy_1}\frac{dy_1}{ds}=\frac{d\theta}{dy_1}\frac{dy_1}{ds}N+\frac{dN}{dy_1}\frac{dy_1}{ds}\tan\theta+\frac{d\theta}{dy_1}\frac{dy_1}{ds}T\tan\theta \tag{3.37}$$

and thus dy_1/ds is eliminated since it appears in every term

$$\frac{dT}{dy_1}=\left(\frac{d\theta}{dy_1}\tan\theta\right)T+\frac{d\theta}{dy_1}N+\frac{dN}{dy_1}\tan\theta. \tag{3.38}$$

To solve this equation, a boundary condition must be imposed at either end of the process zone $0 \le y_1 \le L$. By making use of the far-field steady-state peel force P_f obtained experimentally, a force balance is considered for the beam outside of the process zone where the cohesive force $\sigma = 0$. This force balance is shown in Figure 3.10.

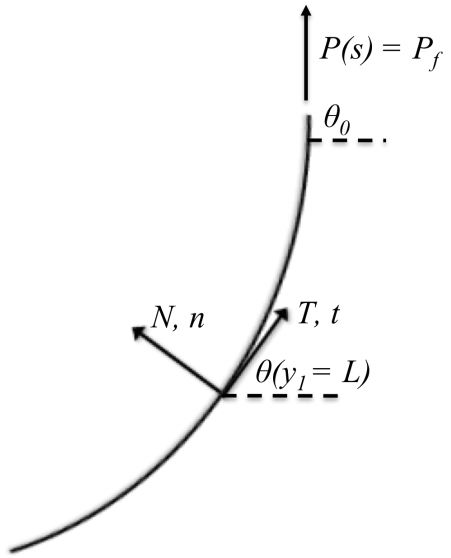

Figure 3.10: Force balance outside the process zone for determining the applicable boundary condition at $y_1 = L$.

$$\vec{F} = \begin{Bmatrix} T(s) \\ N(s) \end{Bmatrix} = P_f \begin{Bmatrix} \cos\left(\theta_0 - \theta(y_1 = L)\right) \\ \sin\left(\theta_0 - \theta(y_1 = L)\right) \end{Bmatrix} \tag{3.39}$$

where θ_0 is the angle at which the far-field peel force P_f is measured and θ is the local angle at some point along the beam (this definition for θ_0 and θ will be used for the rest of the chapter). To obtain the boundary condition, Eq. 3.39 is evaluated at $y_1 = L$. Using this boundary condition, Eq. 3.38 is solved numerically using Matlab.

Substituting T and N into either Eq. 3.33 or Eq. 3.34, one can solve for the cohesive zone stress σ_0. Solving for σ_0, the cohesive zone stress σ_0 is obtained as a function of y_1:

$$\sigma_0 = \frac{1}{\cos\theta} \frac{dy_1}{ds} \left(\frac{dN}{dy_1} + \frac{d\theta}{dy_1} T \right) \tag{3.40}$$

The distributions of $\sigma_0(y_1)$ and $y_2(y_1)$ are then combined to yield the cohesive zone law $\sigma_0(y_2)$.

3.7 Local Process Zone Force Distribution and Cohesive Zone Results

Using the model derived in the previous section in the context of finite deformation beam theory, the experimental results from Chapter 2 are used to extract the cohesive zone law in Eq. 3.40. The experimental profiles from peel tests through a range of peel angles of 30˚ to 90˚ are fit using the elliptical form shown in Eq. 3.12 This allows for the determination of the empirical constants A and B. Figures 3.11 and 3.12 show the relationship between the constants A and B, respectively, and the peel angle, θ.

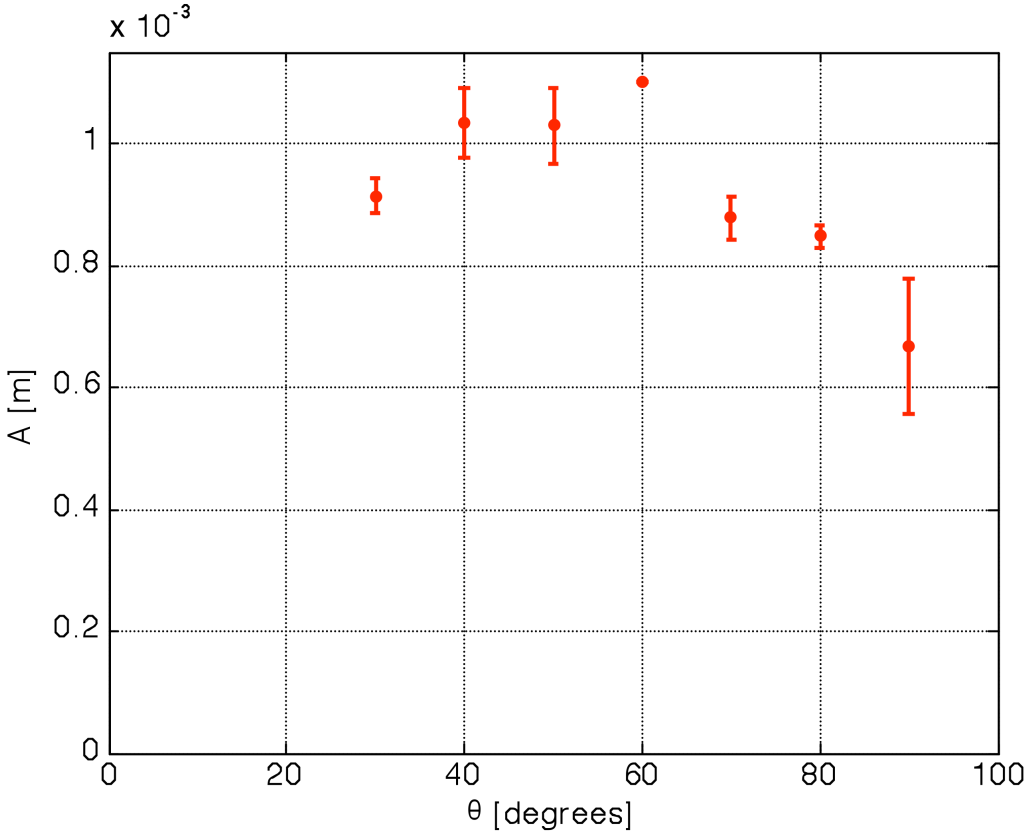

Figure 3.11: Empirical constant A as a function of peel angle, θ.

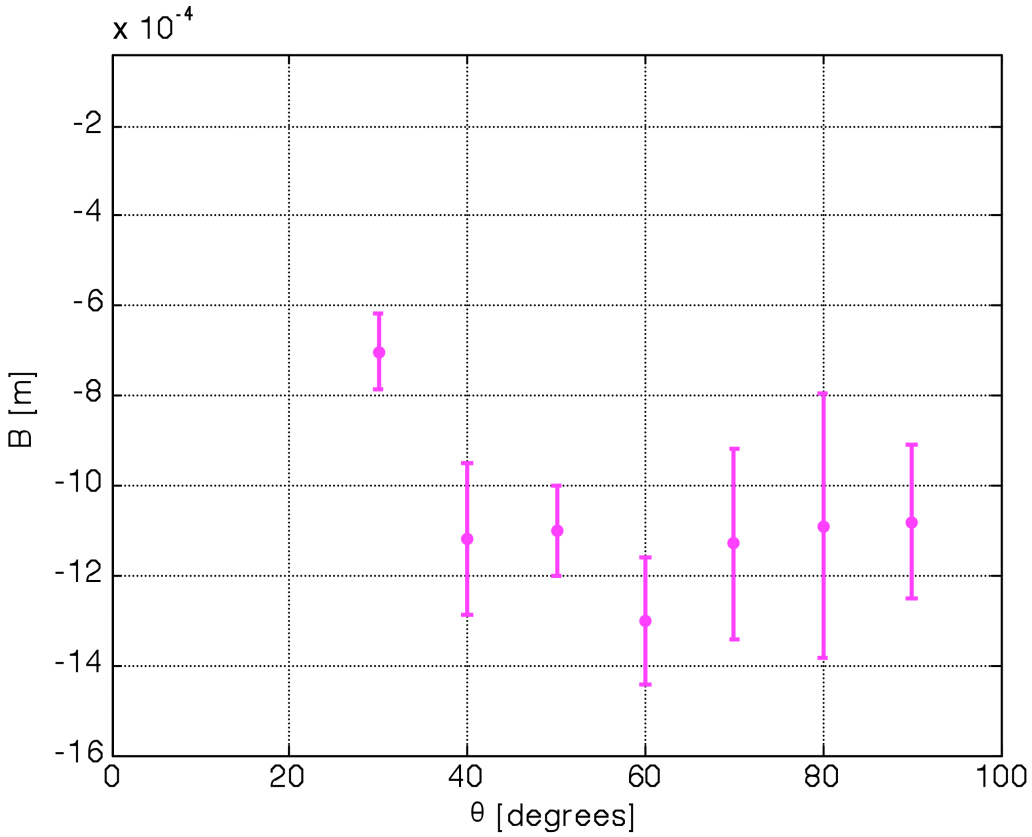

Figure 3.12: Empirical constant B as a function of peel angle θ.

From the Figures 3.11 and 3.12, the constant A increases as the peel angle decreases, while B appears to remain nearly constant with exception of the increase at $\theta = 30°$. The constant A is an order of magnitude larger than B. In the process of fitting the curves, it is seen that the value for A can generally be related to the length of the process zone, L, by

$$A = 1.65L \tag{3.41}$$

Table 3.2 summarizes the results for the empirical fitting constants A and B, along with the values for the process zone length and height, L and δ.

L [μm]	δ [μm]	A [μm]	B [μm]
412 ± 78	226 ± 21	(679 ± 1.28) x 10^{-4}	(-12 ± 0.89) x 10^{-4}

Table 3.2: Process zone geometry and fitting coefficients for peel angle of $\theta_0 = 90°$.

Using the experimental parameters obtained for L, δ, A, B, and the steady-state peel force P_f, the data is input into the model from Section 3.6 in order to extract a relation between the cohesive zone stress σ_0 and the height of the process zone δ. Additionally, the internal transverse and axial forces in the tape backing, N and T, respectively, can be determined and compared to the finite element simulations. Figure 3.13 shows the transverse force, N plotted as a function of y_2 for a peel angle of 90°, where the maximum value of y_2 is the height of the process zone δ measured experimentally.

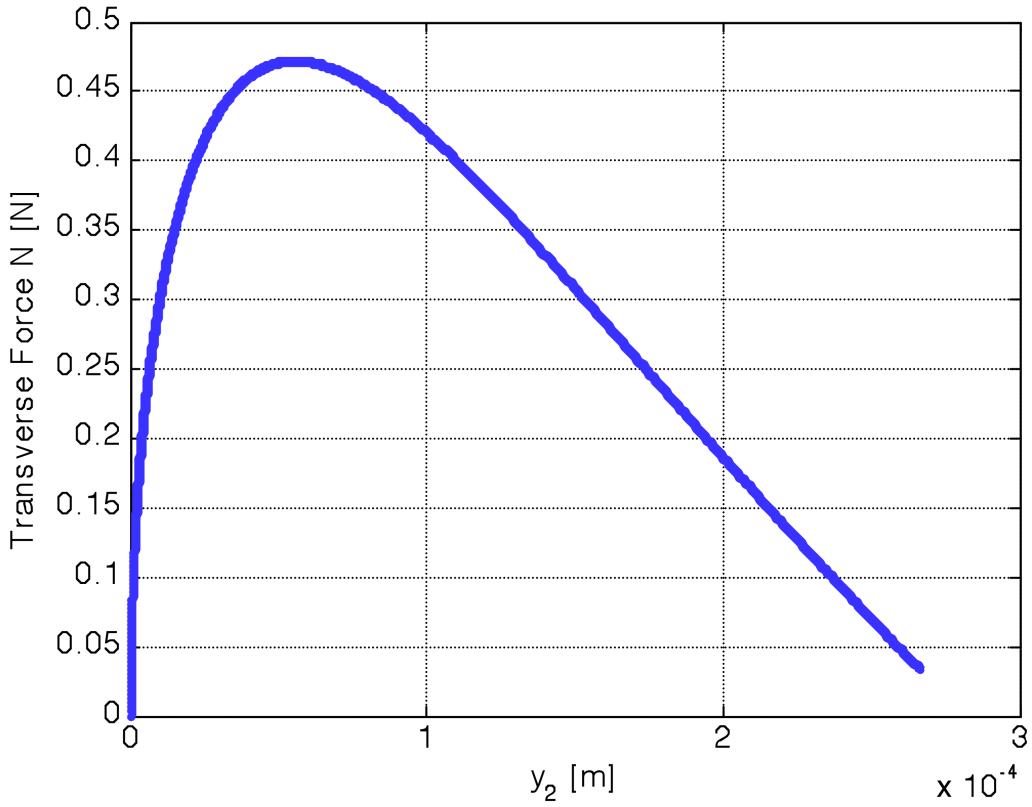

Figure 3.13: Transverse (normal) force in the tape backing, N, as a function of the opening displacement, y_2 in the cohesive zone for a peel angle of 90°.

At the end of the cohesive zone ($y_2 = \delta$), the transverse force N approaches zero but does not reach it. This correlates with the results of the finite element simulations (Figure 3.6), as in the case where there is still curvature in the backing as a result of a bending moment, the transverse force will be non-zero.

The axial force T is plotted as a function of the length of the process zone, y_1 in Figure 3.14.

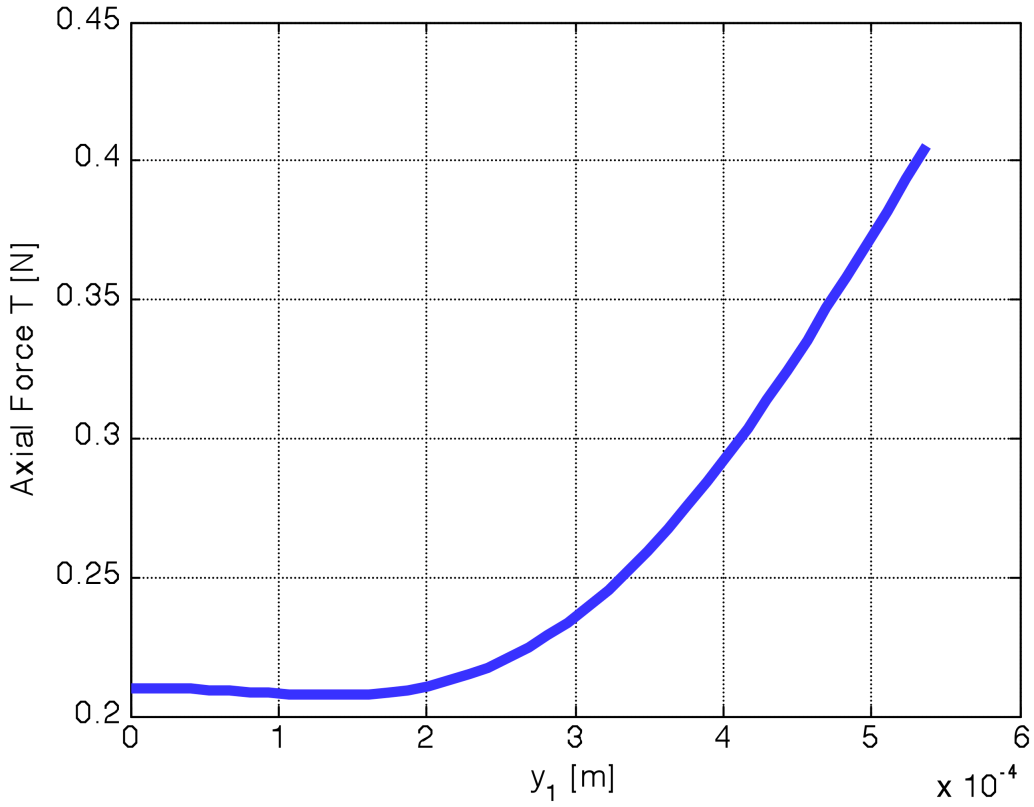

Figure 3.14: Axial force in the tape backing, T as a function of the process zone length, y_1 in the cohesive zone for a peel angle of 90˚.

The axial force is non-zero at the origin of the process zone, which is not in agreement with the finite element simulations. This can be attributed to the boundary condition prescribed by Eq. 3.39, and is discussed later in this section.

Figure 3.15 is a plot of the cohesive zone law, or the σ_0 - δ relationship, which can now be determined since the force distribution is known.

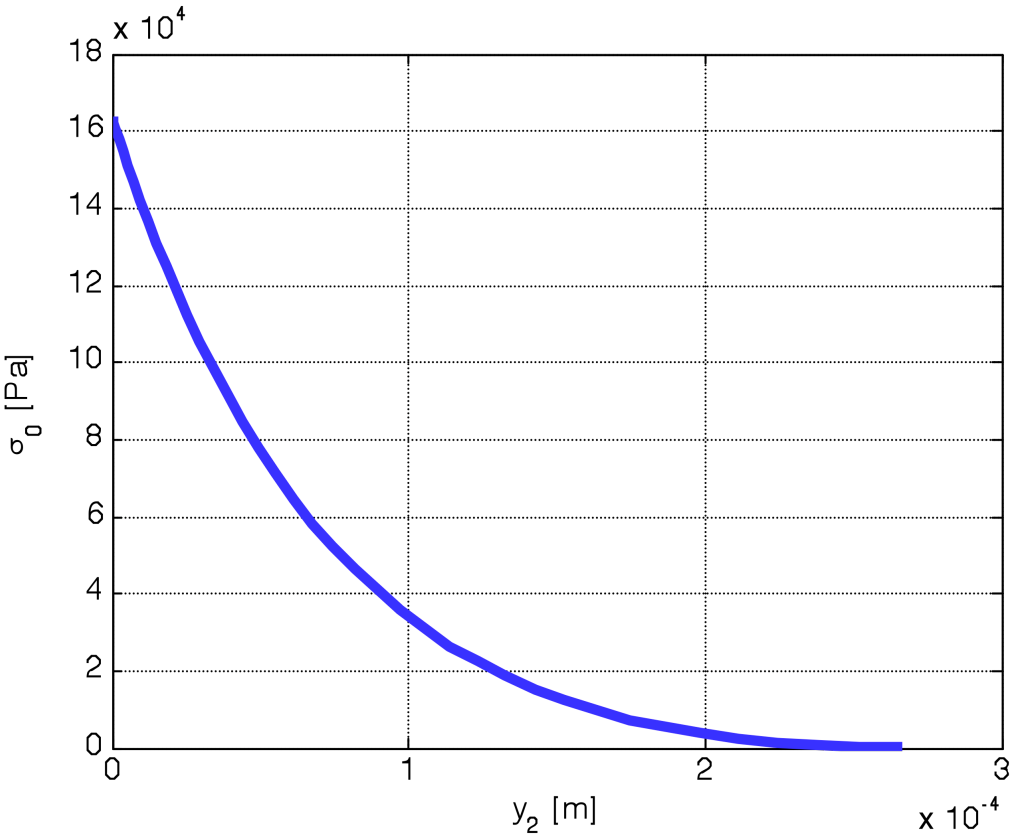

Figure 3.15: Cohesive zone stress-displacement relation for a 90° peel test.

The cohesive zone force σ_0 goes to zero at the end of the process zone, where $y_2 = \delta$. The general shape of this curve is very similar to the power-law form given in Eq 1.9 with $n = 2$. The transverse and axial forces N and T, respectively, along with the cohesive zone relation σ_0 - δ are determined for the range of peel angles 30° to 90°. For comparison with the 90° tests, Figures 3.16 to 3.18 show plots of the axial and transverse forces, T and N, respectively, along with the cohesive zone law curve for a peel angle of 70°.

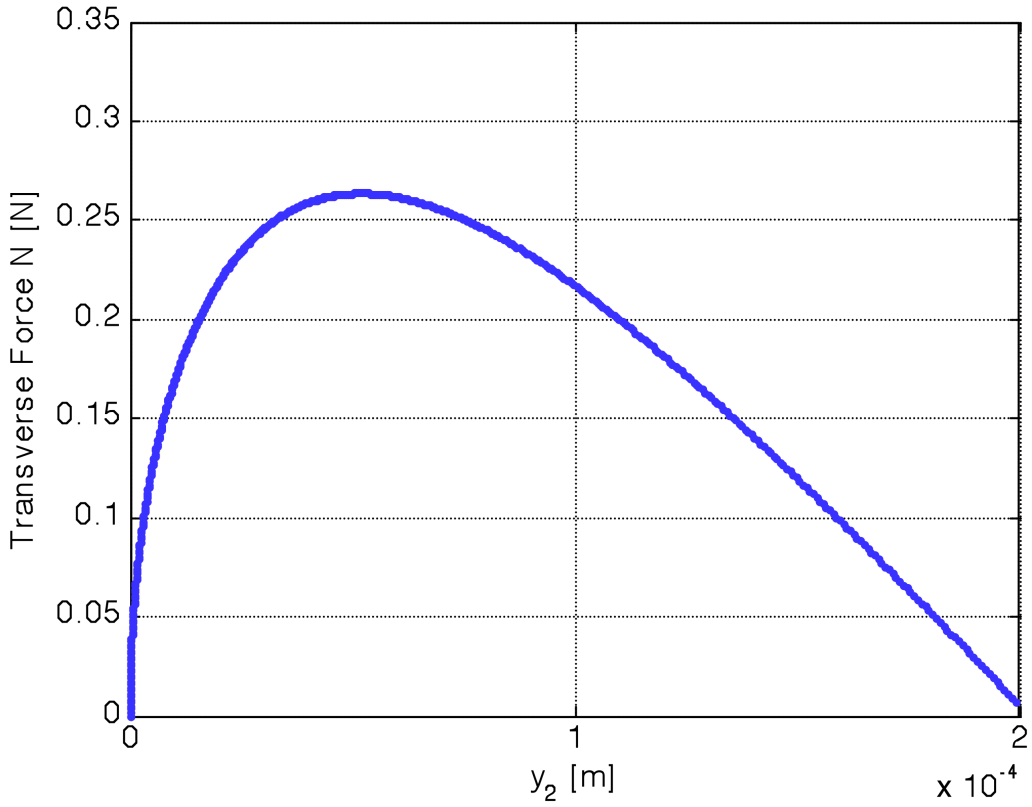

Figure 3.16: Transverse (normal) force in the tape backing, N, as a function of the opening displacement, y_2 in the cohesive zone for a peel angle of 70°.

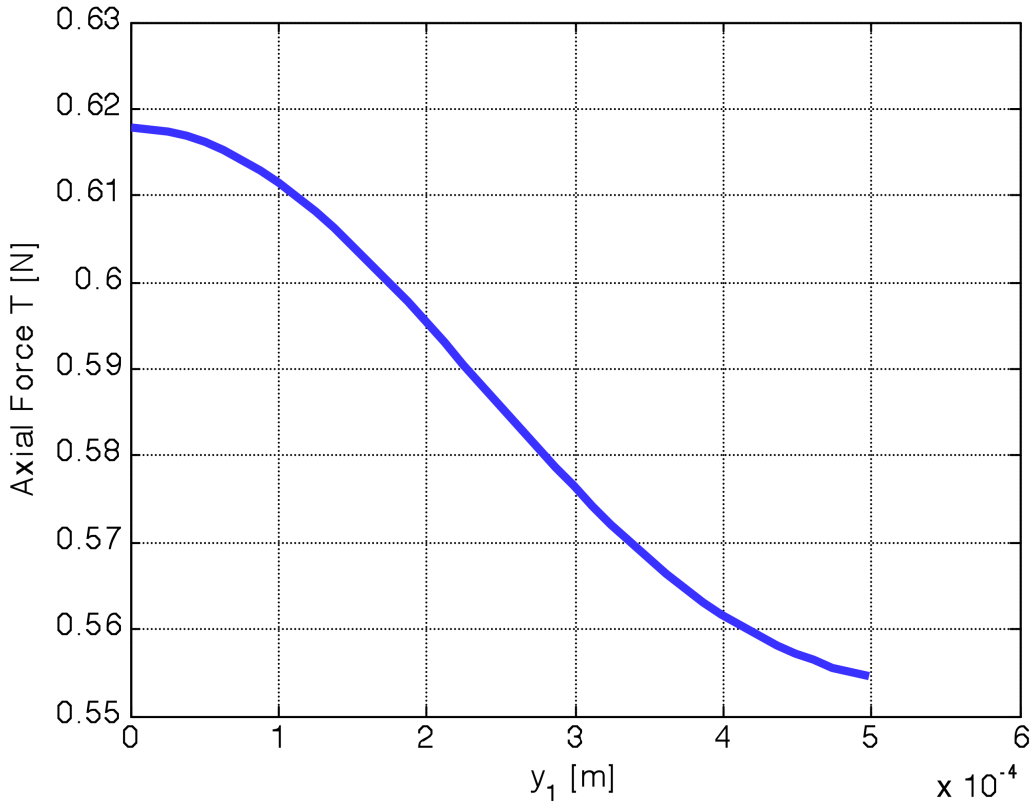

Figure 3.17: Axial force in the tape backing, T as a function of the process zone length, y_1 in the cohesive zone for a peel angle of 70˚.

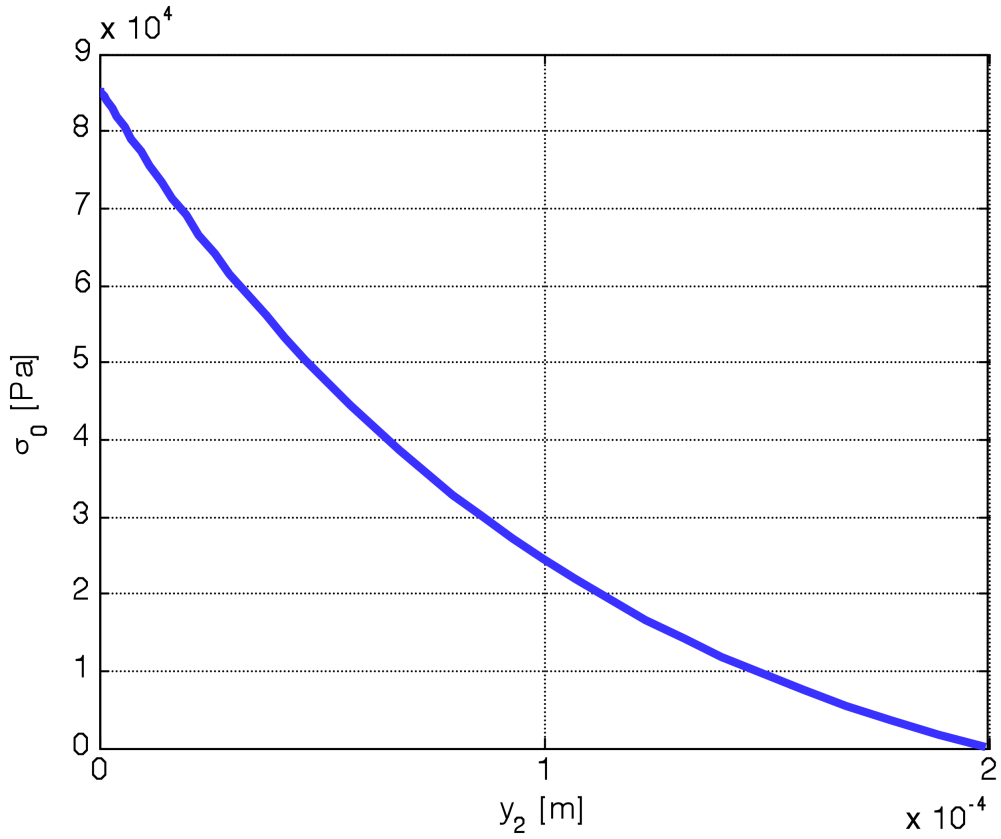

Figure 3.18: Cohesive zone stress-displacement relation for a 70° peel test.

Comparing the transverse and axial forces between the 90° and the 70° peel test, the shape of the transverse force, *N*, for both angles is similar, with the 90° peel test having a larger peak transverse force. The axial force, *T*, at the end of the process zone ($y_1 = L$) for the 70° peel test is larger than that of the 90° peel test, consistent with finite element simulations. However, at the origin of the process zone ($y_1 = 0$) for the two angles, the axial force, *T*, is not consistent. The shapes of the axial force curves for both angles (Figs. 3.14 and 3.17) are also not the same. Since the boundary condition for the axial force is applied at the end of the process zone ($y_1 = L$), this may explain why the values of *T* are not consistent with the finite element simulations at the origin of the process zone ($y_1 = 0$) despite their agreement at the end of the process zone. Comparing Figures 3.15 and

3.18, the cohesive stress-displacement relations for the two angles have similar shapes, with the peak stress, σ_0, being lower for the 70° tests.

To determine the adhesion energy G of this cohesive zone, the σ-δ curve can be integrated as previously described in Chapter 1

$$G = \int_0^{\delta} \sigma(y_2) dy_2 . \tag{3.42}$$

The adhesion energy can also be determined using the global energy balance approach of Rivlin previously described (Eq. 1.7). Comparing the values of G obtained through these two different methods, the validity of the local method using finite deformation beam theory is analyzed. Figure 3.19 shows the adhesion energy G obtained by both the Rivlin model and the model presented here as a function of the peel angle, θ.

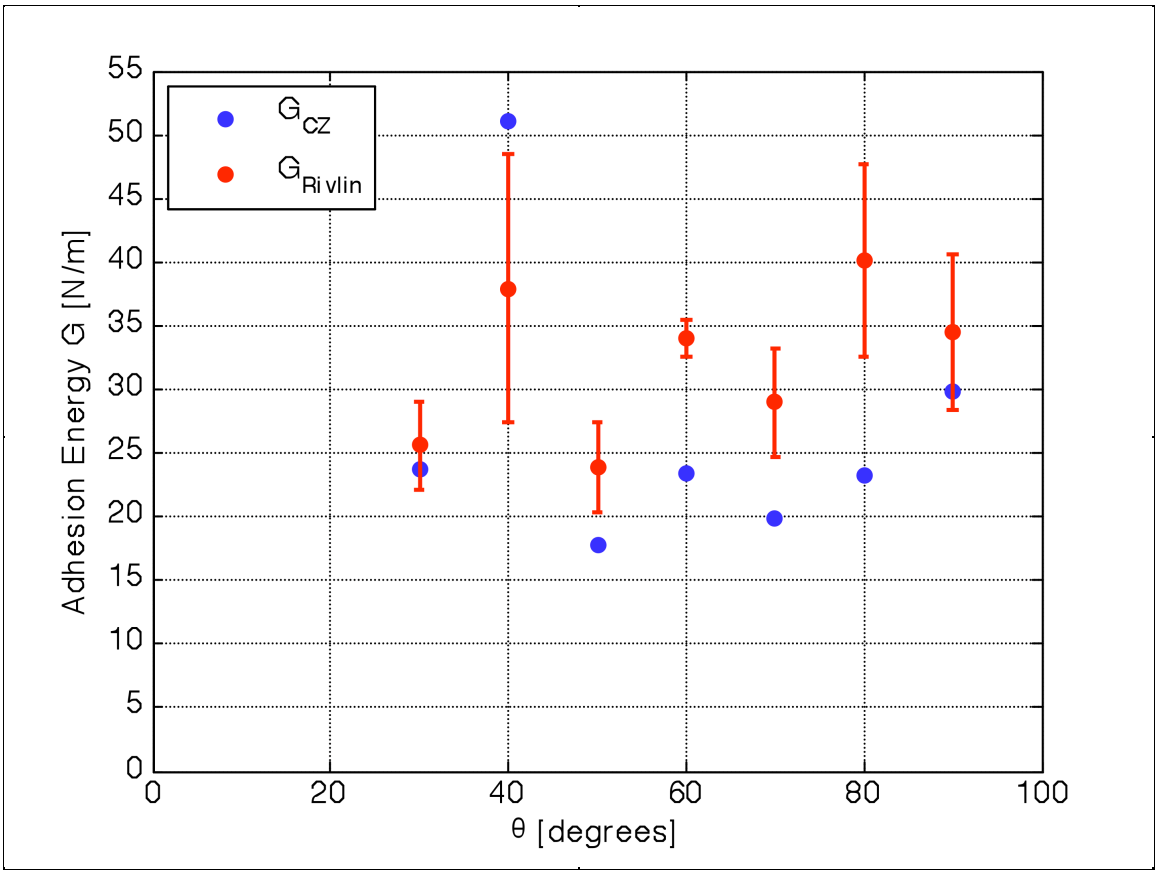

Figure 3.19: Adhesion energy G for range of angles. G_{CZ} is obtained through the local process zone model, while G_{Rivlin} is obtained through the global energy balance.

For a peel angle of 40°, there is a large difference both in the experimental results as well as the correlation between the two methods of determining G. This angle is the only case in which the cohesive zone model yields a higher value of adhesion energy than the Rivlin model. For all other angles shown in Figure 3.19, the cohesive zone model predicts a lower value of the adhesion energy, G. The difference between the two methods is that the Rivlin model determines the global adhesion energy through the far-field peel force P_f and peel angle θ_0. The new method presented here determines slightly smaller values of adhesion energy through the far-field peel force, P_f, and the size of the local process zone. The model here also provides the local force distribution in the

process zone, which the Rivlin model does not provide. As is seen from the finite element simulations, the peel force in the process zone is not constant (Figure 3.5). The present analytical model is able to quantify the forces in this region given that the size of the process zone can be quantified experimentally.

While the advantage of the model presented here is the ability to describe the behavior in the process zone, the implementation of this model is more complicated than the Rivlin model. The simplicity of the Rivlin model is that the adhesion energy can be determined as a function of two far-field variables (P_f and θ_0) that can easily be measured. The cohesive zone model here is sensitive to the values of the empirical constants A and B in the curve fit. As previously mentioned, there are any number of functions that could be used to fit the experimental profile. It is also important to note that in the cohesive zone extraction, an experimentally-obtained data curve is being differentiated four times as it is implemented into the theoretical framework. While the curve fit itself is a functional form, new error may be introduced as the curve fit is processed several times. As previously mentioned, a different boundary condition could be used in order to produce a force distribution that is in better agreement with finite element simulations. This may also improve the correlation between the adhesion energies.

It is also observed that the adhesion energy, G, appears to be constant within some quantifiable error, independent of the peel angle, θ_0, which is in agreement with previous studies [49]. In the context of the cohesive zone law extraction method used here, since the adhesion energy is not a function of the peel angle θ_0, determining the cohesive zone law for a 90˚ peel test may be sufficient to describe the cohesive zone law for an entire

range of angles. The relation between the adhesion energy, G, and the peel angle, θ_0, will be investigated in more detail in Chapter 4.

The definition of the moment M in Eq. 3.7 includes no shear forces. Consider the case where shear forces are included in the definition of the moment as is the case in the Timoshenko beam theory [50]. In the current framework, it is assumed that plane sections remain plane (Bernoulli-Euler beam theory). However, when shear is included, it can no longer be assumed that plane sections remain plane. The shear force component is normally incorporated for short beams, where the ratio of thickness h to length L is $h/L \sim 10$. A form factor κ is introduced, which is nominally 5/6 for rectangular cross section. The theory considered in the previous section, which does not include shear forces, is a sufficient approximation when the following condition is met:

$$\frac{EI}{\kappa LA\mu} << 1 \tag{3.43}$$

where μ is the shear modulus of the beam. For the material used here (Scotch MagicTape), $\nu = 0.2$, $I = \frac{bh^3}{12}$, b = 19mm (3/4"), h = 50 μm, and $\kappa = 5/6$. Thus, $\frac{EI}{\kappa LA\mu}$ = 1.1385 x 10^{-6}, meeting the condition in Eq. 3.43. Hence, the exclusion of shear forces in the analysis is justified.

3.8 Conclusions

A theoretical framework has been developed to model the peeling configuration appropriately and extract a cohesive zone law from the data of an experimental peel test. The model is motivated using a finite element simulation to model the peeling

configuration and investigate the mechanics phenomena in the tape backing. Under the context of finite deformation beam theory, this model enables the determination of the full-field force distribution in the process zone, as well as the cohesive zone law for a range of peel angles. The adhesion energy is calculated from the cohesive zone law and compared to the Rivlin model, showing good agreement. Thus, the inverse method of a local cohesive zone extraction of the process zone from an experimental peel test produces similar results as the global energy balance method of Rivlin, and is a viable method for determining the adhesion energy of the system. The methodology also provides insights regarding the force distribution in the process zone.

Chapter 4

Rate Dependence in the Peel Test

4.1 Introduction

This chapter explores rate-dependent effects and phenomena during the peel test. Thus far, this thesis has considered the steady-state effects of peel at a constant single peel velocity, v_0 = 10 μm/s. In this section, the effects of varying the peel velocity will be examined to develop relations between the adhesion energy, the peel angle, and the rate of peel.

4.2 Experimental Method

The candidate material used here is Scotch Industrial Packing Tape (3M, Minneapolis, MN). This specific adhesive tape is used because of its large width (b = 48 mm), which will be utilized in parts of the study to conduct stability experiments where the width changes as a function of position. Tests are conducted using the same peel configuration as described in Chapter 2, configured slightly differently, as shown in Figure 4.1.

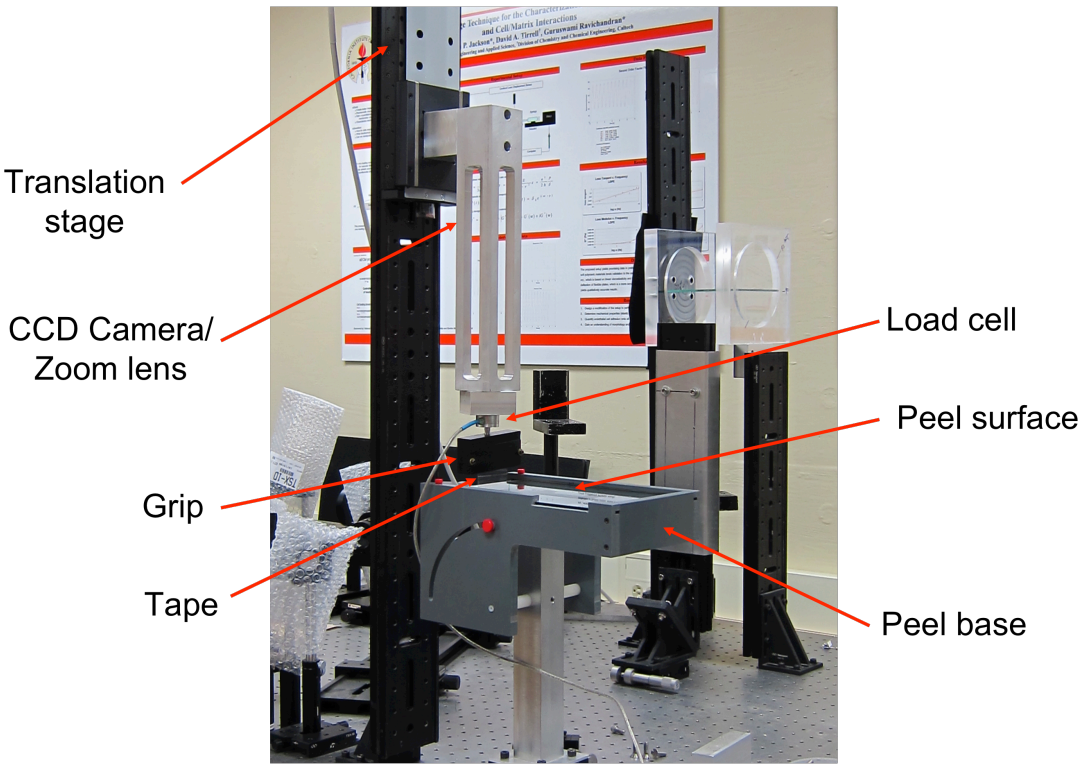

Figure 4.1: Modified peel test configuration for studying rate dependence.

The peel base is turned around opposite of the prior experiments described in Chapter 2. A wider grip is used to accommodate the increased width in tape as compared to the Scotch MagicTape used prior, and the initial peel arm, defined as L_0, is set to be very small, as shown in the figure. As the translation stage is moved vertically, the angle will change rapidly. This allows for a rapid change of the peel angle, as opposed to the previous tests where the angle was kept constant for a given test. However, the tradeoff is that a steady-state peel force is not reached. The grips are made from delrin, a commercial plastic. The tape is peeled from a rigid glass plate with dimensions 203 x 127 x 3.175mm (8" x 5" x 1/8") for the length, width, and thickness, respectively.

Three separate types of measurements will be discussed in this chapter. The first set examines the dependence of peel force and adhesion energy on the peel velocity through

a range of angles. Using the setup in Figure 4.1, tests are conducted for varying initial peel velocities with a short initial peel arm length of L_0 = 12.7 mm (0.5”). While a steady-state peel force is never reached, it is interesting to see how the peel force and adhesion energy change with angle as the angle is reduced from 90° towards 0°.

Further experiments are then performed using a longer peel arm similar to the original configuration in Chapter 2. The goal of these tests is to measure the steady-state peel force (P_f) for a range of angles and compare to the similar curve in Chapter 2 for the Scotch MagicTape material. The adhesion energy G is also plotted as a function of peel angle, to examine the question of whether or not the adhesion energy is a function of peel angle. Finally, a set of measurements is conducted to examine the relation between the steady-state peel force P_f and the peel velocity v for tests with a constant peel angle of 90°. The goal is to develop a rate-dependent law that relates the peel force (P_f) and the peel velocity (v).

4.3 Influence of Peel Arm Length on Local Change in Peel Angle

In Chapter 2, experiments were conducted while keeping the peel angle constant during a test in order to achieve a steady-state peel force at the given angle. This is done to compare the results to the predictions by Rivlin and Kendall models [18, 22]. One way in which this is accomplished is by having a long peel arm, as it is seen geometrically that this enables the peel angle to be kept constant without moving the base upon which the rigid substrate is held. However, the peel angle can be changed rapidly by making the peel arm very short. Consider the case of a 90° peel test shown in Figure 4.2. The extremity of the tape, denoted y_a, is subject to a fixed velocity v and pulled vertically in

order to initiate peel. The test begins in the initial, undeformed configuration Ω_0, with defined parameters including the initial peel arm length L_0, initial tip position a_0, and initial peel angle θ_0. The tape is peeled through some distance to the deformed configuration Ω_i (Figure 4.2), where the new tip position and peel angle are denoted by a_i and θ_i, respectively.

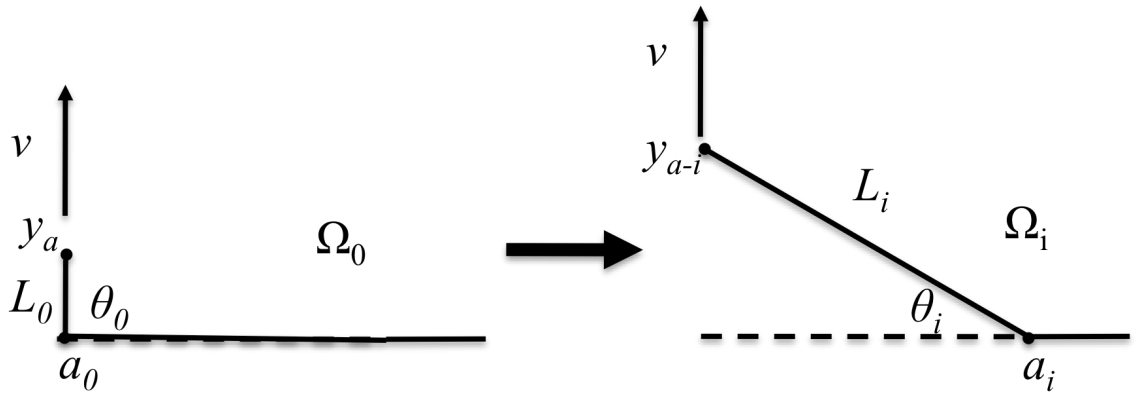

Figure 4.2: Schematic of a displacement-controlled peel test at velocity v.

The variables a_0 and a_i can be related by

$$a_i - a_0 = a, \tag{4.1}$$

where a is referred to as the instantaneous tip position with respect to the initial configuration. From geometry, the new peel angle θ_i (assuming inextensibility) is

$$\theta_i = \cos^{-1}\left(\frac{a}{a + L_0}\right). \tag{4.2}$$

The influence of the initial peel arm length on the local change in peel angle is seen in Figure 4.3 over a range of tip positions. As L_0 is increased, the angle change for a given

tip position decreases. As discussed briefly in Chapter 2, to keep the peel angle relatively constant during a peel test at an intended constant angle, L_0 is set to 76.2 mm (3”).

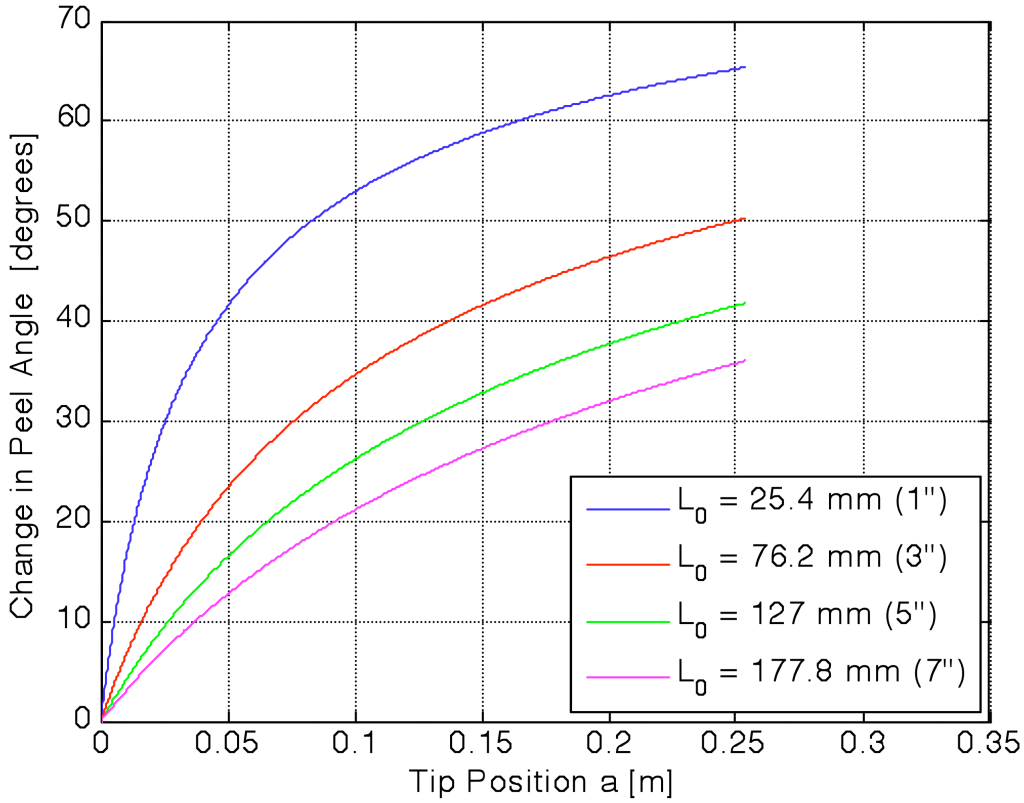

Figure 4.3: Change in peel angle, θ vs. tip position, a for varying initial peel arm length, L_0.

For a peel arm of L_0 = 25.4 mm (1”), the peel angle deviates from the initial peel angle by over 40 degrees for a change in tip position of 50 mm. As the peel arm is increased, the change in peel angle for a given tip position is reduced.

4.4 Relation between Applied Peel Rate and Tip Velocity

Consider the displacement controlled peel test described and shown schematically in Figure 4.2. An expression for the tip position a during a peel test as a function of the prescribed displacement of the tape at position y_a is derived below.

Assuming an inextensible tape, the following quantities are defined: L_0 as the initial peel band length (debonded portion), a_0 as the initial tip position, a_i as the instantaneous tip position, and L_i as the instantaneous length of the debonded portion of the peel band. The tip position is defined as the point of the first presence of a fibril in the process zone; relative to Chapter 2, it is the same as the origin of the process zone. The peel angle at a given time is denoted θ_i. These variables can be related by

$$L_i = L_0 + a, \tag{4.3}$$

where a is used to denote the quantity, a_i-a_0. The following geometrical relations are based upon Figure 4.2:

$$L_i \sin\theta_i = y_{a-i}; \tag{4.4}$$

$$L_i \cos\theta_i = a; \tag{4.5}$$

$$\sin^2\theta + \cos^2\theta = 1. \tag{4.6}$$

Combining Eq. 4.4 and Eq. 4.5:

$$L_i^2 = y_{a-i}^2 + a_i^2. \tag{4.7}$$

Substituting Eq. 4.3 into Eq. 4.7:

$$\left(L_0 + a_i\right)^2 = y_{a-i}^2 + a^2. \tag{4.8}$$

Differentiating this expression with respect to time, one arrives at

$$2\left(L_0 + a\right)\frac{da}{dt} = 2y_a \frac{dy_a}{dt} + 2a\frac{da}{dt}$$

(4.9)

$$2\frac{da}{dt}L_0 + 2a\frac{da}{dt} = 2y_a\frac{dy_a}{dt} + 2a\frac{da}{dt}.$$

(4.10)

Simplifying, an expression for the tip velocity can be obtained as

$$\frac{da}{dt} = \frac{y_a}{L_0}\frac{dy_a}{dt}$$

(4.11)

and from this, the tip position at a given time is obtained. A plot of the tip position vs. time along with the extremity position (denoted $y_{a\text{-}i}$ in Figure 4.2) is shown in Figure 4.4. While the extremity position is linearly increasing in the vertical direction, the tip position does not increase at the same rate as the peel angle decreases. Figure 4.5 shows how the peel angle is related to the tip position independent of time, for a given L_0.

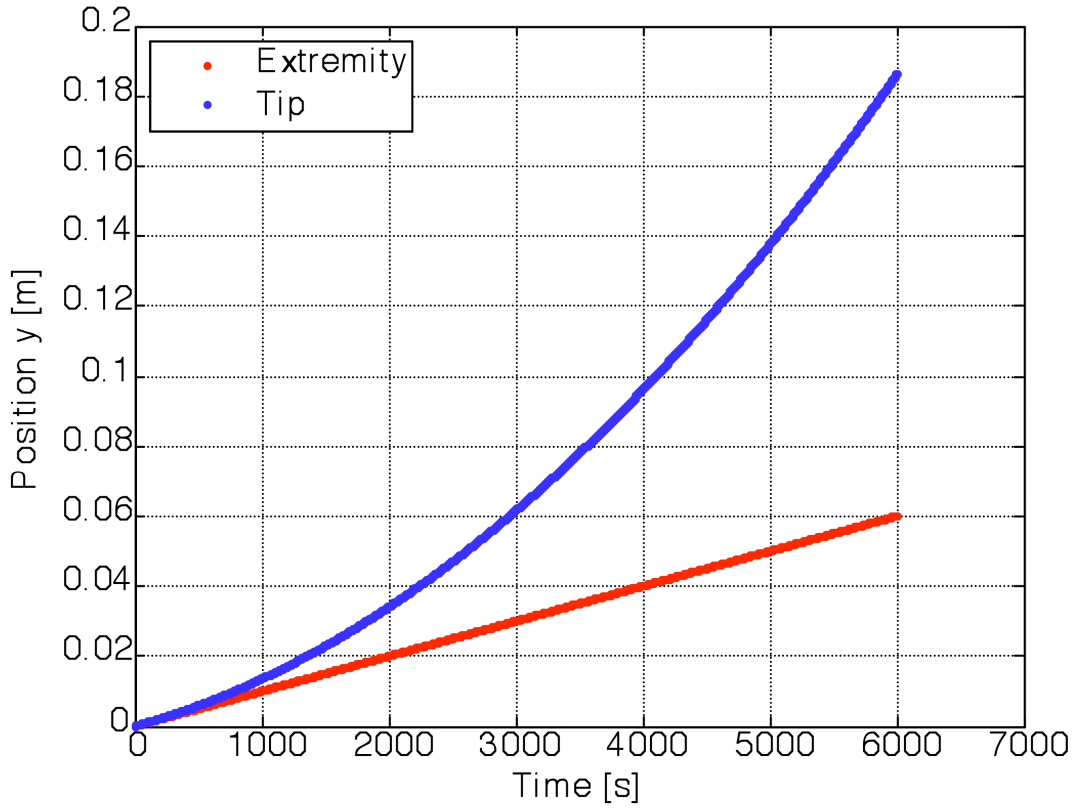

Figure 4.4: Position vs. time during a displacement controlled peel test for an initial peel arm length of L_0 = 12.7 mm (0.5”). The stage velocity is the prescribed velocity at the extremity of the tape, denoted by y_a in Figure 4.2.

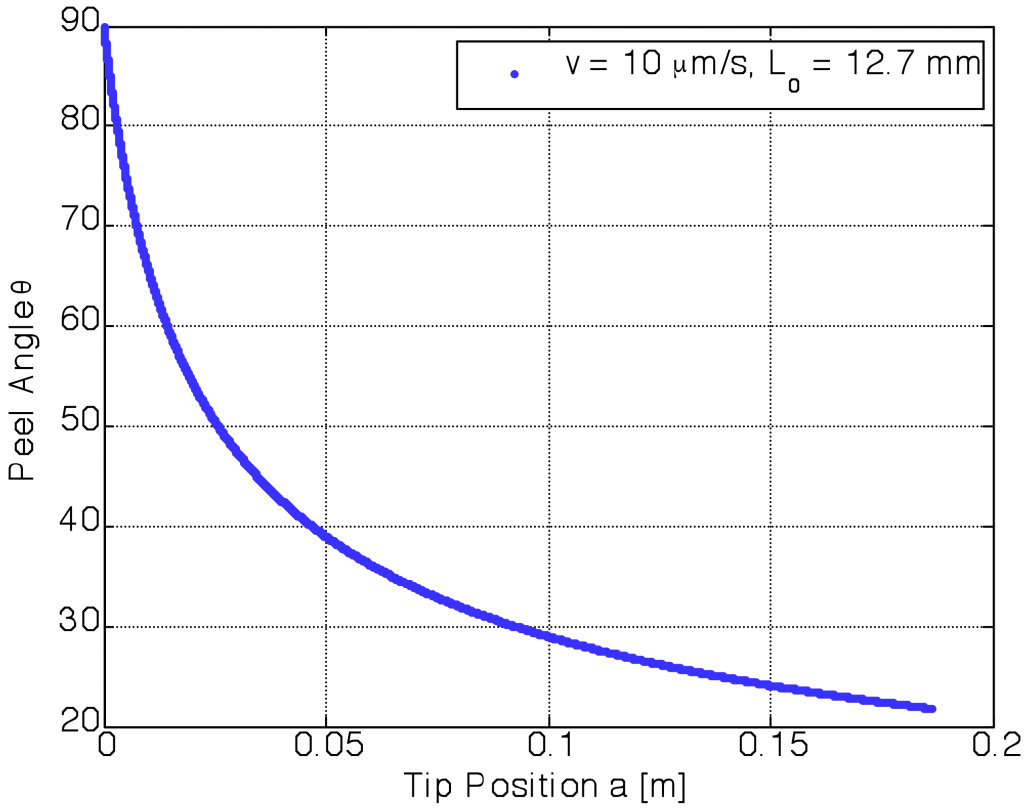

Figure 4.5: Peel angle, θ vs. tip position, a, for an initial peel arm length of L_0=12.7 mm (0.5").

4.5 Varying Peel Angle Tests Including Variable Width

As previously discussed, tests were conducted where the peel angle is forced to change very quickly in a single peel test. This will allow the tip velocity to change as a function of angle while the applied extremity velocity remains constant. It also allows for the examination of the peel force and adhesion energy for a range of angles through which the tape is being forced to move. Thus, there is less time for the adhesive to react and it is being forced to respond to the instantaneous tip velocity. This is in contrast to the constant-angle peel tests where equilibrium is reached and the values for these quantities

are taken from there. Though steady-state peeling is never achieved, the continuously varying angle tests provide insights concerning the rate-dependence of adhesion.

Recall from Chapter 1 that the adhesion energy G for a linear elastic extensible tape adhered to a substrate as given by Kendall is

$$G = \frac{P_f^2}{2Eb^2h} + \frac{P_f}{b}(1-\cos\theta). \tag{1.6}$$

For the experiments and analysis that follows, inextensibility of the tape is assumed, for which the adhesion energy given by Rivlin is

$$G = \frac{P_f}{b}(1-\cos\theta). \tag{1.7}$$

Figure 4.6 shows the tip velocity as a function of the peeling angle. From the starting peel angle of 90° to a peel angle of ~20°, the tip velocity is roughly five times greater than the prescribed velocity at the extremity (in this case, 10 μm/s).

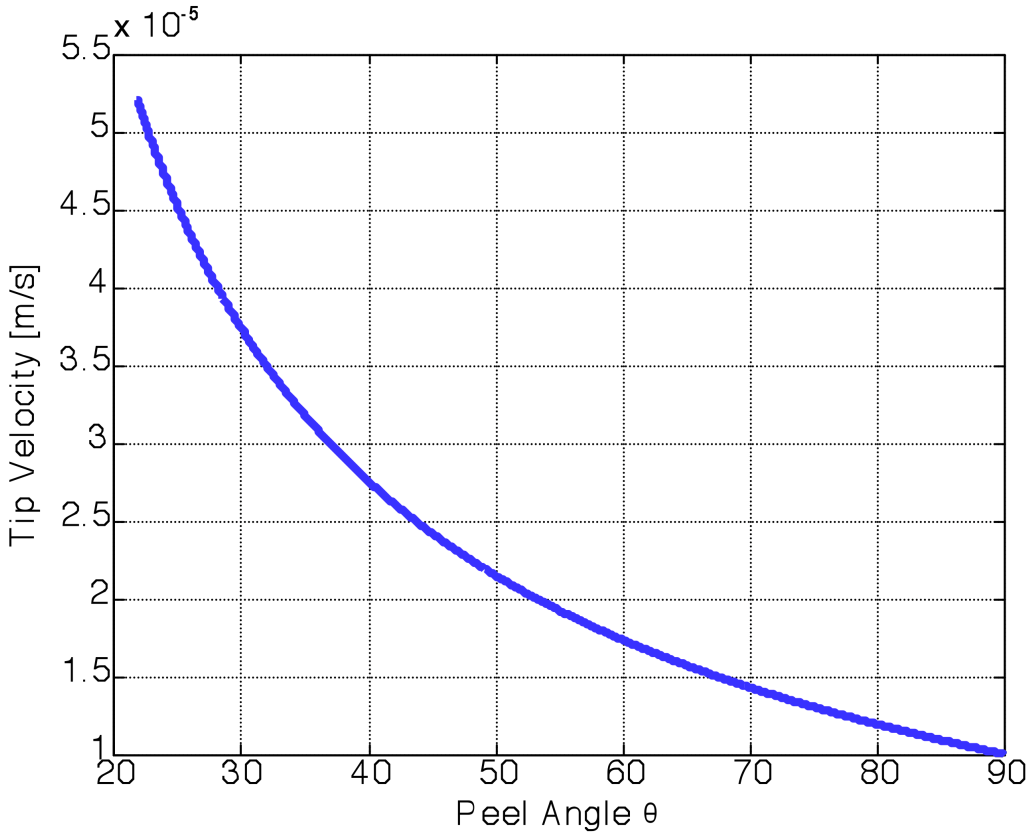

Figure 4.6: Peel angle, θ, vs. tip velocity, da/dt, for a varying-angle peel test for L_o = 12.7 mm (0.5").

In one set of experiments, a new parameter is introduced, namely a variable width for the adhesive tape. The width of the tape is usually kept constant (recall for the packing tape, b = 48 mm). Here, a linear decrease in width is introduced at a point where the tip position a = 50 mm from the beginning of the test, as shown in Figure 4.7. The variable width section is a linear function of the tape width, given by $y = b_0\left(1 - \frac{2}{5}x\right)$, where b_0 is the initial constant width of the tape. The width of the tape changes at $x = a_c$, as shown in Figure 4.7.

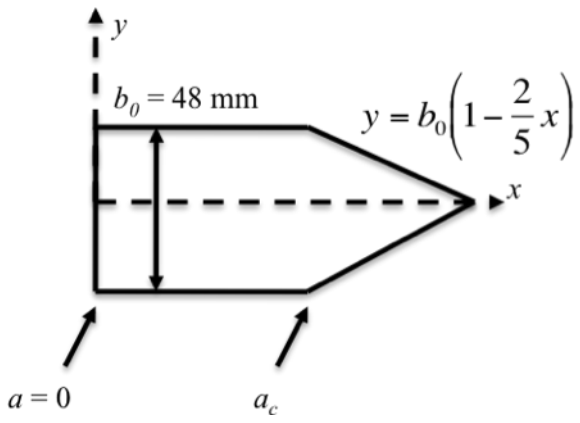

Figure 4.7: Schematic of variable width tape.

Peel tests are conducted with the packing tape for both constant and variable width sections. Several extremity velocities are tested: v_0 = 5, 10, 30, 60, 90 μm/s. For the extremity velocity of v_0 = 30 μm/s, the variable width is introduced. A plot of the peel force vs. tip position is shown in Figure 4.8.

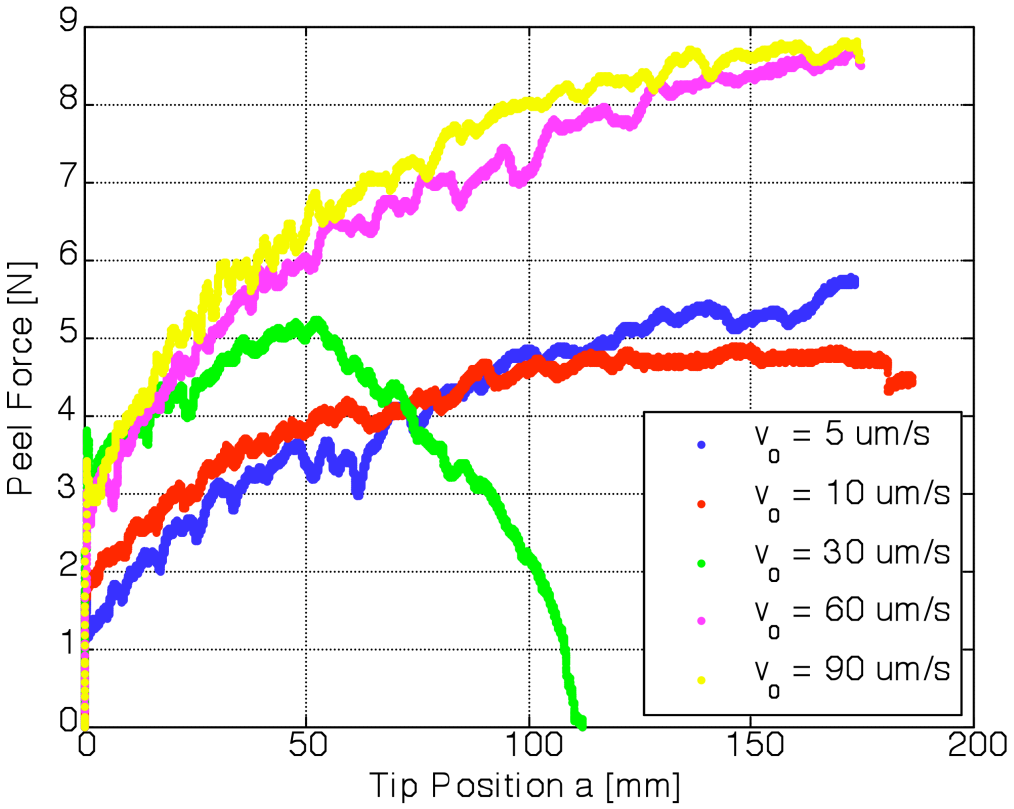

Figure 4.8: Peel force, P_f, vs. tip position, a, for various prescribed extremity velocities. The test at v_0 = 30 μm/s is for a variable width tape, with the width decreasing at a = 50 mm.

For a given extremity (applied) velocity, the peel force increases in all cases with tip position, which is a result of the decreasing peel angle. Since there exists a point where the angle will not change anymore regardless of how long the tip propagates, the peel force approaches the steady-state condition. It is also clear that the peel force for a given tip position increases as the tip velocity increases. Looking specifically at the v_0 = 30 μm/s, the change in width that commences at a = 50 mm also has an effect on the peel force. The peel force approaches zero at some tip position since the tape at this point is peeled completely off of the glass substrate.

The adhesion energy G is plotted below as a function of the peel angle, shown in Figure 4.9.

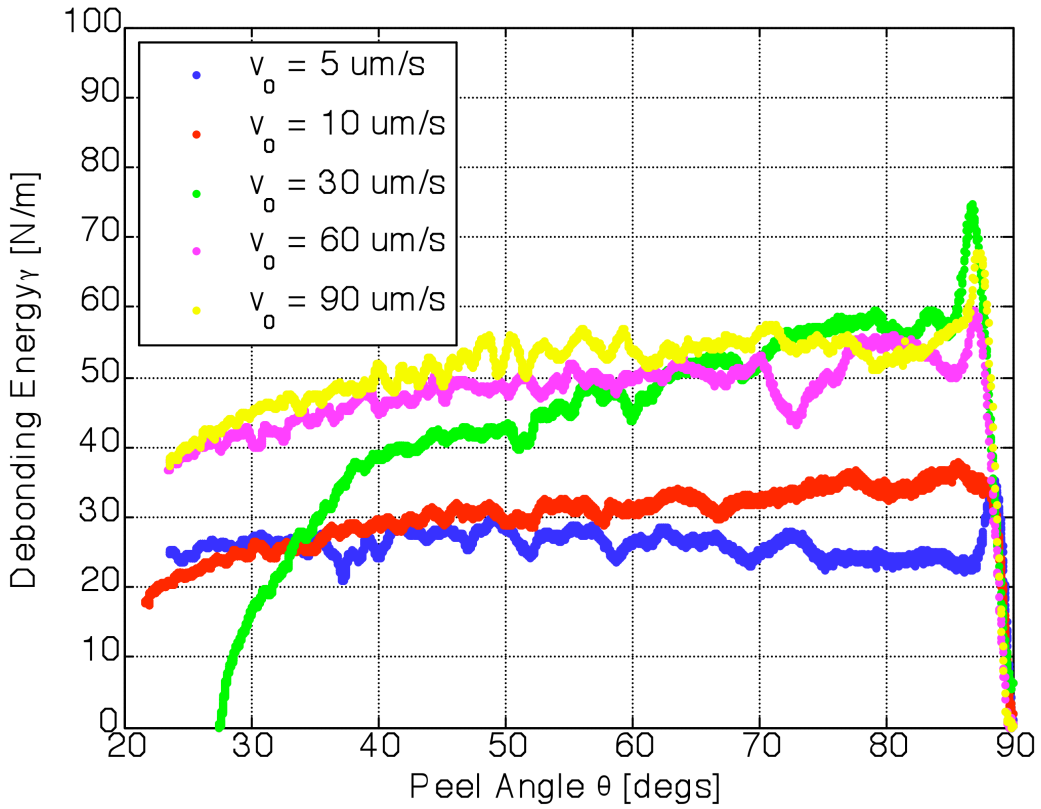

Figure 4.9: Adhesion energy, G, vs. peel angle, θ, for varying extremity velocities. The test at v_0 = 30 μm/s is for a variable width tape, with the width decreasing at a = 50 mm.

The adhesion energy appears to decrease as a function of peel angle for a prescribed extremity velocity. For a given peel angle, the adhesion energy increases as a function of the extremity velocity. Based upon these results, it can be hypothesized that the adhesion energy depends upon both the extremity/tip velocity and the peel angle (e.g., $G(v,\theta)$). However, it must be noted that the tip velocity and the peel angle are not independent of each other, as shown in Figure 4.6. Several previous studies assume the adhesion energy to be constant with respect to the peel angle [37, 38]. To examine this, separate measurements are conducted which examine G as a function of v and θ independently.

The change in width implemented in the v = 30 μm/s test is investigated in more detail in Chapter 5, on stability.

The conditions under which steady-state data might apply to transient loadings can be estimated by relating the size of the cohesive zone (measured experimentally in Chapter 2) to the change in tip velocity during a peel test. The steady-state solution applies so long as during the propagation history of the crack,

$$\frac{\dot{K}(t)}{K(t)} << \frac{\dot{a}(t)}{2\alpha(t)} \tag{4.12}$$

where $K(t)$ is the stress intensity factor, $\dot{K}(t)$ the change in stress intensity factor with time, $\dot{a}(t)$ the crack tip speed, and $\alpha(t)$ the length of the cohesive zone [51]. This expression states that differences between steady-state and transient conditions arise only if there are significant changes in the crack tip speed during the time interval when the crack passes through the cohesive zone. The right-hand side of Eq. 4.12 states that during the time when the stress intensity factor changes by an incremental amount, the distance traveled by the crack tip must be much larger than the cohesive zone size for the steady-state solution to apply. Starting from a peel angle of 90°, if the change in peel angle in which the stress intensity factor changes by an incremental amount is estimated to be 10°, Figure 4.5 shows that crack tip travels a distance of ~3 mm for this range. Recall from Chapter 2 that the size of the cohesive zone for peel angles of 80° to 90° is ~500 μm. Therefore, the ratio of the distance traveled by the crack tip to the cohesive zone size is

about six, which is not very large and suggests that in this case the steady-state data does not apply to transient loadings.

4.6 Constant Peel Angle Tests

As a result of the previous tests in the previous section, the relationship between the adhesion energy, G, with both the extremity velocity, v_0, and the peel angle, θ, need to be investigated independent of each other. This section aims to do this by conducting peel tests at constant angles, keeping the velocity constant for a given test at a given angle. Peel tests are conducted for a range of angles of 30° to 90° at rates of v_0 = 10 μm/s and v_0 = 50 μm/s. In all of the tests, the total tip position propagation is 6 mm. In all of these tests, the initial peel arm length is chosen to be in the range L_0 = 76.2mm (3") to 114.3mm (4.5"). The measured steady-state peel force, P_f, is plotted vs. peel angle, θ, and shown in Figure 5.10. The experimental data is plotted by the circles, with the Rivlin expression (Eq. 1.6) shown by the lines with values of the adhesion energy G chosen to fit each curve.

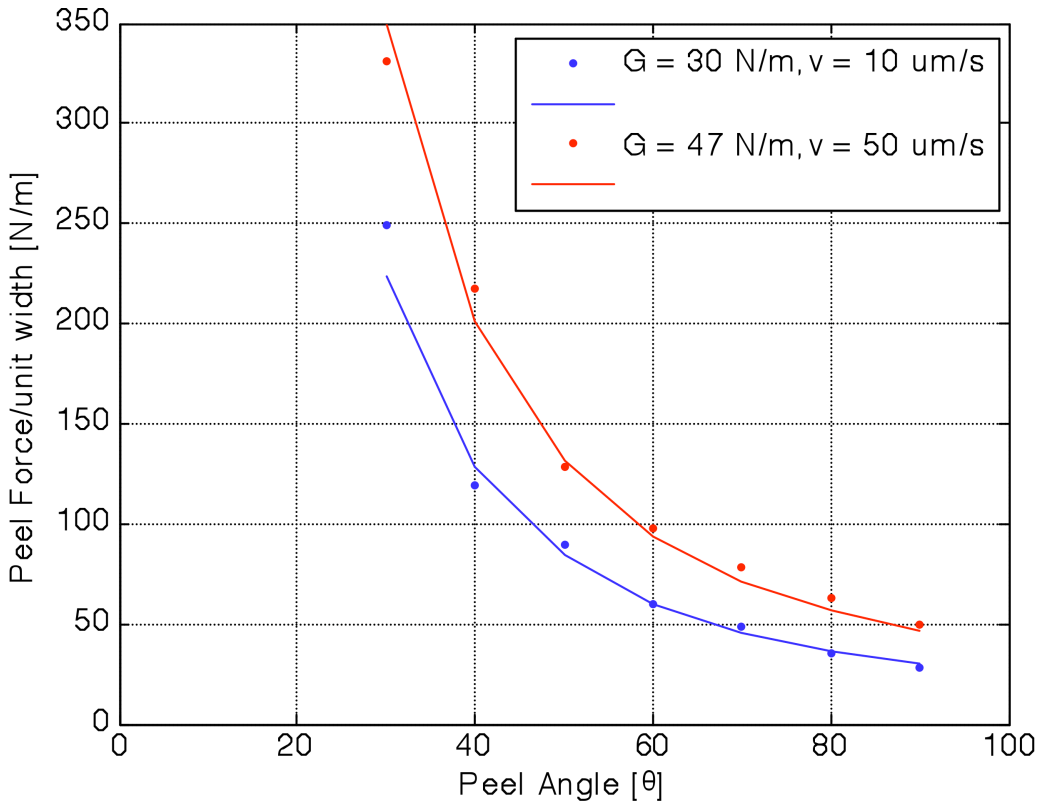

Figure 4.10: Steady-state peel force vs. peel angle for peel velocities of v = 10 μm/s and 50 μm/s for Scotch Packing Tape

This plot shows a clear dependence of the steady-state peel force, P_f on the peel velocity, v. For both velocities, the Rivlin relation fits the data quite well assuming a constant value of the adhesion energy, G. In attempts to make measurements at lower peel angles (0°, 10°, 20°), it is very difficult to obtain steady-state peel-force values. This is so because of the effect of extensibility at lower angles. To keep the peel angle constant at these lower angles, the peel arm length must be increased. As the peel angle approaches 0°, essentially a tensile test of the tape is being conducted, as opposed to a peel test. As is seen from the finite element simulations in Chapter 3, the force along the tape does not remain constant throughout the process zone, and very likely is not constant in other portions of the tape and adhesive. Future investigations can be geared towards

measuring this by utilizing a non-contact measurement technique such as digital image correlation (DIC) to examine strain and consequently stress in various portions of the tape sections during a peel test.

The adhesion energy as a function of rate and peel angle is also investigated. Figure 4.11 is a plot of the adhesion energy, G, vs. peel angle, θ, for the same tests in Figure 4.10. The adhesion energy here is calculated rather than fit (as in Figure 4.10) using the Rivlin relation (Eq. 1.6) along with the prescribed peel angle, θ and the experimentally measured steady-state peel force, P_f.

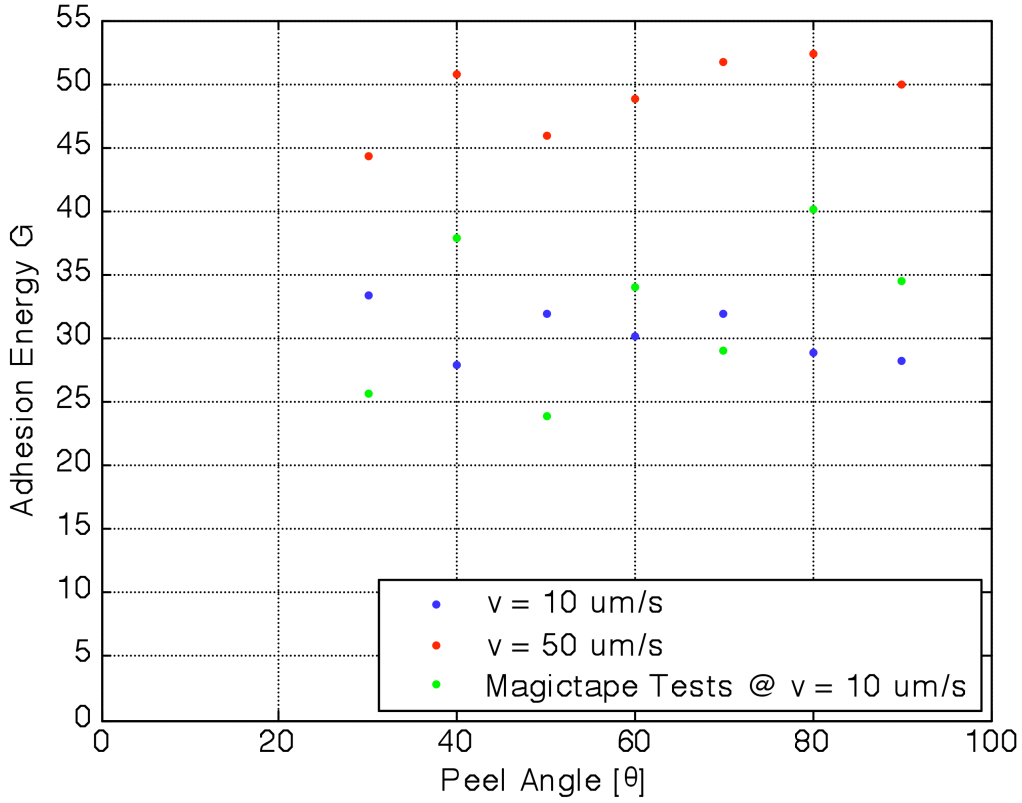

Figure 4.11: Adhesion energy vs. peel angle for peel velocities of v_0 = 10 μm/s and 50 μm/s for Scotch Packing Tape.

In addition to the tests conducted for the Scotch Packing Tape at given velocities, the plot includes data from the Scotch Magic Tape tests at v_0 = 10 μm/s from Chapter 2 for comparison. For all three sets of data, the adhesion energy is constant with respect to a given peel angle for a given peel rate. Comparing the values of G for the Magic Tape and Packing Tape at v_0 = 10 μm/s, the values are almost the same, suggesting that the two tapes have similar adhesive properties. The two materials also have similar elastic moduli, E = 1.65 GPa for the Magic Tape versus E = 1.60 GPa for the Packing Tape. There is also more scatter in the data for the Magic Tape as compared to the Packing Tape. This can be attributed to the different widths of the two tapes used for testing, b = 19 mm for Magic Tape, b = 48 mm for Packing Tape. Because the Magic Tape is narrower, the effects of any misalignment in the experiment are amplified and can be a cause of more substantial error in the results, as seen in Figure 4.11.

Finally, a clear dependency of the adhesion energy on the peel velocity (e.g., $G(v)$) exists, as the adhesion energy for a given angle is greater for the peel tests at higher peel velocity. While G is not a function of the peel angle, it is indeed a function of the peel velocity, v.

4.7 Rate-Dependent Law for the Peel Test

Based upon the results of the previous section, which show a dependency of the adhesion energy on the peel velocity, tests are conducted at several peel velocities using a constant-angle peel configuration with a constant peel angle θ = 90°. The goal is to develop a rate law between the adhesion energy, G, and the peel velocity, v, for a range of velocities. Figure 4.12 shows the adhesion energy plotted against the peel velocity for

peel velocities of v = 2, 10, 50, and 100 μm/s for a peel angle of $\theta = 90°$, and the same data is plotted on a logarithmic scale in Figure 4.13. For this peel angle, the adhesion energy given by the Rivlin relation is equivalent to the peel force, P_f, per unit width, b.

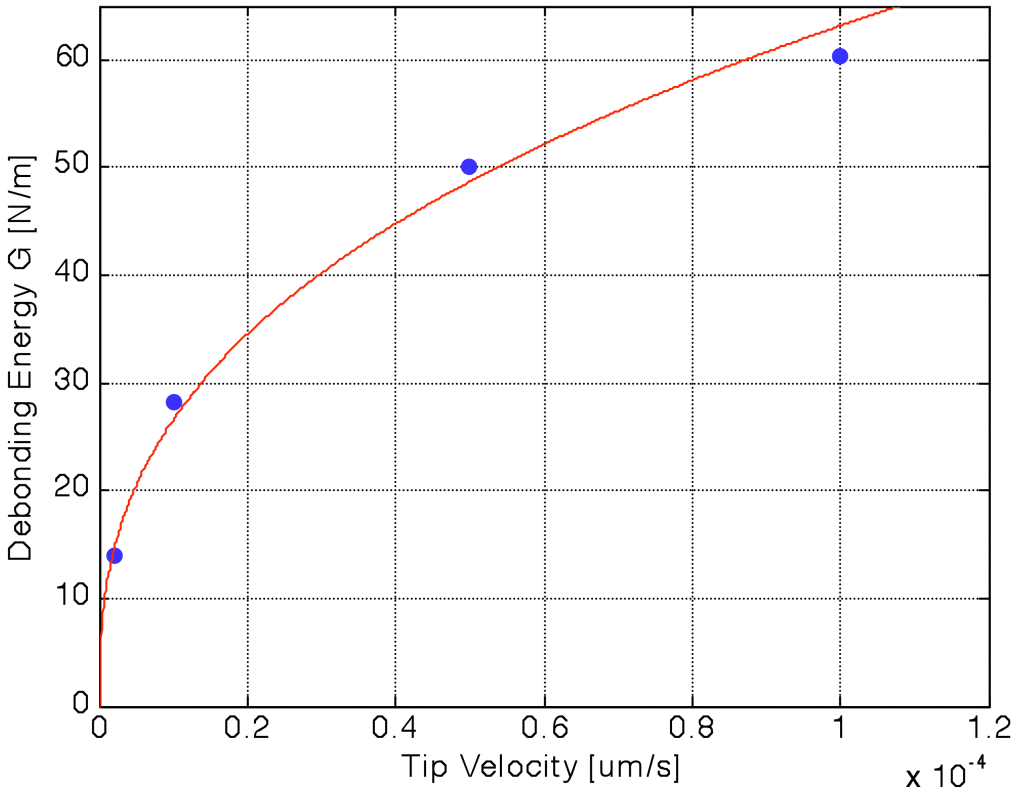

Figure 4.12: Adhesion energy, G, vs. peel velocity, v, for various tip velocities. The curve is fit with a power-law relation.

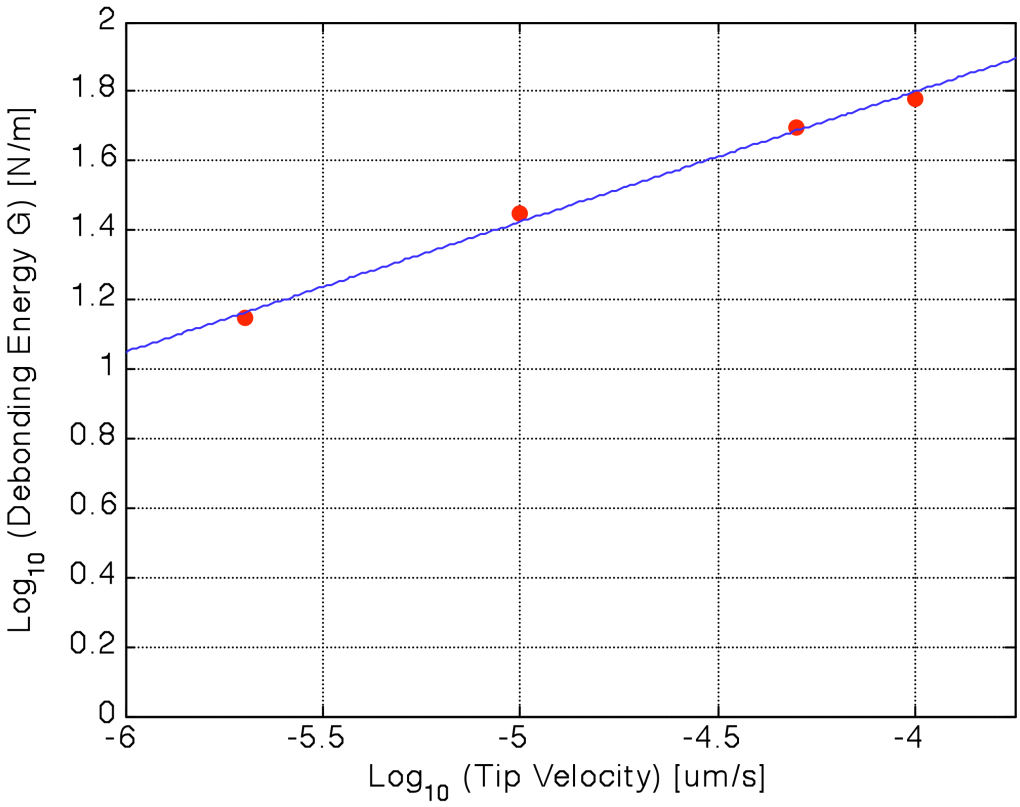

Figure 4.13: Adhesion energy, G, vs. peel velocity, v, on a logarithmic scale for different tip velocities. The curve is fit with a linear regression line.

There exists a clear linear trend between G and v here on the log-log plot as seen in Figure 4.13. A fit of this curve as shown is given by

$$\log G(v) = 0.3757 \log v + 3.3032 \tag{4.13}$$

This yields a power-law expression for this material system given by

$$G(v) = G_0 \left(\frac{v}{v_0} \right)^{0.3757} \tag{4.14}$$

where v_0 and G_0 are reference values for a peel velocity of 1 μm/s and the corresponding value for adhesion energy, respectively. For this system, G_0 = 11.2 N/m at v_0 = 1 μm/s.

This law compares well to similar rate-dependent studies of adhesive materials [52, 53], albeit with different empirical constants.

4.8 Conclusions

This chapter has examined the effect of rate on the peel force during the peel test for a material system of Scotch Packing Tape adhered to a rigid glass substrate. Using a new peeling configuration, a set of three experiments were conducted in order to specifically investigate the relationship between the adhesion energy, the peel angle, and the peel velocity. Initial experiments where the peel angle was changed rapidly suggested a dependence of the adhesion energy, G, on the peel velocity, v, and the peel angle, θ. Further experiments showed that at a constant peel velocity, the adhesion energy remained constant for the entire range of peel angles tested. Finally, experiments conducted at a constant peel angle of 90° for varying velocities showed a clear power-law rate-dependency of the adhesion energy on the peel velocity.

Chapter 5

Stability of Peeling

5.1 Introduction

A fundamental question of interest in peeling is the stability of this process. The role of various parameters including adhesion energy, compliance of the loading system, and geometry of the tape on the stability of the peeling needs are of interest. Recent studies have focused on understanding the role of stability in the gecko adhesion problem [5, 6], particularly with regard to the force distribution in the contact of the gecko's foot to a surface and the detachment of setae. This study aims to investigate the stability including the role of compliance during a peel test through implementation of a force-controlled experimental configuration. Experiments are conducted that monitor the tip position of an inextensible adhesive tape over time subject to a constant applied load at the tape extremity while the width of the tape is decreased as a function of the tape length. In addition to examining the effect of the applied load and the change in width on the stability of the debonding process, the stiffness of the system is varied by altering the magnitude and direction of the applied load during a test. This change in stiffness also affects the tip velocity, and can be tuned to trigger or delay the onset of instability. Theoretical stability criteria are also presented to develop insights of the role of parameters investigated experimentally. The stability of peeling can be viewed as a classical application of stability concepts in fracture mechanics to the peel test [42].

5.2 Experimental Method – Controlled Stiffness

To investigate the stability of the peel test, a force-controlled experimental setup is developed in which a constant force is applied to the extremity of the tape and the tip position is monitored over time for a given test. Figure 5.1 is a detailed view of the experimental configuration implemented in the laboratory.

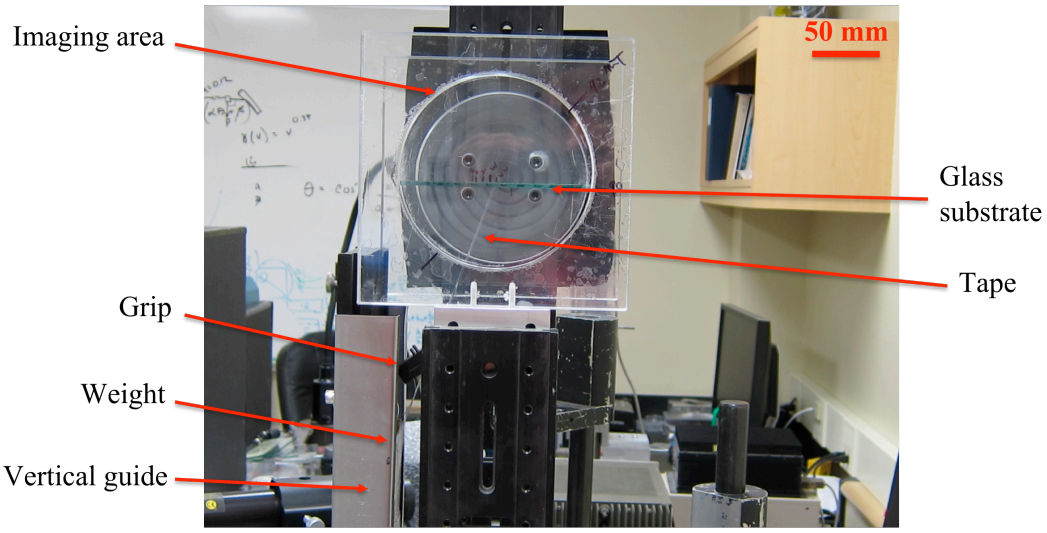

Figure 5.1: Force-controlled configuration for investigating stability of peeling of elastic tapes.

For the experiments conducted here, Scotch Packing Tape (3M, Minneapolis, MN) is used as the model material. This tape is chosen because of its large width (b = 48 mm), which will be useful in investigating the effect of variable width on the stability of the peeling process. The tape is adhered to the underside of a glass substrate with dimensions 127 mm x 127 mm x 3 mm (5” x 5” x 1/8”). Prior to testing, the glass surface is cleaned with acetone, followed by isopropanol, and left to dry. The adhesive tape is applied to the glass surface with a roller to minimize the presence of air pockets between the tape and the substrate. Ideally, it appears that the longer the adhesive is left on the surface once

attached before testing, the more steady a peel force can be obtained, along with more consistent results. Based on this observation, to minimize experimental variations, all tests are conducted after the adhesive is left to sit for 30 minutes prior to testing. Due to the stochastic nature of this process, great care is taken in being consistent in the process of applying the adhesive to the surface.

The glass substrate is held between two acrylic glass plates, each with a 127 mm (5") radius cut-out with depth of 12.7 mm (0.5"). This allows for the substrate to be rotated and set at any angle for the beginning of a test. The acrylic glass plates are bolted to an optical rail on each side (304 mm (12") and 457 mm (18") in height, respectively), which are fixed to an optical table. Two pieces of delrin held together by two screws are used as a grip to clamp the end of the tape. To attach the weight, numbers of small spherical beads each weighing approximately 0.3 g are placed into a rectangular receptacle constructed from corrugated cardboard (hidden by the vertical guide in the figure). The receptacle is tied to the front and back ends of the screws of the delrin grip with 89 N (20 lbf) fishing wire. The use of small spherical beads allows for small increments of weight to be added or removed. A vertical guide is formed using a thin aluminum sheet attached to a 304 mm (12") optical rail, which is mounted vertically. This guide restricts the applied load to movement in the vertical direction only. Thus, as the load descends vertically when the tape is peeled, the peel angle θ will change throughout the test.

The tip position of the tape is imaged and monitored during the tests. Recall from Chapter 4 that the tip position, a, is defined as the contact point between the tape and the glass substrate. The tip is imaged with a 2-megapixel monochromatic digital CCD

camera (UP-2000CL B/W, Uniqvision, Santa Clara, CA). The camera is attached to an optical post, which is attached to a series of manual translation stages (Newport Corporation, Irvine, CA) to allow for fine adjustment of the camera. The camera and mounting configuration is not shown Figure 5.1.

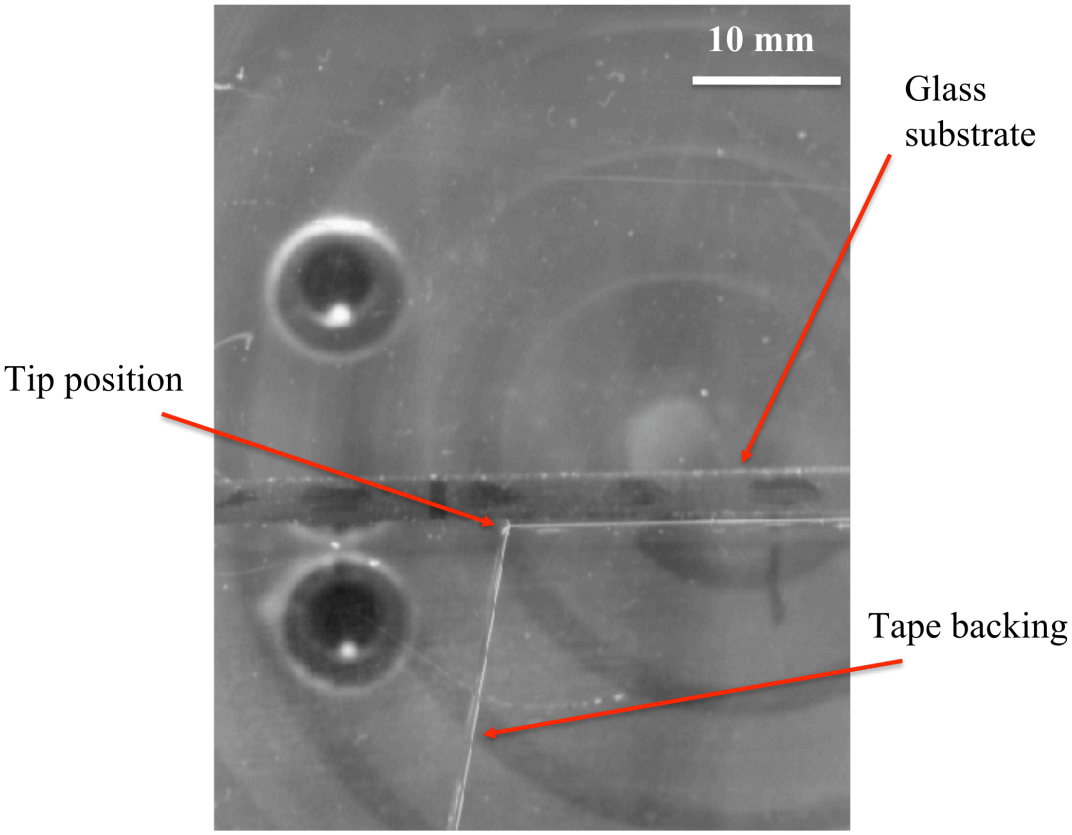

Figure 5.2: Image of the tip position, *a*, as acquired with a CCD camera during a force-controlled peel test.

For these experiments, one image is acquired every 5 seconds for the duration of the test. To determine the length scale from the image, an image of sets of line pairs from a 1951 USAF target grid is acquired prior to testing. This image allows for determination of the scaling factor in units of mm/pixel. Figure 5.2 shows a sample image of the tape

debonding from the glass substrate during a test. To track the tip position, a, over time, all of the images from a given test are loaded sequentially in Matlab (Mathworks, Natick, MA) and the tip position is selected manually. The selected tip position is stored for each image and subsequently tracked over time, as is shown in a later section.

Using this specific experimental configuration, tests are conducted to examine the tip position of the tape as a function of time for different combinations of applied loads. The tests use a tape that goes from constant to variable width, as shown in Figure 5.3, which is used to investigate effect of the change in width on tip velocity and stability. The variable width section is a linear function of the tape width, given by $y = b_0\left(1 - \frac{2}{5}x\right)$, where b_0 is the initial constant width of the tape. The width of the tape changes at $x = a_c$, as shown in Figure 5.3.

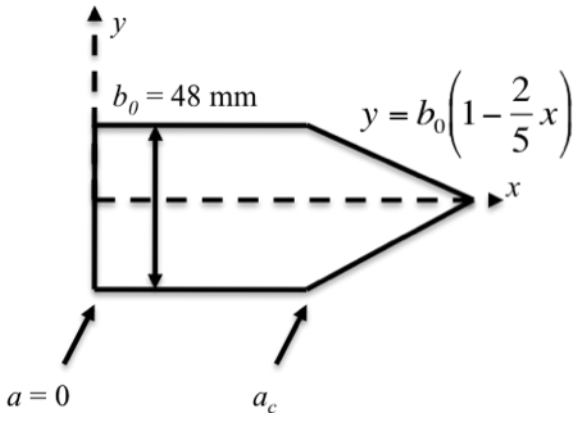

Figure 5.3: Schematic of variable width tape used in the peeling tests.

An initial constant weight P_0 is applied at an initial peel angle of $\theta = 90°$ and the tip position is imaged as the tape peels from the substrate in the section of constant width (a = 0 to 50 mm). After some time increment has passed, the weight is increased to P_1. This

new increased weight will cause the tip to propagate at a faster rate and take it into the variable width section. The change in tip velocity, *da/dt*, is investigated for different combinations of P_0 and P_1.

5.3 Debonding Stability Criteria

Figure 5.4 shows a schematic of the force-controlled peeling configuration. An elastic adhesive tape is adhered to a rigid substrate with a peel angle θ. A set of forces F_{perp} and F_{par} are applied to the extremity of the tape in the directions perpendicular ($\theta = 90°$) and parallel to the substrate ($\theta = 0°$), respectively.

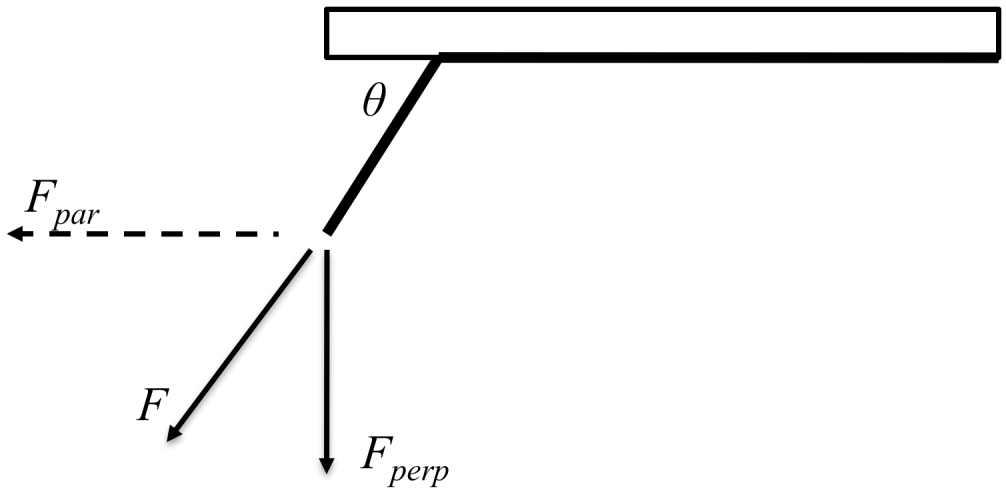

Figure 5.4: Schematic of the force-controlled peel configuration. *F* is the resultant axial force acting along (θ) the backing of the tape.

These two forces form a resultant force *F* along the tape backing, which is expressed as

$$F = \sqrt{F_{par}^2 + F_{perp}^2} \,. \tag{5.1}$$

The experimental realization of such a test can be considered by hanging a fixed load from the extremity of the tape (F_{perp}) with a separate tensile force imposed horizontally (F_{par}), simultaneously. The details of the applications of these forces are discussed in the next section on experimental methods. Recall that the peel force, P_f, is measured along the backing of the tape. The parameter F_{perp} is the force applied in the perpendicular direction with respect to the substrate. The peel force $\hat{P}_f$ is the total peel force used in the Rivlin relation for determining the adhesion or debonding energy. Recall the Rivlin relation from Chapter 1:

$$\hat{P}_f = \frac{Gb}{1-\cos\theta}, \tag{5.2}$$

where b is the width of the tape, θ is the peel angle, and G is the adhesion or debonding energy. Stability criteria for the debonding of the tape during the peeling process can be examined by considering the relation between the peel force $\hat{P}_f$ used in the Rivlin relation and the perpendicular force (applied load), F_{perp}. To resolve F_{perp} in the direction of the peel force, $\hat{P}_f$, the generalized resultant force F is introduced. For the Rivlin expression, the driving force F, which is the resultant of the applied load, is equivalent to the peel force, $\hat{P}_f$. The applied load, F_{perp}, can be related to the resultant force F through geometry,

$$F = \frac{F_{perp}}{\sin\theta} \tag{5.3}$$

Figure 5.5 shows the relation between the force, F, and the peel angle, θ. The solid curve represents the resistance to peeling given by the Rivlin expression (Eq. 5.2), while the dashed curve represents the driving force for debonding due to the applied load (Eq. 5.3).

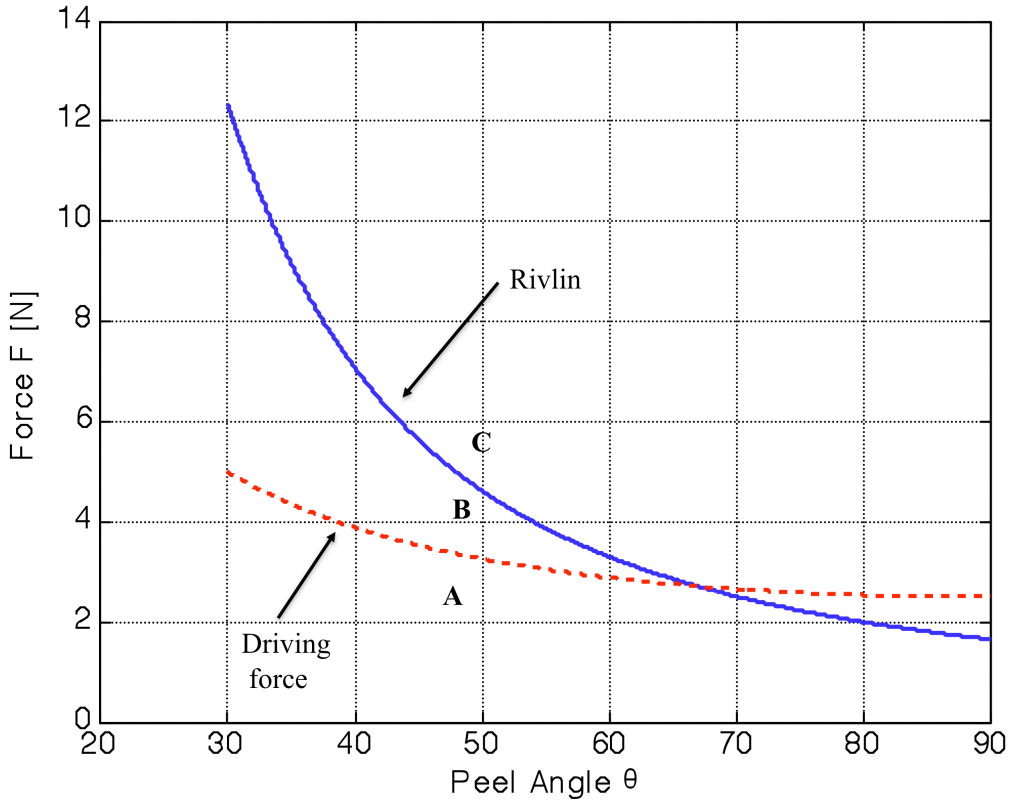

Figure 5.5: Force, F, as a function of the peel angle, θ. The solid curve represents the resistance to peeling given by the Rivlin relation, while the dashed curve represents the driving force for debonding due to a specified applied load, F_{perp}.

The Rivlin curve in Figure 5.5 represents the equilibrium state of peeling or intrinsic material resistance to debonding. For a given angle θ, there is a corresponding force on the Rivlin curve that defines the equilibrium force at which peeling will not occur. That is, for some load F at an angle θ on the Rivlin curve, the tape will not debond. For the

tape to debond, the peel angle must be increased or the applied force must be increased. The three regions denoted A, B, and C correspond to regions of stability criteria. When the driving force ($F_{perp}/\sin\theta$) curve is above the Rivlin curve (region C), unstable debonding will occur. For the point of intersection between the driving force and Rivlin curves (region B), stable debonding will occur. Finally, when the driving force curve is below the equilibrium curve, no debonding will occur and peeling will be arrested.

To best understand the utility of Figure 5.5 in the force-controlled peel-tests, consider the case where a constant load F_{perp} is applied for a tape of constant width at an initial peel angle of 90˚. This corresponds to the dashed curve in Figure 5.5. At this point, the driving force curve is above the equilibrium Rivlin curve, designated region C on the plot. Debonding in this region is unstable, as the tape will peel off and the tip position, a, will advance. As the tape is peeled, the angle will decrease, as described in the experimental setup section. Following the driving force curve, eventually at an angle of θ = 68˚, this curve will intersect the Rivlin curve. At this intersection, the tape will no longer debond and the propagating tip will arrest. This is the case of stable debonding. For the tape to debond further, a larger force must be applied, so as to shift the driving force curve up the vertical axis. An example is shown of a larger force being applied in Figure 5.5. Note how the driving force curve is now shifted up in comparison to Figure 5.4 as a result of this increase in applied load. For the same angle θ = 68° where the intersection of the two curves occurs in Figure 5.5, Figure 5.6 shows the case of unstable peeling since the force F is increased.

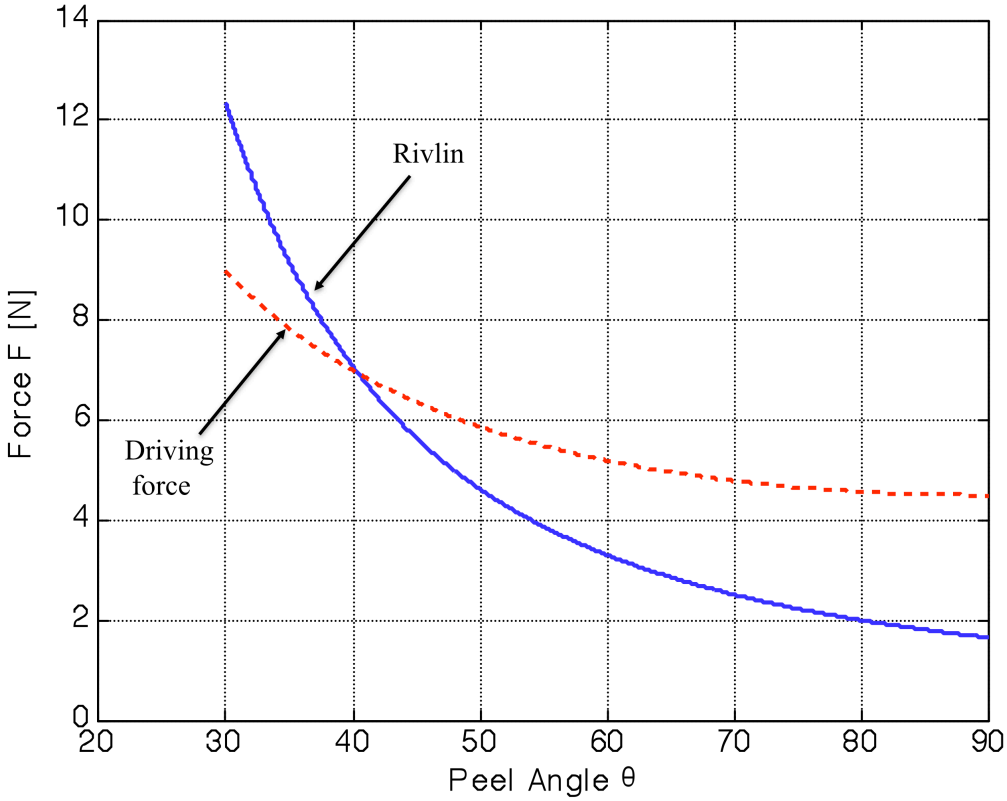

Figure 5.6: Force, F, as a function of the peel angle, θ, for an increase in applied load, F_{perp} (with respect to Figure 5.5). The solid curve represents the resistance to peeling given by the Rivlin relation, while the dashed curve represents the driving force for debonding due to the applied load, F_{perp}.

5.4 Experimental Method – Role of Stiffness in the Parallel Direction

In Section 5.2, a force-controlled peeling configuration is described that confines the applied force vertically (F_{perp}), restricting the movement of the weight horizontally. This corresponds to a system with infinite stiffness ($K = \infty$) parallel to the substrate. As alluded to in the introduction, it is interesting to examine how varying this stiffness, K, which will alter the parallel force F_{par}, in addition to varying the applied load, F_{perp} affects the stability of the peeling process. Consider an elastic string that can be attached to the extremity of the tape to apply the parallel force F_{par}. While the elastic modulus, E,

of the string is a property of the material, the stiffness, K, is a property of the structure. K is generally defined as

$$K = \frac{F_{par}}{\delta} \tag{5.4}$$

where F_{par} is the force and δ is the resultant displacement. Relating Eq. 5.4 to the geometry and material properties:

$$K = \frac{Ewt_s}{L} \tag{5.5}$$

where w, t_s, and L are the width, thickness, and length, respectively, of a elastic string of rectangular cross section. If the length and thickness of the string remain constant, as the width (w) of the string is increased, the stiffness, K, will increase, for a constant thickness, t_s.

To investigate the effect of the compliance of the system experimentally, an experimental setup is developed based upon the vertically-guided setup in Figure 5.1. This new experimental arrangement is shown in Figure 5.7.

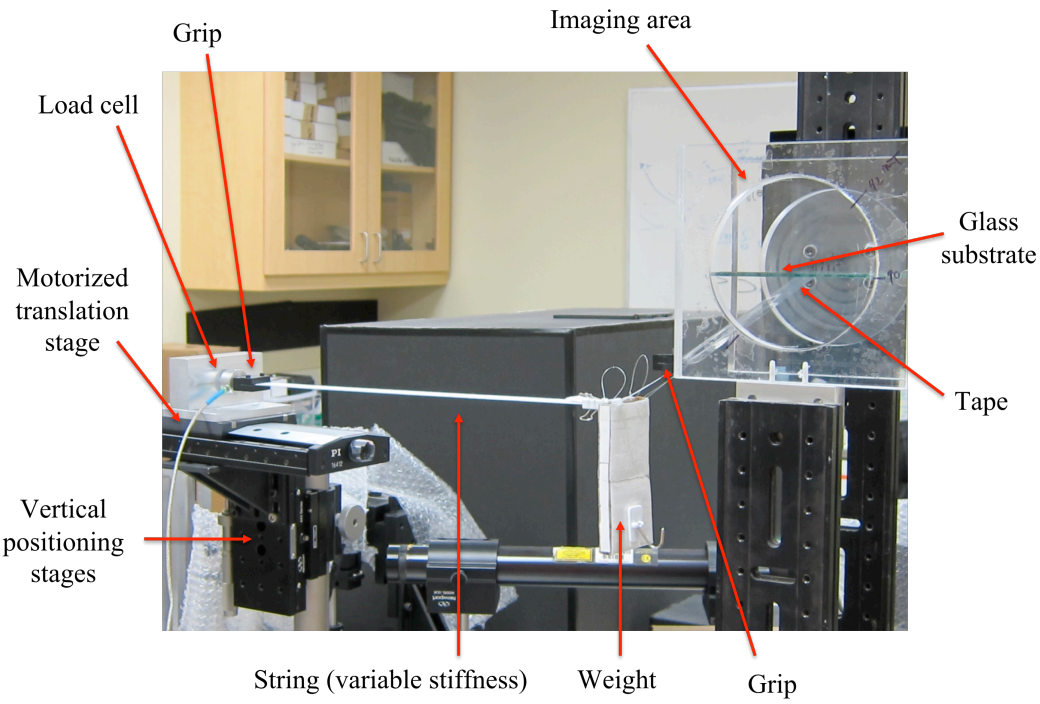

Figure 5.7: Variable stiffness experimental setup, which incorporates a string parallel to the substrate attached to the tape in addition to the vertically guided weight.

The tape used in these experiments is Scotch Packing Tape (3M, Minneapolis, MN). The tape is adhered to the glass substrate in the same manner as in Section 5.2. The glass substrate is held between two acrylic glass plates, each with a 127 mm (5") radius cut-out with depth of 12.7 mm (0.5"). This allows for the substrate to be rotated and set at any angle for the beginning of a test. The acrylic glass plates are bolted to an optical rail on each side (304 mm (12") and 457 mm (18") in height, respectively), which are fixed to an optical table. Two pieces of delrin are used as a grip to clamp the end of the tape, held together by two screws. To attach the weight, numbers of small spherical beads each weighing ~0.3 g are placed into a rectangular receptacle constructed from corrugated cardboard (hidden by the vertical guide in the figure). The receptacle is tied to the front and back ends of the screws of the delrin grip with 89 N (20 lbf) test fishing wire. The

use of small spherical beads allows for small increments of weight to be added and subtracted, which can be used to alter F_{perp}.

To implement a variable stiffness in the horizontal direction, an elastic string with a thickness (t_s) of 1 mm (elastic strap, Michael's, Irving, TX) is woven through a slot in the weight receptacle and clamped at the end with a fastener. Variable lengths and widths of the elastic string will be used, and are described in detail later in this chapter and will be used to alter F_{par}. The string is clamped at the other end by a similar delrin grip to the one used to hold the extremity of the tape. The grip is screwed on to a 500 g load cell (ALD-MINI-UTC-M, AL Design, Inc., Buffalo, NY), which is attached to an aluminum T bracket and fixed to a motorized translation stage (M-410.CG, Physik Instrumente, Irvine, CA). The stage has a total travel range of 100 mm, a maximum velocity of 1 mm/s, and resolution of 100 nm. The stage is used to apply a crosshead displacement to the string, effectively changing the force in the horizontal direction, F_{par}. The stage is mounted on an optical T bracket, which is attached to a linear translation stage mounted vertically on an optical post. The optical post is mounted to a separate linear translation stage fixed to an optical table. As the applied weight falls when the tape is peeled, the height of the motorized translation stage is manually adjusted in small increments to keep the string stiffness direction parallel to the substrate plane.

The load from the load cell is monitored in-situ with a digimeter (MD-40, Newport, Irvine, CA), configured to show the output force from the load cell in grams. The initial parallel force, F_{par0}, is determined by setting the tension in the string and observing the value through the digimeter. The parallel force F_{par} is decreased during a test by moving

the stage towards the tape and substrate during a test, resulting in the tension in the string being decreased. Data is acquired at a rate of five samples per second for the duration of a test from the load cell through a virtual instrument created in Labview (DAQM02, National Instruments, Austin, TX). The test times are typically on the order of one hour (3600 s).

Two separate types of tests are conducted with this configuration. The first is for a tape of constant width. Tests are conducted with two different string widths of w = 12.7 mm (1/2") and 6.35 mm (1/4"), for varying combinations of F_{perp} and the initial F_{par0} force which produce the same resultant force F. The tape is set at a shallow initial peel angle to change the equilibrium condition quickly along the driving force curve to propagate the peel. The stage is set to move at a velocity of 150 μm/s for the entire duration of the test, slowly releasing the tension in the string and thus decreasing F_{par}. The goal is to investigate how altering the parallel and perpendicular force components affect the tip velocity and, hence, the stability of peeling.

In the second set of tests, the width of the tape is varied as in the infinite stiffness tests of Section 5.2. For all tests, a single string width of w = 12.7 mm (1/2") is used along with values of F_{perp} and F_{par0} of 300 g and 350 g, respectively. In these tests, the horizontal loading stage is moved so as to decrease the tension in the string for varying amounts of time and then stopped. By stopping the stage at different times, the parallel force component F_{par} will be different and its effect on the stability, particularly in the variable width portion of the tape, can be examined.

5.5 Theory of Stability for Peeling

Consider an inextensible tape with width b. The debonding energy G is assumed to be independent of the peel velocity v as well as independent of the peel angle θ. While the results of Chapter 4 contradict the assumption of the debonding energy being rate-independent, the peel velocities examined in this study are an order of magnitude slower than the peel velocities in Chapter 4. The typical peel velocities (tip speeds) in the present investigation range from 3 to 10 μm/s. Furthermore, the aim of this work is to examine the stability of the peeling process, not the rate-dependency of the process. Let P_f be the peel force per unit width of tape, previously defined as $\hat{P}_f / b$.

The following expression serves as the basis for examining the stability in peeling of tapes [54],

$$\frac{d\left(\overline{G} - Gb\right)}{da} = -\frac{\frac{bf}{L_0}\left(1-\cos\theta\right)^2 + b' P_f \left(1-\cos\theta\right)\left(\sin^2\left(\theta\right) + \frac{bP_f}{KL_0}\right)}{\sin^2\left(\theta\right) + \frac{bP_f}{KL_0}} \tag{5.6}$$

where $\overline{G}$ is the energy release rate, b' the derivative of the tape width with respect to position (i.e., db/da), L_0 is the initial length of the peel arm, θ is the current peel angle, a is the current position of the tip, and K is the string stiffness. The energy release rate represents the energy available in the system available for debonding provided externally through the applied loading, F. The stability of peeling and its dependence on the string

stiffness is analogous to the stability of crack in a fracture specimen and its dependence on machine compliance [42].

From examining Eq. 5.6, criteria for debonding are established. Debonding will occur when

$$\overline{G} - Gb = 0 \tag{5.7}$$

For the case of debonding, stability criteria can also be established. The debonding is unstable if

$$\frac{d\left(\overline{G} - Gb\right)}{da} > 0, \tag{5.8}$$

while the debonding is stable if

$$\frac{d\left(\overline{G} - Gb\right)}{da} < 0. \tag{5.9}$$

Consider now the variable stiffness tests described in Section 5.5. For the case of a tape with constant width ($b' = 0$), the expression in Eq. 5.6 can be simplified:

$$\frac{d\left(\overline{G} - Gb\right)}{da} = -\frac{\frac{bP_f}{L}\left(1-\cos\theta\right)^2}{\sin^2\theta + \frac{bP_f}{KL}} < 0. \tag{5.10}$$

For this case, debonding is always stable. Now consider the case where the tape width decreases linearly as a function of the tape length ($b' < 0$), as shown in Figure 5.2. Debonding here is unstable if

$$\frac{bP_f}{L}(1-\cos\theta)^2 + b'P_f(1-\cos\theta)\left(\sin^2\theta + \frac{bP_f}{KL}\right) < 0, \tag{5.11}$$

or, simplified in a more convenient form,

$$b' < -\frac{b}{L}(1-\cos\theta)\left(\sin^2\theta + \frac{bP_f}{KL}\right)^{-1}. \tag{5.12}$$

These results show that as the string stiffness, K, is decreased, the system moves towards the unstable state. By manipulating the string stiffness K, the system can be moved between stable and unstable peeling. Important observations are made by examining the two extreme cases for the string stiffness: $K = \infty$ and $K = 0$. When $K = \infty$ (prescribed or dead load), this corresponds to the experimental configuration of Section 5.2 where the weight attached to the extremity of the tape is vertically guided. In this case, the stability criterion takes the form

$$b' < -\frac{b}{L}(1+\cos\theta)^{-1}. \tag{5.13}$$

For this specific case, consider two separate tests, denoted #1 and #2, in which the same initial values are imposed for the width, peel arm length, and peel angle, b_o, L_o, and θ_0. The difference will be in the relation between the change of width and Eq. 5.13 such that for test #1:

$$b' > -\frac{b_0}{L_0}\left(1+\cos\theta_0\right)^{-1},$$

(5.14)

and for test #2:

$$b' < -\frac{b_0}{L_0}\left(1+\cos\theta_0\right)^{-1},$$

(5.15)

For the case of test #1, the debonding of the tape is initially stable. However, for test #2, the debonding is initially unstable. Thus, by tuning the parameters b_0, L_0 and θ_0 with respect to the value of b', an instability can be triggered or avoided. It should be noted that for the case of $b' < 0$, debonding is always unstable.

Finally, considering the other stiffness extreme of an infinitely soft string where $K = 0$ (prescribed displacement), Eq. 5.6 can be expressed as

$$\frac{d\left(\overline{G} - Gb\right)}{da} = -b' P_f \left(1-\cos\theta\right).$$

(5.16)

5.6 Results: Prescribed Load Tests

Tests are conducted for Scotch Packing Tape adhered to a rigid glass substrate subjected only to prescribed vertical load using the experimental setup shown in Figure 5.1. The initial peel arm length, L_0, or the length of tape from the tip position, a, to the grip is set to 25.4 mm (1”). The tip position, a, is imaged as a function of time for an initial peel angle of $\theta = 90°$ and shown below in Figure 5.8.

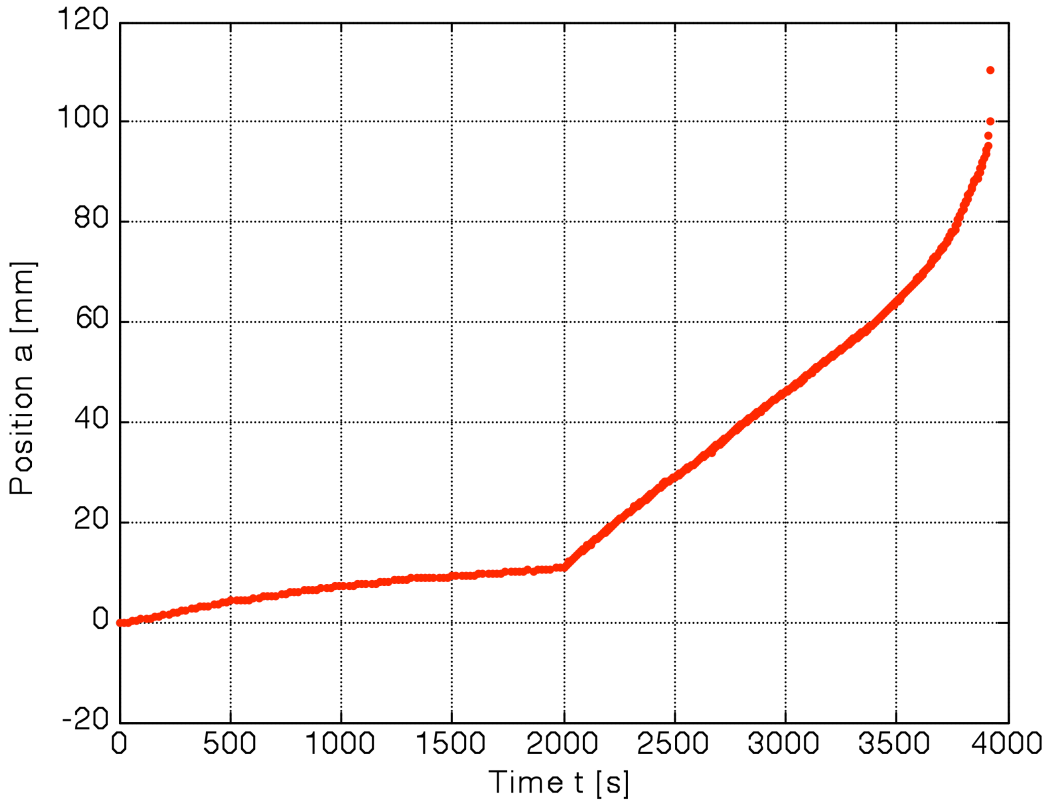

Figure 5.8: Tip position, a, as a function of time, t, for a force-controlled peel test with a guided extremity.

An initial load of P_0 = 60 g is applied at time t = 0. Note from Figure 5.3 that the width of the tape is constant at b =48 mm until a tip position of a = 50 mm, at which point the width decreases linearly as a function of the tape length. The instantaneous slope of the position as a function of time represents the instantaneous tip velocity, da/dt. From time t = 0 to t = 2000 s, the plot shows that the tip velocity is decreasing as the time t increases. This occurs as a result of the decreasing peel angle. Recall from Chapter 4 that the peel angle can be expressed as a function of the tip position, a, and the length of the initial peel arm, L_0, by

$$\theta_i = \cos^{-1}\left(\frac{a}{a + L_0}\right). \tag{4.2}$$

Thus, at time t = 2000 s, the tip position is a = 11 mm and the instantaneous peel angle θ_i = 62°. Since the tip velocity is decreasing, the debonding here is stable, since it is approaching an equilibrium position where it will arrest. At t = 2000s, the weight is increased to reach a total applied load P_1 = 200 g. This results in a faster tip velocity, as can be seen from Figure 5.7. At the tip position where the width begins to decrease (a = 50 mm), the tip velocity, *da/dt*, no longer remains steady and clearly tends towards unstable debonding.

The experimental test shown in Figure 5.8 is now related to the stability regions discussed in Section 5.3. Consider the same plot of the Rivlin relation and the driving force in Figure 5.5 applied to this experiment. In the experiment, the initial peel angle θ_0 = 90° with an applied load of F_{perp} = 60 g. This corresponds to a position on the driving force curve that is above the equilibrium position of the Rivlin curve. As the load is applied from t = 0 s to t = 2000 s, the angle is decreased and eventually the driving force curve approaches the Rivlin curve. As equilibrium is approached, Figure 5.8 shows a correspondence with a decreasing tip velocity. When the driving force and Rivlin curves intersect, this is the point where the tip position will cease to propagate and results in arrest of the debonding. At this point in the experiment, the applied load F_{perp} is now increased to P_1, which translates to a shift vertically up of the driving force curve similar to the scenario presented in Figure 5.6. Now, the tape will continue to peel, this time at a

faster velocity. Before equilibrium is reached again, the variable width is introduced $\left(b' < 0\right)$ and the peeling becomes completely unstable.

Upon examining the previous test to look at how the tip velocity changes as a result of the applied loads P_0 and P_1, it is now interesting to examine what happens for additional experiments when different combinations of P_0 and P_1 are applied. Figure 5.8 shows two separate tests for two different selections of applied loads. For both tests, a load P_0 is applied at t = 0 with an initial peel arm length of L_0 = 12.7 mm (1/2") at an initial peel angle of θ_0 = 90°. At t =3000 s, additional weight is added resulting in a new applied load P_1. In both tests, the tape width is constant at b = 48 mm until a tip position of a = 50 mm is reached, at which point the width begins to decrease linearly as a function of the tape length. Table 5.1 lists the values of the applied loads for each test.

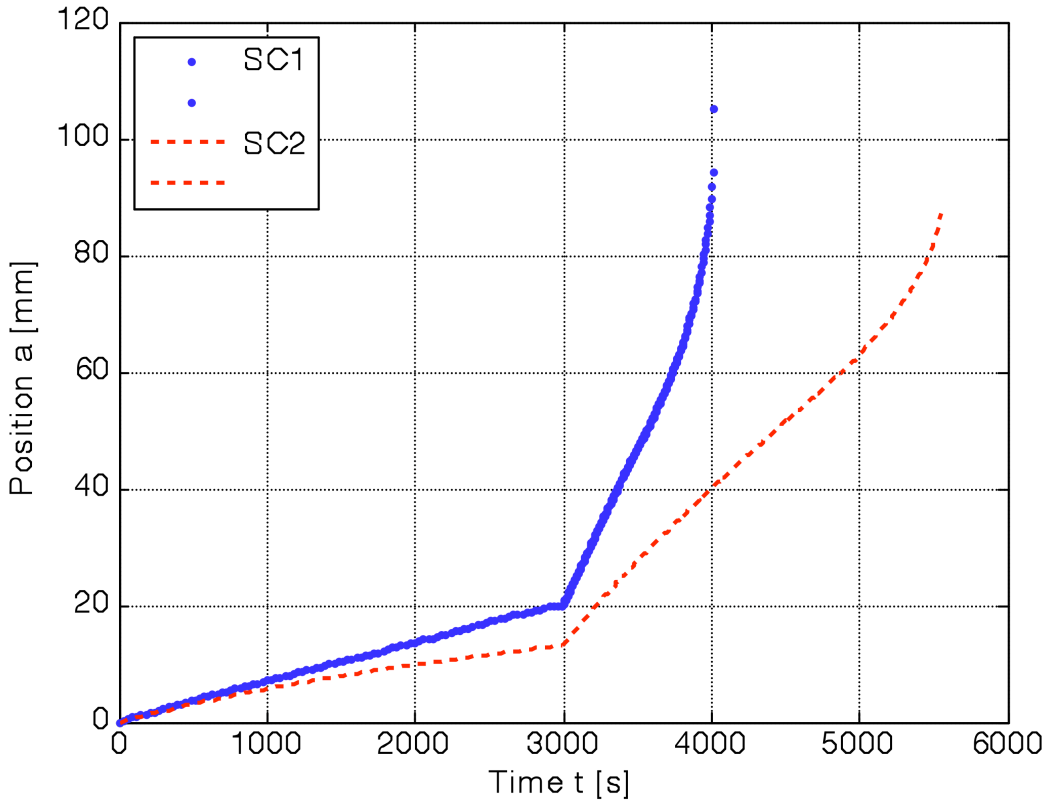

Figure 5.9: Comparison of tip position, *a*, as a function of time, *t*, for two separate force-controlled peel tests with guided tip extremities.

Test #	P_0 (g)	P_1 (g)
SC1	60	200
SC2	50	125

Table 5.1: Applied loads, P_0 and P_1 for the tests shown in Figure 5.9.

This plot shows that there is a relationship between the tip velocity and the applied load P_i. For the initial applied load P_0, the tape is peeled farther for the dotted curve with a larger applied load in the same amount of time. When the load is increased to P_1, the tip velocity increases in both cases, with the curve corresponding to #SC1 test moving faster than the curve corresponding to #SC2 test as a result of the larger load. Similar to the previous test shown in Figure 5.8, peeling tends toward the unstable condition when the

variable width section is reached. Thus, as described in the theoretical criteria presented in Section 5.7, the change in width is a driving condition in affecting the stability of the system.

5.7 Results: Variable Stiffness Tests

The experimental method described in Section 5.4 for introducing a variable stiffness K through an additional applied force F_{par} is carried out with strings of varying width w. These tests differ from the tests of Section 5.6 with an infinite stiffness string in that the initial peel angle θ_0 is set to be approximately 40° as opposed to 90°. In the initial configuration with an applied vertical load F_{perp} and F_{par0} from the string, the tape is at the equilibrium position where the driving force and Rivlin equilibrium curves intersect. As the tension in the string is released, in turn decreasing F_{par}, the peel angle θ will increase, resulting in movement away from the equilibrium position along the driving force curve. The tape will then peel from the substrate as a result of the loading combination F_{perp} and F_{par}.

The first set of experiments investigates the effects of varying combinations of F_{perp} and F_{par0} along with varying string stiffness for Scotch PackingTape of constant width b = 48 mm. Table 5.2 gives a summary of the combination of F_{perp}, F_{par0}, and string widths w (stiffness K is proportional to the width) considered.

Test #	String width, w (mm)	F_{perp} (g)	F_{par0} (g)	F_0 (g)
SK1	6.35	300	400	500
SK2	12.7	300	400	500
SK3	6.35	400	300	500
SK4	12.7	400	300	500

Table 5.2: Summary of test parameters for constant tape width (b = 48 mm) for variable specified stiffness.

Note that for all combinations of F_{perp} and F_{par0}, the initial resultant force F_0 remains the same (F_0 = 500 g). The length of initial peel arm, L_0, and initial string length, L_S, in all of these tests is set to 50.8 mm (2") and 393 mm (15.5"), respectively. A plot of the tip positions, a, of the tape as a function of time, as imaged during the tests, are shown in Figure 5.10. The corresponding outputs from the load cell for the force F_{par} as a function of time are shown in Figure 5.11.

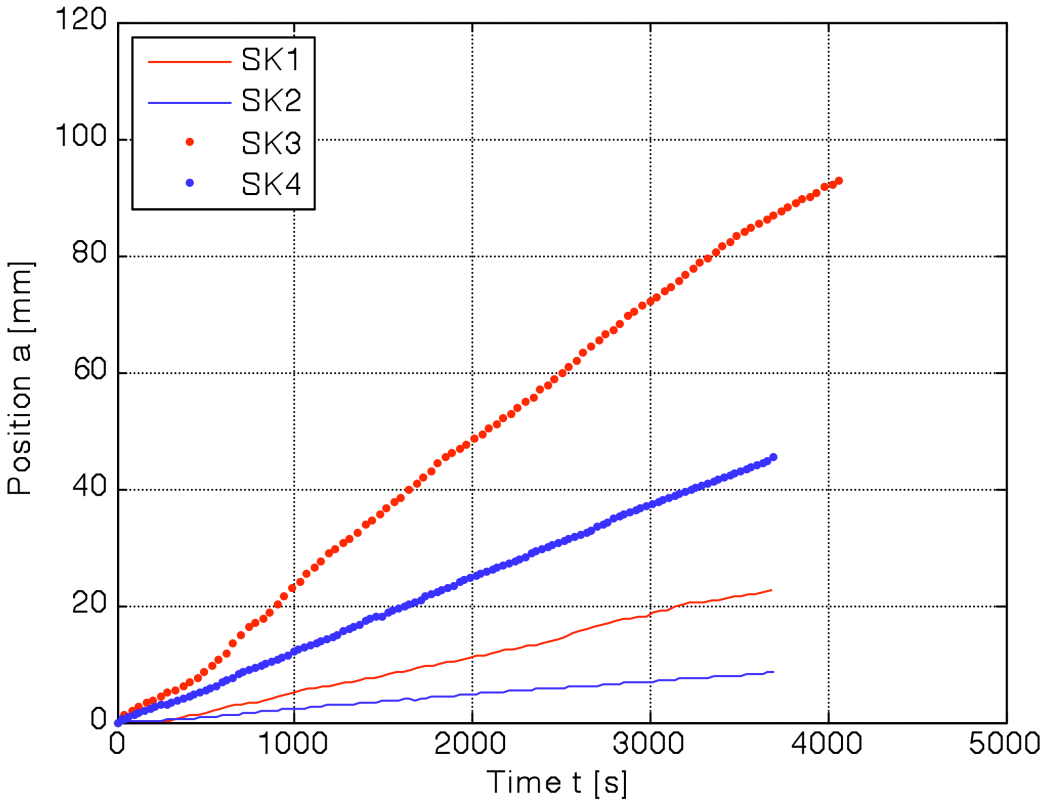

Figure 5.10: Tip position, a as a function of time, t, for tests of variable string stiffness and combinations of F_{perp} and F_{par0} for the same initial resultant force F_0.

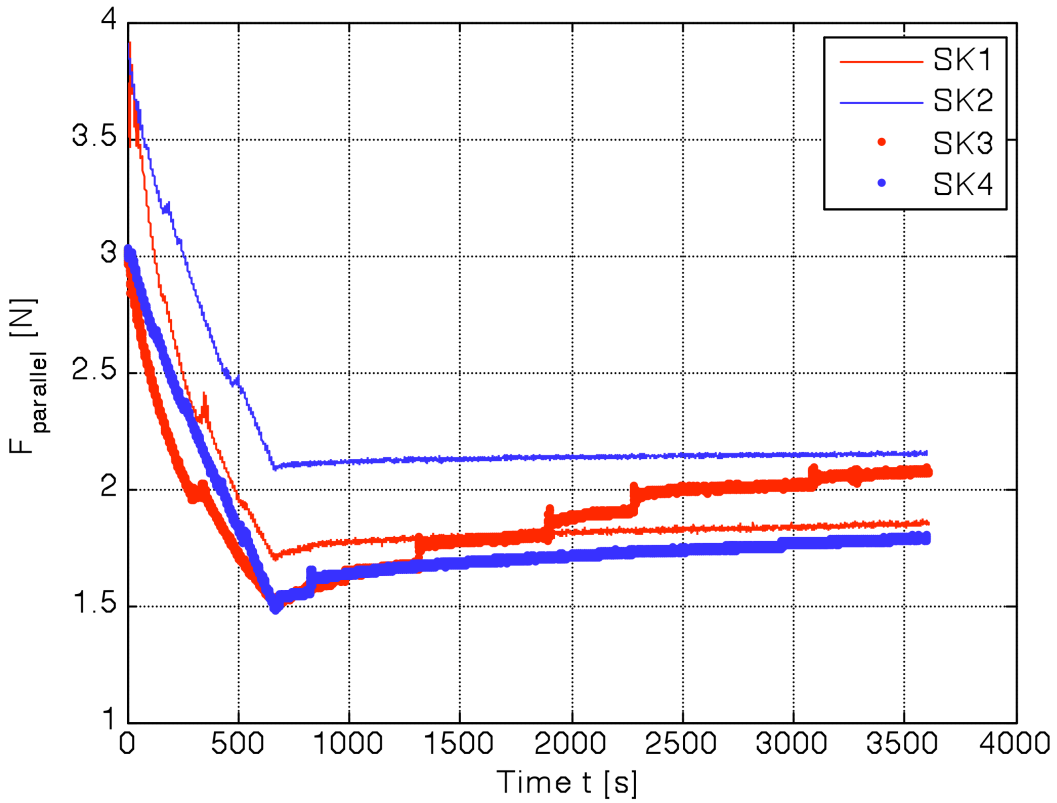

Figure 5.11: Measured force parallel to the substrate, F_{par}, as a function of time, t, for tests of variable string stiffness and various combinations of F_{perp} and F_{par0}. The corresponding tip position as a function of time is shown in Figure 5.10.

Examining Figure 5.10, while the initial resultant force, F_0 in all cases is the same, there is a clear effect of the string stiffness, K, as well as the combination of forces F_{par0} and F_{perp}. Recall from Eq. 5.5 that the stiffness of the string increases as the width of the string increases. This corresponds to the trend we see in the plot in Figure 5.10. Examining two curves with the same F_{perp}/F_{par0} combination but with different widths (SK1 and SK2, SK3 and SK4), the tip velocity da/dt decreases as the width increases. Thus, a system with increased stiffness K results in a slower peeling rate. It is seen further why this result exists from Figure 5.10, since for the same F_{par0}, the decrease in F_{par} is

less for a stiffer string over the same time increment (recall that for all tests here, the string is relaxed at a constant rate of 150 μm/s).

In all cases, the stage is stopped at time t = 600 s. Since the tape is still debonding from the substrate as is seen by the increasing position for the entire time in Figure 5.10, the parallel force F_{par} then increases. This is a result of the tip position, a, moving away from the string while the string is fixed at the load cell.

The increase in F_{par} after time t = 600 s does not seem to affect the propagation of the tip position since the tape used here is of constant width. However, this increase in F_{par} does have an effect on the tip position for the variable width tape, and hence the stability of the debonding process. The infinite stiffness (prescribed load) tests of Section 5.7 already show that the tip velocity increases as the applied load F_{perp} increases. This is seen in Figure 5.10 as well, by comparing tests for the same string width (e.g. SK1 and SK3, SK2 and SK4). This is further evidence that altering the force components F_{par0} and F_{perp} has an effect on the tip velocity.

To examine the exclusive effect F_{par} has on the tip velocity and the stability of the debonding process, tests are conducted for variable width tape while the stage is stopped at different amounts of time to alter the change in F_{par}. In all of these tests, the applied load F_{perp} and initial parallel force F_{par0} are kept the same at 300 g and 350 g, respectively. A string with the same width of w = 12.7 mm (1/2”) is used for all tests described here. The parameters are summarized in Table 5.3.

Test #	Stage stop time (s)	F_{par0} (g)	F_{perp} (g)	String width, w (mm)
SV1	300	350	300	12.7
SV2	400	350	300	12.7
SV3	500	350	300	12.7
SV4	600	350	300	12.7

Table 5.3: Summary of test parameters for the stage stop tests with variable width tape.

The tip position, a, is plotted as a function of time for the four tests with variable width tape in Figure 5.12. In all cases, the initial peel angle is $\theta_o = 40°$ and the initial tip position is set at a point in a region of the constant-width portion of the tape, 5 mm prior to reaching the variable-width portion.

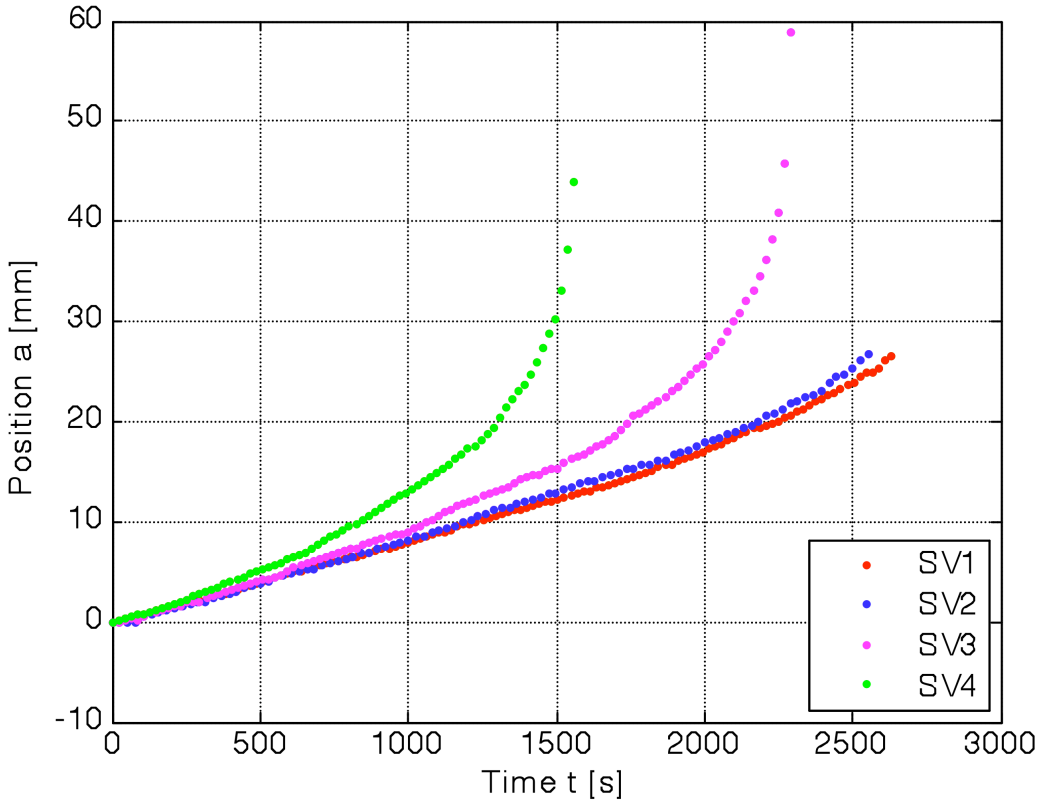

Figure 5.12: Tip position, a, as a function of time, t, for varying stage stop times for separate tests with tape of variable width.

For all of the tests except the one for a stop time of 600 s (SV4), the tip position when the stage is stopped is just prior to the position where the tape changes width. Figure 5.12 shows that the stability of the debonding process is affected by the time at which the stage is stopped. The parallel force F_{par} is larger for the smaller stop times than the larger stop times. As the stop time is increased, the value of F_{par} at the corresponding stop time is lower, resulting in an increase of the tip velocity da/dt promoting unstable peeling. While the tape debonds completely for stop times of 500 s (SV3) and 600 s (SV4), the tape is still attached to the substrate at the end of the test for the stop times of 300 s (SV1) and 400 s (SV2). Although the process also becomes unstable for the smaller stop times, the tip velocity increases at a slower rate. This is consistent with the theoretical stability criterion of Section 5.6 that the debonding process is always unstable for a decreasing tape width.

5.8 Conclusions

This chapter examined the stability of the peel test through a series of experimental investigations aimed at understanding criteria that govern the debonding process of an inextensible adhesive tape to a rigid glass substrate. Experiments show that the tip position and hence the tip velocity change as a function of time as a result of a change in the peel angle as well as the width of the tape. The significance of this result is that the tip velocity is directly related to the adhesion energy of the debonding process, which provides a simple yet rigorous method to characterize stability through means of a simple experimental measurement. Additionally, the experiments conducted here show that there is a relation between the stiffness of the system and the stability. While the stiffness in

these investigations was altered using an elastic string to change a parallel force component in these tests, this can provide significant insight into the gecko adhesion problem in terms of how the gecko alters the force magnitude and directions of the setae during attachment and detachment.

Chapter 6

Summary and Future Work

6.1 Cohesive Zone Law Extraction

This thesis has examined the mechanics of the peel test through experiments, finite element simulations, and theoretical analysis with the aim of developing governing relations to describe the role of adhesion in the peel test for elastic adhesive tapes and in the fracture process in general. An experimental peel test configuration has been developed and validated for the study of the peeling of elastic adhesive tapes. A cohesive zone law is extracted using the experimentally-measured profile of the tape backing in the framework of finite deformation beam theory for a range of peel angles. This cohesive zone law provides information about the mechanical behavior of the adhesive in the process zone, including the full-field force distribution and the adhesion energy. The adhesion energy computed from the cohesive zone law shows good correlation with the value obtained using the Rivlin model, which utilizes a global energy balance of the system. Recall that a cohesive zone law is traditionally postulated and used in a finite element simulation to compare to a known theoretical or experimental result or data set. The new method of using the cohesive zone law to extract the adhesion energy is unique in that it provides a rigorous method of determining the cohesive zone law based upon the measured shape of the tape backing during an experiment.

The validity of the method of cohesive zone law extraction presented in this thesis can be improved in several ways. The formulation in this work is conducted using a single material system: Scotch Magic Tape adhered to a rigid glass substrate. It remains to be seen if this method also yields accurate results for another material, such as a softer adhesive tape such as Scotch+ 33 Electric Tape. In the present study, the substrate (glass) is also treated as rigid and as such is not modeled. With regard to the investigations by Gao and coworkers [7, 8] on the hierarchical structure of the gecko's foot, experimenting with different substrates with surface roughness as well as both random and patterned defects would introduce a dependency of the system on the substrate as well.

The inverse method used for extracting information from the experiments and using it as input for the theory could be tested independent of the Rivlin model by doing the process in reverse. To further validate the cohesive zone law derived in Chapter 3, this law could be input in a finite element simulation of the peel test to compare the predicted shape and force profile to the experimental data. Additionally, the boundary condition used to solve for the axial force T in the non-linear beam theory could be changed and improved. Recall that the far-field peel force P_f measured experimentally is imposed at the position $y_1 = L$ (end of the cohesive zone) as a boundary condition. However, the finite element simulations show that the axial force $P(s)$ at the edge of the process zone is not exactly equal to the far-field peel force measured experimentally. A potential way to impose a more accurate boundary condition would be to prescribe the peel force at infinity of the beam

The overall result could be improved by implementing a physically-based functional form of the curve-fit for the experimental profile in the process zone. The elliptical profile used here yields accurate results, but is not motivated by any physical phenomenon. By including the bending energy similar to the theory used in Chapter 3, Kendall [20] has derived the shape of a peeled band. This shape could potentially be a more accurate fit and thus yield a similar if not better result for the cohesive zone law. As mentioned previously, there are any number of functions that can be used to fit the experimental profile. The second-order polynomial fit first attempted was of similar accuracy to the elliptical profile. However, since the profile is differentiated four times throughout the implementation into non-linear beam theory, the end result was not accurate. This also alludes to an unavoidable source of error in that the experimental data is extracted and used in analytical expressions. Any experimental error will simply be propagated through and amplified in the end result, which in this case is the cohesive zone law and thus the adhesion energy.

Finally, while the cohesive zone law provides a full-field force distribution in the process zone, future work could be aimed at experimentally measuring the full-field displacements in this region. The finite element simulations show that the forces in the process zone are not uniform. Thus, the displacements in this region will also vary throughout the process zone. A candidate method to measure the displacements is the digital image correlation (DIC) technique. DIC is a non-contact, full-field optical strain measurement technique that can be implemented to measure the displacements directly during a peel test. In addition to measuring the deformations in the tape backing, the deformation of the fibrils themselves could be measured. This will allow for accurate

determination of both the opening and sliding displacements *in-situ*. An experimental challenge in using this technique would be applying a stochastic speckle pattern on the adhesive fibrils and/or the tape backing during a test without affecting the adhesive properties of the material.

The use of DIC would also allow for the potential viscoelastic characterization of the tape. This would enable an improved material model over a linear elastic adhesive. Furthermore, the extensibility of the tape could be measured and included in a model. This would enable further investigation of peel angles below 30˚, for which extensibility plays a significant role.

6.2 Rate-Dependence and Stability of Peel

Chapter 4 investigated the rate-dependent effects of the peel test. Using the same experimental peel setup as in Chapter 2 with Scotch Packing Tape as the material, a rate-dependent power-law for the adhesion energy as a function of peel rate is derived. The effect of varying geometrical parameters in the peel test such as the length of the peel arm L_0 and its effect on the tip position and velocity were also examined. While the rate-dependency of the adhesion energy for a single peel angle of $\theta = 90^\circ$ is seen, future work could examine the effect of rate for a larger range of angles. The results of Chapter 4 show that the adhesion energy is constant with respect to the peel angle, but not the velocity. To further improve the proposed rate-dependent power law, its application to a range of peel angles is recommended. The idea of rate-dependency in peel can be extended to the shape of the cohesive zone law. Since the adhesion energy is rate-

dependent, this suggests that the shape of the cohesive zone will also change as a function of rate.

Finally, a study of the stability including the role of compliance during a peel test through several force-controlled experimental configurations was discussed in Chapter 5. Experiments show that the tip position and hence the tip velocity changes as a function of time as a result of a change in the peel angle as well as the width of the tape. The significance of this result is that the tip velocity is directly related to the adhesion energy of the debonding process, which provides a simple and yet rigorous method to characterize stability through means of a simple experimental measurement. Future work aimed at further correlating the experimental results to the theoretical stability criteria will result in significant insight into how the stiffness can be tuned to trigger or delay the onset of stability. Additionally, the experiments show that there is a relation between the stiffness of the system and the stability. While the stiffness in these investigations was altered using an elastic string to change a parallel force component in these tests, this can provide significant insight into the gecko adhesion problem in terms of how the gecko alters the force magnitude and directions of the setae during attachment and detachment. Applying the stability and stiffness criteria directly to previous studies of the gecko may provide additional information as to the micromechanics of the gecko foot during its motion.

References

[1] K. Bundy, U. Schlegel, B. Rahn, V. Geret and S. Perren, "An improved peel test method for measurement of adhesion to biomaterials," *J. Mat. Sci: Materials in Medicine*, **11**, 517-521 (2000).

[2] J.H. Harris and E. Rubel, "The role of interfacial compound formation on package reliability," *Advancing Microelectronics*, **35 (4)**, 20-27 (2008).

[3] M. Balicki, A. Uneri, I. Iordachita, J. Handa, P. Gehlbach and R. Taylor, "Micro-force sensing in robot assisted membrane peeling for vitreoretinal surgery," *Lecture Notes in Computer Science*, **6363**, 303-310 (2010).

[4] K. Autumn, M. Sitti, A. Peattie, W. Hansen, S. Sponberg, Y.A. Liang, T. Kenny, R. Fearing, J. Israelachvili and R.J. Full, "Evidence for van der Waals adhesion in gecko setae," *PNAS*, **99**, 12252-12256 (2002).

[5] K. Autumn, A. Dittmore, D. Santos, M. Spenko and M. Cutkosky, "Frictional adhesion: a new angle on gecko attachment," *J. Exp. Biology*, **209**, 3569-3579 (2006).

[6] Y. Tian, N. Pesika, H. Zeng, K. Rosenberg, B. Zhao, P. McGuiggan, K. Autumn, J. Israelachivili, "Adhesion and friction in gecko toe attachment and detachment," *PNAS*, **103 (51)**, 19320-19325 (2006).

[7] H. Yao and H. Gao, "Mechanics of robust and releasable adhesion in biology: bottom-up designed hierarchical structures of gecko", *J. Mech. Phys. of Solids*, **54**, 1120-1146 (2006).

[8] B. Chen, P. Wu and H. Gao, "Pre-tension generates strongly reversible adhesion of a spatula pad on substrate," *J. R. Soc. Interface*, **6 (35)**, 529-537 (2009).

[9] J.W. Hutchinson and Z. Suo, "Mixed Mode Cracking in Layered Materials," *Advances in Applied Mechanics, edited by J.W. Hutchinson and T.Y. Wu,* **29**, 63-191 (1992).

[10] K. Kendall, "The adhesion and surface energy of elastic solids," *J. Phys. D: Appl. Phys.,* **4**, 1186-1195 (1971).

[11] A.N. Gent and G.R. Hamed, "Peel Mechanics," *J. Adhesion*, **7**, 91-95 (1975).

[12] D.H. Kaelble, "Theory and analysis of peel adhesion: mechanisms and mechanics," *Trans. Soc. Rheology*, **3**, 161-180 (1959).

[13] D.H. Kaelble, “Theory and analysis of peel adhesion: bond stresses and distributions,” *Trans. Soc. Rheology*, **4**, 45-73 (1960).

[14] D.H. Kaelble, “Peel adhesion: Micro-fracture mechanics of interfacial unbonding of polymers,” *Trans. Soc. Rheology*, **9 (2)**, 125-163 (1965).

[15] K.M. Liechti and W.G. Knauss, “Crack-propagation at material interfaces-2: experiments on mode interaction,” *Exp. Mech.*, **22 (10)**, 383-391 (1982).

[16] M. Parvin and W.G. Knauss, “Damage induced constitutive response of a thermoplastic related to composites and adhesive bonding,” *Int. J. Fracture*, **42 (1)**, 57-72 (1990).

[17] F. Niesiolowski and D.W. Aubrey, “Stress distribution during peeling of adhesive tapes,” *J. Adhesion*, **13**, 87-98 (1981).

[18] R.S. Rivlin, “The effective work of adhesion,” *Paint Tech.*, **9**, 215 (1944).

[19] K.L. Johnson, K. Kendall, and A.D. Roberts, “Surface energy and the contact of elastic solids,” *Proc. R. Soc. Lond. A.,* **324**, 301-313 (1971).

[20] K. Kendall, “The shapes of peeling solid films,” *J. Adhesion*, **5**, 105-117 (1973).

[21] K. Kendall, “Interfacial dislocations spontaneously created by peeling”, *J. Phys. K: Appl. Phys.,* **11**, 1519-1527 (1978).

[22] K. Kendall, “Thin-film peeling – the elastic term,” *J. Phys. D: Appl. Phys.,* **8**, 1449-1452 (1975).

[23] G.P. Anderson, K.L. DeVries, and M.L. Williams, “The peel test in experimental adhesive-fracture mechanics,” *Exp. Mech.*, **16 (11)**, 11-15 (1976).

[24] Z.C. Leseman, S.P. Carlson and T.J. Mackin, “Experimental measurements of the strain energy release rate for stiction-failed microcantilevers using a single-cantilever beam peel test,” *J. MEMS*, **16 (1)**, 38-43 (2007).

[25] ASTM D903 – 98, “Standard test method for peel or stripping strength of adhesive bonds,” ASTM International, West Conshohocken, PA (2010).

[26] D. Garrivier, E. Decave, Y. Brechet, F. Bruckert and B. Fourcade, “Peeling model for cell detachment,” *Eur. Phys. J. E*, **8**, 79-97 (2002).

[27] M.A. Griffin, A.J. Engler, T.A. Barber, K.E. Healy, H.L. Sweeney and D.E. Discher, “Patterning, prestress, and peeling dynamics of myocytes,” *Biophys. Journal*, **86**, 1209-1222 (2004).

[28] C. Verdier and G. Ravilly, “Peeling of polydimexylsiloxane adhesives: the case of adhesive failure,” *J. Polymer Sci. Part B: Polymer Physics*, **45 (16)**, 2113-2122 (2007)

[29] K-H. Tsai and K.-S. Kim, “Stick-slip in the thin film peel test – I. The 90˚ peel test,” *Int. J. Solids Structures*, **30 (13)**, 1789-1806 (1993).

[30] K-S. Kim and N. Aravas, “Elastoplastic analysis of the peel test,” *Int. J. Solids and Structures*, **24 (4)**, 417-435 (1988).

[31] Y. Wei and J.W. Hutchinson, “Interface strength, work of adhesion and plasticity in the peel test,” *Int. J. of Fracture*, **93**, 315-333 (1998).

[32] M.D. Thouless and Q.D. Yang, “A parametric study of the peel test,” *Int. J. Adhesion and Adhesives*, **28 (4-5)**, 176-184 (2008).

[33] K-S. Kim and J. Kim, “Elasto-plastic analysis of the peel test for thin film adhesion,” *Trans. of the ASME*, **110**, 266-273 (1988).

[34] J.A. Williams and J.J. Kauzlarich, “The influence of peel angle on the mechanics of peeling flexible adherends with arbitrary load-extension characteristics,” *Tribology Int.,* **38**, 951-958 (2005).

[35] J.A. Williams and J.J. Kauzlarich, “Peeling shear and cleavage failure due to tape prestrain,” *J. Adhesion*, **80**, 433-458 (2004).

[36] A. Molinari and G. Ravichandran, “Peeling of elastic tapes: effects of large deformations, pre-straining, and peel-zone model,” *J. Adhesion*, **84 (12)**, 961-995 (2008).

[37] N.S. Pesika, Y. Tian, B. Zhao, K. Rosenberg, H. Zeng, P. McGuiggan, K. Autumn and J.N. Israelachivili, “Peel-zone model of tape peeling based on the gecko adhesive system,” *J. Adhesion,* **83**, 383-401 (2007).

[38] Y. Wei and H. Zhao, “Peeling experiments of ductile thin films along ceramic substrates – critical assessment of analytical models,” *Int. J. Solids and Structures*, **45**,3779-3792 (2008).

[39] D.S. Dugdale, “Yielding of steel sheets containing slits,” *J. Mech. and Phys. of Solids*, **8**, 100–104 (1960).

[40] G.I. Barenblatt, “The mathematical theory of equilibrium cracks in brittle materials,” *Advances in Applied Mech.,* **7**, 55-129 (1962).

[41] L. Prandtl, “Ein Gedankenmodell fuer den Zerriessvorgang sproeder Koerper,” *Zeitschrift fuer angewandte Mathematik und Mechanik*, **13**, 197-204 (1933).

[42] J.W. Hutchinson, "A course on non-linear fracture mechanics," Lecture notes, Technical University of Denmark (1979).

[43] T. Ungsuwarungsri and W.G. Knauss, "A nonlinear-analysis of an equilibrium craze 1: problem formulation and solution," *J. App. Mech.*, **55 (1)**, 44-51 (1988).

[44] T. Ungsuwarungsri and W.G. Knauss, "A nonlinear-analysis of an equilibrium craze 2: simulations of craze and crack-growth," *J. App. Mech.*, **55 (1)**, 52-58 (1988).

[45] A. Zehnder, "Lecture notes on fracture mechanics," Lecture notes, Cornell University, Ithaca, NY (2008).

[46] J.W. Hutchinson and V. Tvergaard, "The influence of plasticity on mixed-mode interface toughness," *J. Mech. Phys. Solids*, **41**, 1119-1135 (1993).

[47] Abaqus/Standard Finite Element Analysis Software, *Simulia*, Providence, RI.

[48] G.T. Camacho and M. Ortiz, "Computational modeling of impact damage in brittle materials," *Int. J. Solids and Structures*, **33 (20-22)**, 2899-2938 (1996).

[49] S.P. Timoshenko and J.N. Goodier, "Theory of Elasticity, 2nd Edition" *McGraw Hill* (1951).

[50] M.D. Thouless and H.M. Jensen, "Elastic fracture mechanics of the peel-test geometry," *J. Adhesion*, **38**, 185-197 (1992).

[51] W.G. Knauss, "Viscoelasticity and the time-dependent fracture in polymers," *Comprehensive Structural Integrity, Vol. 2: Fundamental Theories and Mechanisms of Failure,* 383-428 (2003).

[52] M.A. Meitl, Z.T. Zhu, V. Kumar, K.J. Lee, X. Feng, Y.Y. Huang, I. Adesida, R.G. Nuzzo, and J.A. Rogers, "Transfer printing by kinetic control of adhesion to an elastomeric stamp," *Nat. Materials*, **5**, 33-38 (2006).

[53] S. Xia, Rate-dependency of heterogeneous adhesive materials peeled from substrates with patterned defects, Personal communication (2011).

[54] A. Molinari, Stability criteria for a force-controlled peel test of inextensible elastic adhesive tapes, Personal communication (2011).